Hydrodynamics and suspended sediment dynamics in estuarine channel networks: an idealised modelling approach

Jinyang Wang 汪金洋

Coastal and Shelf Sea Dynamics group
Institute of Marine and Atmospheric research Utrecht
Department of Physics
Utrecht University

ISBN: 978-94-6458-700-5
Printing: Ridderprint, www.ridderprint.nl
Cover photos: Antony Spencer, www.antonyspencer.com
Designed by Jiaxin Li

Hydrodynamics and suspended sediment dynamics in estuarine channel networks: an idealised modelling approach

De dynamica van waterbeweging en gesuspendeerd sediment in estuariene kanaalnetwerken: een geïdealiseerde modelleringsbenadering

(met een samenvatting in het Nederlands)

Proefschrift

ter verkrijging van de graad van doctor aan de
Universiteit Utrecht
op gezag van de
rector magnificus, prof.dr. H.R.B.M. Kummeling,
ingevolge het besluit van het college voor promoties
in het openbaar te verdedigen op

woensdag 7 december 2022 des ochtends te 10.15 uur

door

Jinyang Wang

geboren op 27 mei 1993
te Shanghai, China

Promotor:	Prof. dr. H. E. de Swart
Copromotor:	Dr. Y. M. Dijkstra

Assessment Committee:	Prof. dr. H.Q. Cheng
	Prof. dr. ir. A.J.F. Hoitink
	Prof. dr. H.M. Schuttelaars
	Prof. dr. Z.B. Wang
	Prof. dr. L.R.M. Maas

This thesis was accomplished with financial support from the Dutch Research Council (NWO) (Grant ALWSW.2016.012).

Contents

1 Introduction **1**
1.1 Phenomena in estuarine networks 3
1.2 Current state of the art 5
1.3 Knowledge gaps and research questions 6
1.4 Research approach 7
1.5 Thesis outline 7

2 Dependence of tides and river water transport on river discharge, tidal forcing, geometry, and sea level rise **9**
2.1 Introduction 11
2.2 Model and Methods 12
2.3 Results 20
2.4 Discussion 34
2.5 Conclusions 37

3 Mechanisms controlling the distribution of net water transport in estuarine networks **41**
3.1 Introduction 43
3.2 Model and Methods 45
3.3 Results 54
3.4 Discussion 63
3.5 Conclusions 67
3A Sensitivity of baroclinic transport to horizontal diffusivity . . . 69

4 Dependence of turbidity maxima on fluvial sediment input and local deepening/narrowing **71**
4.1 Introduction 73
4.2 Model 74
4.3 Methods and design of experiments 76

4.4 Results 81
4.5 Discussion 90
4.6 Conclusions 93

5 Synthesis **95**
5.1 Conclusions 95
5.2 Outlook 98

Supplementary informationg **103**
S1 Time structure of the model solutions 103
S2 Scaling and perturbation expansion 105
S3 Turbulence model 107
S4 Solutions to water motion 112
S5 Derivation of the continuity of dynamic pressure 117
S6 Solution procedure 119
S7 A network perspective decomposition of net sediment transport 120
S8 Figures 122

Bibliography **135**

Summary **147**

Nederlandse samenvatting **151**

Acknowledgements **155**

Curriculum vitæ **157**

1

Introduction

An estuary is a semi-enclosed coastal body of water that has a free connection to the open sea, of which the saline water is diluted by the fresh water from the river (Cameron and Pritchard, 1963, Valle-Levinson, 2010). In lowland areas all around the globe, the planform topology of estuaries often features multiple interconnected channels: an estuarine channel network (Hoitink and Jay, 2016). Examples are the Yangtze Estuary in East Asia, the estuary of the Ganges-Brahmaputra Delta in South Asia, the Rhine-Meuse-Scheldt Estuary in Western Europe, and the Amazon Estuary in South America (Fig. 1.1). As tides propagate into the estuarine channels from the sea, the water level and current in the estuarine channel network vary continuously on tidal timescales. Along with the tidal flow, salt and marine sediments are periodically transported into and out of these channels. Simultaneously, the river flow imports freshwater and fluvial sediments into the estuary. On the bottom of the channels, the stress exerted by the water motion erodes sediments into suspension. The focus of this thesis is on the hydrodynamics and suspended sediment dynamics in estuarine channel networks.

The hydrodynamics and sediment dynamics greatly impact the ecological and economic functions fulfilled by the estuarine channels. Typically being rich in nutrients, they provide invaluable resources for a diverse range of coastal inhabitants (e.g., planktons, mangroves, and birds) through the food web (Kennish, 1990). Although the spatial content of estuaries covers less than 1% of the marine area, the exceptional productivity of estuarine organisms provides almost 6% of global fishery yields (Cowan Jr. et al., 2012). Besides their ecological implications, they are important for agriculture and provide access to major ports all over the world (e.g., Antwerp and Shanghai). Agricultural

Figure 1.1: Some examples of estuaries with multiple interconnected channels. Satellite images from Google Earth.

activities can be hampered by flooding with brackish water (Cox et al., 2006) and maritime transport can be restricted if the water depth is less than the required navigational depth (Eloot and Vantorre, 2011).

The level of achievement of estuarine functions is affected by the changing environment, which includes the inherent variability (e.g., seasonality) and sea level rise due to the changing climate (IPCC, 2019, 2022). Specifically, risks have been imposed by estuarine environmental disturbances due to human interventions. Sanitary sewer overflow resulting from residential, industrial, and commercial activities contributes to estuarine contamination by pathogens and nutrients (García-García et al., 2021). The pathogens affect the flora and fauna, including people who may consume them. The excessive amounts of nutrients may trigger eutrophication that causes toxic algal blooms (Anderson et al., 2002). The construction of human facilities (e.g., ports and navigational channels) immediately causes the destruction of natural estuarine habitats. It also establishes the potential of recurrent investment in sediment dredging, which may periodically increase the turbidity that may cause hypoxia (Zaikowski et al., 2008, Talke et al., 2009). Climate change, the planning of human facilities, and maintenance require appropriate evaluations for the responses of the networks to these changes. This is only possible if there is a thorough understanding of various physical phenomena in estuarine channel networks.

Viewing an estuarine channel network as an integrated system, hydrodynamics and sediment dynamics are essential components. They are vital in understanding the responses to changes. Therefore, this thesis aims to gain a more fundamental understanding of the dependence of the hydrodynamic

and turbidity phenomena on different types of changes in estuarine channel networks. In Section 1.1, observable phenomena in estuarine channel networks that play key roles in this thesis are described, followed by an overview of existing theories and models for these phenomena (Section 1.2). Section 1.3 contains the knowledge gaps and specific research questions. The research approach is presented in Section 1.4. The thesis is further outlined in Section 1.5.

1.1 Phenomena in estuarine networks

1.1.1 Tides and river flow

Two prominent forcings for the flow in an estuarine channel network are river and tides. The river flow is the consequence of the freshwater discharge from terrestrial runoff. Under the influence of tides from the open sea, the periodic rise and fall of the water level can be also observed at different locations in an estuarine channel network. In general, at any moment in time, such water levels are spatially non-uniform, causing the transport of water, because the water flows from a higher level to a lower level. Hence, the current of the flow is also periodic. Although the most dominant tidal signal is typically semi-diurnal, the time series of the water level and current velocity are hardly perfectly sinusoidal, as the consequence of the various tidal constituents (Gerkema, 2019). This further gives rise to the fortnightly tidal signal, the spring-neap variation. In addition, a single tidal constituent may generate overtides, integer multiples of the frequency, due to nonlinearities such as advection and bottom stress.

The coexistence of the tidal flow and river flow implies that they mutually influence each other, not only inside of every channel, but also at the junctions (or branching points), where the flows in different channels are connected and synchronised. Tides experience enhanced friction due to river flow, which varies over the year. It has been observed that the tidal characteristics (water level and current) depend on the river discharge in an estuarine channel network (Guo et al., 2015), known as the river-tide interaction (Godin, 1999). Besides, the division of river flow at a junction depends on tides (Buschman et al., 2010).

Both the tidal flow and river flow exhibit a vertically sheared structure. This is caused by the bottom friction experienced by the flow generates turbulence, which penetrates up to the surface through eddies (Nezu and Nakagawa, 1993, Nieuwstadt et al., 2016).

1.1.2 Estuarine circulation

A key pattern of the flow in estuarine channels is the estuarine circulation (see Geyer and MacCready, 2014, for a review), the circulation pattern in an along-channel cross-section when the longitudinal flow velocity is tidally averaged. It is formed due to mass conservation of the estuary: the net (i.e.,

subtidal/residual/tidally averaged) inflow is balanced by the net outflow, while their dependences on depth are not identical. A classical example of estuarine circulation is the density-driven flow (Hansen and Rattray, 1965). It is forced by the horizontal density gradient, even when the density is vertically well-mixed. This density gradient is the consequence of the spatial varying subtidal salinity, as the estuary connects freshwater to saline seawater.

The action of the vertically sheared tidal flow on a horizontal density gradient further leads to the phenomenon known as tidal straining (Simpson et al., 1990). It effectively intensifies the circulation pattern due to the density-driven flow, which has been verified by field observations (Stacey and Ralston, 2005).

1.1.3 Net transport of water and matter

In estuaries, the transport of both water and substances occurs. In a channel with only river flow, the transport of water is unidirectionally seaward. In a channel with only tidal flow, a net landward mass transport can be observed, known as the Stokes transport (Stokes, 1847), which is fully compensated by the seaward return flow, if the tide is not a standing wave (see van den Bremer and Breivik, 2018, for a review). Similarly, the circulation pattern exhibited by the density-driven flow also features the balance between inflow and outflow. Thus, in a single channel estuary with river flow, tides, and density gradients, the net transport of water equals the river discharge. In a network, however, the net transport of water in a channel may depend on tides, salinity distribution, et cetera. For example, the landward Stokes transport in one channel does not need to be compensated by the return flow anymore; this amount of water mass can be transported back to the sea through another channel.

The flow also transports suspended sediments. In the along-channel direction, the river flow constantly transports freshwater and fluvial fine sediments into the estuary. Under the influence of tides, sediments are transported into the estuary during the flood and flushed out of the estuary during the ebb. In the vertical direction, sediments tend to settle and deposit onto the bed, while they are also forced upward by turbulence created by the friction that the current experiences at the bed. The combination of these processes creates a complex along-channel distribution of sediment.

1.1.4 Estuarine turbidity maximum (ETM)

In estuarine environments, it can be often observed that the sediment concentration attains a local maximum: the estuarine turbidity maximum (ETM). As turbidity is the visual perception of the sediment concentration and because of the stochastic nature of the fluid motion, an ETM appears to be a broad zone where the water seems to be more turbid than the neighbouring area. ETMs can be observed at different locations, such as near the salt intrusion limit and in the freshwater zone. Their formation is usually the result of the horizontal

convergence in the sediment transport (see Burchard et al., 2018, for a review). In an estuarine channel network, ETMs can be observed in multiple channels. Examples are the Mahakam Estuary (Salahuddin and Lambiase, 2013) and the Yangtze Estuary (Wan and Zhao, 2017). It has been shown that the locations of these ETMs vary over time and may travel from one channel to another.

1.2 Current state of the art

This section provides a brief overview of existing knowledge and literature about the hydrodynamics and sediment dynamics in estuarine channel networks. Apart from field measurements (e.g., Buschman et al., 2010, Sassi et al., 2011, Bain et al., 2019), there are two types of frameworks for studying water motion and sediment dynamics. The first resolves the complex geometry of the system (e.g., Achete et al., 2016, Shan et al., 2019), which is useful to study the local dynamics near the junctions and make accurate predictions. The second considers a single channel as the basic element, from which the channel network is constructed based on conservation laws (e.g., Hill and Souza, 2006, Alebregtse and de Swart, 2016), hereinafter referred to as the network framework. It allows for explicit interpretations of the interactions among the channels, which will be the focus of the reviewed literature below.

The study of tidal propagation in interconnected channels goes at least a century back (Lorentz, 1926), in which quadratic bottom stress is represented by linear stress, assuming the same energy dissipation over one tidal cycle. Later, it has been studied by, for example, Defant (1961), Hill and Souza (2006), who showed that the conservation of mass together with the continuity of water level is a reasonable description for the water motion over a junction. These studies concerned the linear tide of a single constituent, meaning that there is neither residual flow nor overtides. Moreover, the continuity of water level has been demonstrated to be the lower order approximation for momentum conservation when the surface area at the junction is small (van de Kreeke, 1988, Nassehi and Bikangaga, 1993). Zhang et al. (2012) applied the nonlinear theory for tidal propagation of Savenije et al. (2008) to the estuarine channel network of the Yangtze. However, the final solution for tidal propagating in every channel was obtained by fitting to the observational data.

The net transport of water in the channels is affected by the river flow. The division of river flow at a junction has been studied by many researchers (e.g., Wang et al., 1995, Bolla Pittaluga et al., 2003, Kleinhans et al., 2013). However, tides were not considered in these studies. Based on the study of Buschman et al. (2010), Sassi et al. (2011) explained the effect of tides on the division of net water transport through the differential water level set-up: the tides cause an additional pressure gradient at the junction, which is compensated by net transport of water so that tides contribute to the net water transport. Alebregtse and de Swart (2016) explicitly modelled the river-tide interaction

through the bottom stress in an estuarine channel network. They found that the distribution of the net water transport over the channels is globally determined by the entire network system, rather than locally determined near the junctions.

Regarding the division of suspended sediment transport at junctions in the estuarine channel network, Buschman et al. (2013) found that it strongly depends on the local geometry around the junction. Sassi et al. (2013) argued that it is the upstream transverse distribution of suspended sediment concentration profile that determines the instantaneous division of the sediment transport. They further extended the finding by Kleinhans et al. (2008) in terms of the high correlation between the division of net water and suspended sediment transports from fluvial to estuarine environments.

Some research has been carried out on the suspended sediment dynamics in estuarine channel networks using the framework that fully resolves the complex geometry (e.g., Achete et al., 2016, Zhu et al., 2021) and the ETM dynamics due to sediment trapping mechanisms have been extensively discussed in a single channel estuary (see Burchard et al., 2018, for a review).

1.3 Knowledge gaps and research questions

Much of our process-level understanding of tides and river flow in estuarine channel networks is in terms of vertically averaged models, their interaction has not been explicitly studied when the flow vertical structure is accounted for. Furthermore, existing studies of river water transport and tidal propagation in estuarine networks with a focus on their dynamics in a network geometry do not consider the flow vertical structure (Hill and Souza, 2006, Alebregtse and de Swart, 2016) and the sensitivities of net transport of water to river discharge, tidal forcing, local geometric changes, and sea level rise have not been investigated.

In addition to the river discharge and tides, the net water transport in each channel of an estuarine network can be affected by other forcing agents, such as baroclinic pressure gradients induced by horizontal salinity gradients (Zhang et al., 2017). These contributions have not been analysed within the network framework; hence, their relative importance remains unknown. This also holds for the sensitivity of each component of the net water transport to river discharge, tidal forcing, local geometric changes, and sea level rise. Moreover, it is not clear if the flow vertical structure may influence the distribution of the net water transport over the channels.

Little is known about the response of the ETM dynamics to changing conditions in a network, such as the upstream damming that reduces the fluvial sediment input and the dredging and the construction of the training walls in a channel.

Motivated by the above knowledge gaps, the following research questions will be addressed for estuarine channel networks.

$\mathcal{Q}1$ How do tidal propagation and the distribution of river water transport depend on the river discharge, external tidal forcing, local geometric changes, and sea level rise, when the flow vertical structure is accounted for?

$\mathcal{Q}2$ What are the contributions of the river, tides, and horizontal density gradients to the distribution of net water transport in estuarine channel networks and their sensitivities to river discharge, tide, human interventions, and sea level rise?

$\mathcal{Q}3$ What is the dependence of ETMs in an estuarine network on fluvial sediment discharge and on changes in depth and width in one channel of the network?

1.4 Research approach

To obtain a more fundamental understanding of the hydrodynamics and suspended sediment dynamics in estuarine networks in the along-channel and vertical directions, process-based idealised width-averaged models will be developed and used. The governing equations are solved (semi-)analytically. This creates a computationally inexpensive model and hence allows extensive sensitivity analyses for each individual estuarine process. Such models are exploratory in nature, their purposes are elaborated in Murray (2003) in comparison with the more sophisticated simulation models.

1.5 Thesis outline

The research questions 1-3 are addressed in Chapters 2-4, respectively. A summary and outlook are contained in Chapter 5.

2

Dependence of tides and river water transport on river discharge, tidal forcing, geometry, and sea level rise

This chapter is based on the article Wang, J., de Swart, H. E., and Dijkstra, Y. M. (2021) Dependence of tides and river water transport in an estuarine network on river discharge, tidal forcing, geometry and sea level rise. *Continental Shelf Research* 225, 104476. https://doi.org/10.1016/j.csr.2021.104476

Abstract

Estuaries are often characterised by a complex network of branching channels, in which the water motion is primarily driven by tides and fresh water discharge. For both scientific reasons and management purposes, it is important to gain more fundamental knowledge about the hydrodynamics in such networks, as well as their implications for turbidity and ecological functioning. A generic 2DV estuarine network model is developed to study tides and river water transport and to understand the dependence of their along-channel and vertical structure on forcings, geometry characteristics and sea level changes. The model is subsequently applied to the Yangtze Estuary to investigate tides and the distribution of river water over channels during dry and wet seasons, spring tide, as well as prior to and after the formation of Hengsha Passage and the construction of the Deep Waterway Project, and sea level rise. Increasing river discharge enhances the friction for tides by increasing both internal and bottom stresses. Changes in tidal forcing are correlated with the friction for both tide and river. A shortcut channel reduces the water level difference in adjacent channels, as well as the tidal amplitudes difference. Sea level rise results in larger friction parameters, faster propagation of tides, and more even distribution of river water transport. The distribution of river water transport is hardly affected by the above-mentioned changes. Model results and current vertical structure are consistent with observations.

2.1 Introduction

Many of the world's estuaries have the structure of a network with multiple connected channels. Examples are the Yangtze Estuary (China), the Mahakam Delta (Indonesia), the Pearl River Delta (China), and the Berau Estuary (Indonesia). Compared to a single-channel estuary, the network structure adds further complexity to the dynamics. Knowledge of the tides and transport of river water of estuarine networks is important to prevent coastal flooding, manage fresh water supply and for ecology (transport of matter, turbidity dynamics, etc.) This is especially important since human interventions (e.g., dredging and constructions) and climate change (e.g., sea level rise) may strongly alter the conditions of the entire system (Winterwerp et al., 2013, Cheng et al., 2018).

Besides focusing on the water levels alone, accounting for the vertical structure of tidal currents is considered to be important, as velocity shear is crucial for e.g., sediment dynamics and ecology (Dijkstra et al., 2018, Cloern et al., 2016). In this study, we focus on the vertical structure of tidal and river flows in networks from the perspective of an idealised model. An idealised model is a useful tool, because it can help to reveal the contribution of individual physical processes. Moreover, such a model is fast and therefore suitable for sensitivity studies.

Tidal propagation in a single channel estuary has been investigated by numerous researchers (Friedrichs, 2010, Geyer and MacCready, 2014, Talke and Jay, 2020, and references therein). The evolution of water level and tidal discharge is well understood in terms of analytical relations and sensitivity to changing parameters (Friedrichs and Aubrey, 1988, 1994, Ridderinkhof et al., 2014, Lanzoni and Seminara, 1998). Also, the vertical structure of tidal current has been studied (Ianniello, 1977, 1979). Numerical models exist to simulate tidal dynamics in networks. E.g., Buschman et al. (2010) used an idealised 2DH numerical model to examine the effect of amplitude of M_2 sea surface elevations on the division of river water transport at the delta apex junction in the Berau region. Sassi et al. (2011) used a numerical 2DH model to show that, in the east part of Mahakam Delta, Indonesia, a so-called differential water level setup occurred. This concerns the modification of river discharge distribution over channels due to subtidal water level difference that arises from the interaction of surface elevations induced by subtidal flow and river. Full 3D numerical models of Zhu et al. (2018) for the Yangtze Estuary successfully simulated tides and net water transport prior to and after a major intervention, the Deep Waterway Project (DWP) that comprised the deepening and narrowing of one channel of this estuarine network. However, the more fundamental understanding of tidal propagation in estuarine networks in terms of analytical solutions and parameters sensitivities is less well-developed. Tides in a channel network were first studied by Lorentz (1926). He developed a 1D (cross-sectional averaged) analytical model to quantify tides and storm surges

in the Dutch Wadden Sea and Zuiderzee prior to and after the construction of a dyke. A generic analytical linear 1D network model for tides was developed by Hill and Souza (2006). They applied it to investigate tides in a fjord system in the east of Queen Charlotte Sound, western Canada, where friction is weak. Alebregtse and de Swart (2016) extended the Hill and Souza (2006) model such that it also describes nonlinear tides and net water transport in friction-dominated estuaries and applied their model to the Yangtze Estuary.

However, idealised models for tidal dynamics in networks resolving the vertical current structure are missing. Hence, the first aim of this study is to develop a vertically resolving idealised model for tides and river discharge in estuarine networks. The second aim is to use this model to gain a more fundamental understanding of tides and the transport of river water in a network and how this responds to changes in river discharge, tidal forcing, geometry, and sea level rise. Specifically, this work adds the interaction between eddy viscosity, bottom friction, and tidal propagation in a network under several local and global modifications.

The 2DV network model will be used to examine the Yangtze Estuary (YE), which is characterised by strong seasonal cycles in both river discharge and tidal forcing (Guo et al., 2015). In addition, multiple changes in geometry occurred in this estuary over the last century due to both anthropogenic activities and natural evolutions. Besides the already mentioned DWP, a shortcut channel, the Hengsha Passage (HP), formed during the severe floods in 1954 and thereby enriched the branching characteristics of the YE (Kuang et al., 2014a). Furthermore, the YE is subject to sea level rise (SLR) (Kuang et al., 2017), which increases the difficulty for decision-makers to implement adequate management strategies (Cheng et al., 2018).

This chapter is organised as follows. Section 2.2 describes the model geometry and outlines the derivation of the final equations that govern the tide-river system. Section 2.3 presents the results from applying the model to the Yangtze Estuary, with a focus on the effects of changes in the forcings and geometry on tidal characteristics (i.e., amplitudes and phases of tidal currents and surface elevations) and the magnitudes of river water transport. Section 2.4 contains the discussion, followed by the conclusion in Section 2.5.

2.2 Model and Methods

2.2.1 Model

Domain

Consider an idealised estuarine network system that consists of multiple connected channels. The water motion is forced by both river discharge at the various river heads and by tidal sea surface variations. Each channel has a

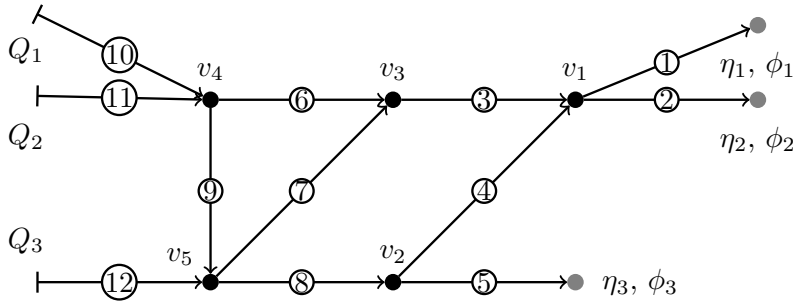

Figure 2.1: A schematic diagram for an arbitrary estuarine network, following Hill and Souza (2006). Channel indices are in white circles. Solid grey circles denote open sea with tidal forcings indicated next to them. Channels connected to the sea are referred to as sea channels. The closed ends (tidal limit or a weir) of so-called river channels are shown as vertical bars; at these locations, a constant river discharge is prescribed and the tidal current vanishes. The set of indices for each branching point is denoted by v_i. Here, $v_1 = \{-1, -2, 3, 4\}$, $v_2 = \{-4, -5, 8\}$, $v_3 = \{-3, 6, 7\}$, $v_4 = \{-6, -9, 10, 11\}$, and $v_5 = \{-7, -8, 9, 12\}$, where the numbers between braces denote the channels that are connected at each branching point. Positive and negative signs indicate whether the positive x-direction of that channel is pointing towards or away from the branching point.

constant depth H_j and a constant length L_j, where j is the channel index. Both the transverse and longitudinal bed slopes are 0 in all channels. Cartesian coordinates x and z are used, where the positive x-direction is seaward and the z-axis points vertically upwards, with $z = 0$ the approximate subtidal water level, which is assumed to be constant for each channel. The width B_j of each channel is assumed to vary exponentially in x and does not depend on z, i.e.,

$$B_j(x) = B(L_j) \exp\left(\frac{x - L_j}{L_{b,j}}\right), \qquad 0 \leq x \leq L_j. \tag{2.2.1}$$

In this expression, $L_{b,j}$ is the length scale at which channel width increases exponentially in the seaward direction. Channel labelling is explained in Fig. 2.1. Channel index will be omitted from hereon for simplicity if the equations hold for all channels, unless specified otherwise.

Equations of motion

The equations governing tides and river water transport are the width-averaged shallow water equations. It is assumed that advection, horizontal dispersion, drying/flooding of tidal flats, and the baroclinic pressure gradient are negligible. Next, the water motion, to the leading order, is assumed to consist only of M_2

and the subtidal component. The resulting equations at each frequency are (see e.g., Ianniello, 1979)

$$\frac{\partial u_n}{\partial t} = -g\frac{\partial \eta_n}{\partial x} + \check{A}_{vn}\frac{\partial^2 u_n}{\partial z^2}, \tag{2.2.2a}$$

$$\frac{\partial u_n}{\partial x} + \frac{\partial w_n}{\partial z} + \frac{1}{L_b}u_n = 0. \tag{2.2.2b}$$

Here, the subscript n denotes the harmonic component ($n = 0$ for subtidal and $n = 1$ for M_2 tide), u and w are the horizontal and vertical width-averaged velocities, respectively. Furthermore, η is the free surface elevation with respect to the undisturbed water level $z = 0$, g is the gravitational acceleration and $\check{A}_{vn}$ is a constant vertical eddy viscosity coefficient, to be determined, which has a different value for subtidal ($n = 0$) and M_2 ($n = 1$) motion. Using a depth-uniform constant eddy viscosity is most applicable for partially to well-mixed estuaries, not strongly stratified ones. The boundary conditions for each harmonic read

$$\check{A}_{vn}\frac{\partial u_n}{\partial z} = 0 \quad \text{and} \quad w_n = \frac{\partial \eta_n}{\partial t} \quad \text{at} \quad z = 0, \tag{2.2.3a}$$

$$\check{A}_{vn}\frac{\partial u_n}{\partial z} = \check{s}_{fn}u_n \quad \text{and} \quad w_n = 0 \quad \text{at} \quad z = -H, \tag{2.2.3b}$$

where $\check{s}_{fn}$ is the slip parameter, which, like $\check{A}_{vn}$ is different for the subtidal and M_2 motion, to be determined. It is assumed that there is no wind stress at the free surface and a linearised kinematic boundary condition is applied (Eq. (2.2.3a)). The condition for this linearisation to be valid is that sea surface amplitudes are much smaller than the mean depth (Chernetsky et al., 2010). The partial slip bottom boundary condition is used (Eq. (2.2.3b)) (Maas and van Haren, 1987, Schramkowski and de Swart, 2002).

Tidal sea surface elevations with a single radian frequency ω are prescribed at all seaward boundaries and a constant fresh water discharge Q is assumed at the tidal limit. At each branching point, the actual level of the sea surface η is assumed to be continuous and the fluid obeys mass conservation. This results

in

$$\eta_{n,j} = \delta_{n1} Z_j \cos(\omega t - \phi_j), \qquad \text{at} \quad x = L_j \quad \text{for sea channels,} \tag{2.2.4a}$$

$$B_j \int_{-H_j}^{0} u_{n,j} \mathrm{d}z = \delta_{n0}\, Q_j, \qquad \text{at} \quad x = 0 \quad \text{for river channels,} \tag{2.2.4b}$$

$$\eta_{n,j} = \eta_{n,k}, \qquad \text{at branching points } v_i, \quad j,k \in v_i, \tag{2.2.4c}$$

$$\sum_{j \in I_i} B_j \int_{-H_j}^{0} u_{n,j} \mathrm{d}z = \sum_{j \in O_i} B_j \int_{-H_j}^{0} u_{n,j} \mathrm{d}z, \qquad \text{at branching points } v_i, \quad j \in v_i, \tag{2.2.4d}$$

with Z_j and ϕ_j are the prescribed tidal amplitude and phase at the sea boundaries. Eqs. (2.2.4c) and (2.2.4d) mean that at the branching points sea level is continuous and mass is conserved. Here, ν_i is a set of indices of channels that connect at branching point i. The index set ν_i is further decomposed into I_i and O_i, which respectively contain indices of channels in which the fluid flows towards or away from branching point v_i. A specific example of this network labelling is given in Fig. 2.1.

2.2.2 Turbulence model

The values of effective eddy viscosities and slip parameters are realistically different for each harmonic component n (e.g., Godin, 1991, 1999). To determine these, it is assumed that the total energy dissipation in each harmonic component is the same as when using a space- and time-dependent turbulence closure. Hence, this method may be regarded as a width-averaged extension of the Lorentz linearisation method (Lorentz, 1926, Zimmerman, 1982). Denote the averaging over a channel and one tidal cycle by an underline, the mean energy dissipation due to the last term in the momentum equation Eq. (2.2.2a) is

$$\check{D}_n = \check{A}_{vn} \left(\frac{1}{HLT} \int_0^T \int_{-H}^{0} \int_0^L \left(\frac{\partial u_n}{\partial z} \right)^2 \mathrm{d}x\, \mathrm{d}z\, \mathrm{d}t \right) = \check{A}_{vn} \underline{\left(\frac{\partial u_n}{\partial z} \right)^2}, \tag{2.2.5}$$

where T is the period of one tidal cycle. In the model, stresses have been related to constants $\check{A}_{vn}$ and $\check{s}_{fn}$, whereas in reality, these parameters depend on space and time. Therefore, eddy viscosity in the space- and time-dependent turbulence model is parameterised by the Prandtl mixing length hypothesis

(Bradshaw, 1974)

$$A_v(x,z,t) = l^2\left|\frac{\partial u}{\partial z}\right|. \tag{2.2.6}$$

Here, u is the local velocity that depends on both space and time, and l is the mixing length, which is usually assumed to be proportional to the distance to the wall for a wall-bounded flow (Kundu et al., 2016). In this study, a parabolic profile is assumed (for a detailed discussion of this profile see Chen and de Swart (2016))

$$l = \begin{cases} (\zeta+1)\Big(\frac{\zeta_h}{2+\zeta_h}-\zeta\Big)H, & -1 \le \zeta \le \zeta_h, \\ (\zeta_h+1)\Big(\frac{\zeta_h}{2+\zeta_h}-\zeta_h\Big)\Big(\frac{\zeta}{\zeta_h}\Big)^2 H, & \zeta_h < \zeta \le 0, \end{cases} \tag{2.2.7}$$

where $\zeta = \frac{z}{H}$ is the scaled depth and ζ_h is an input parameter that indicates the location of the boundary between the upper and the lower layer. The value of ζ_h is near the depth at which the eddy viscosity attains the maximum. Note that Eq. (2.2.7) only parametrically accounts for the effects of stratification on turbulence through calibration of ζ_h.

The local kinematic internal stress is

$$\tau = A_v\frac{\partial u}{\partial z}. \tag{2.2.8}$$

A harmonic truncation is applied to the local kinematic internal stress so that it is decomposed into different harmonic components (for details see S3.2),

$$\tau = \tau_0(x,z) + \tau_1(x,z,t). \tag{2.2.9}$$

The mean energy dissipation attained by the space- and time-dependent turbulence closure is therefore $D_n = \underline{\tau_n\frac{\partial u_n}{\partial z}}$. This is required to equal $\check{D}_n$ (Eq. (2.2.5)). Hence, $\check{A}_{vn}$ is determined as

$$\check{A}_{vn} = \frac{\underline{\tau_n\frac{\partial u_n}{\partial z}}}{\underline{\Big(\frac{\partial u_n}{\partial z}\Big)^2}}. \tag{2.2.10}$$

The mean energy dissipation at the bottom due to the boundary condition in Eq. (2.2.3b) is

$$\check{D}_{bn} = \check{s}_{fn}\big(\underline{u_{bn}}\big)^2, \tag{2.2.11}$$

where u_b is the local bottom velocity. In the space- and time-dependent turbulence closure, the bottom slip parameter is modelled by

$$s_f = C_{100}|u_b|, \tag{2.2.12}$$

where C_{100} is a drag coefficient that depends on the bottom type. The local bottom stress is also decomposed into different harmonic components

$$\tau_b = s_f u_b = \tau_{b0}(x) + \tau_{b1}(x,t). \tag{2.2.13}$$

The corresponding mean energy dissipation is therefore $D_{bn} = \underline{\tau_{bn} u_{bn}}$. This is required to equal $\check{D}_{bn}$. Hence, the constant slip parameters are determined as

$$\check{s}_{fn} = \frac{\underline{\tau_{bn} u_{bn}}}{\underline{u_{bn}^2}}. \tag{2.2.14}$$

In this study, both eddy viscosities and slip parameters are called friction parameters that are related to internal and bottom frictions. The internal friction is $\frac{\partial \tau}{\partial z}$ and its mean value is the same as the mean value of the last term in Eq. (2.2.2a) because of the turbulence model. Whereas the bottom friction is defined as $\frac{\tau_b}{H}$, which is the stress that is experienced by the depth-averaged current.

2.2.3 Definition of river water transport

It follows, from the integration of the continuity equation for the river flow over depth and application of the boundary conditions $w_0 = 0$ at $z = 0$ and $z = -H$, that

$$\frac{\partial}{\partial x}\left[B_j(x)\int_{-H_j}^{0} u_{0,j}\,\mathrm{d}z\right] = 0. \tag{2.2.15}$$

The quantity between the square brackets is therefore a constant in each channel and defined to be the river water transport Q_j of each channel. The values of Q_j are determined by the conditions at the branching points.

2.2.4 Model solutions

The solutions of system (2.2.2)-(2.2.4) are derived in Section S4.1. Those for river flow read (for each channel)

$$u_0(x,z) = \frac{gH^2}{\check{A}_{v0}}\left[\frac{1}{2}\left(\zeta^2 - 1\right) - r\right]\frac{\mathrm{d}\eta_0}{\mathrm{d}x} = \frac{Q}{B(x)H}\left(\frac{1}{\frac{1}{3}+r}\right)\left[\frac{1}{2}\left(1-\zeta^2\right) + r\right], \tag{2.2.16a}$$

$$\frac{\mathrm{d}\eta_0}{\mathrm{d}x} = -\frac{Q\check{A}_{v0}}{gB(x)H^3\left(\frac{1}{3}+r\right)}, \tag{2.2.16b}$$

where $r^{-1} = \frac{H\check{s}_{f0}}{\check{A}_{v0}}$ is a dimensionless slip parameter. In each channel, the constant river water transport Q (except for river channels in which river discharge is prescribed) and the elevation at the beginning point of the channel, are determined by the boundary conditions (Eq. 2.2.4b).

The solutions for the tidal flow velocities and elevation are

$$(u_1, w_1) = \mathrm{Re}\{(\hat{u}_1, \hat{w}_1)e^{-i\omega t}\}, \quad \eta_1 = \mathrm{Re}\{\hat{\eta}_1 e^{-i\omega t}\}, \tag{2.2.17}$$

where a hat denotes the complex amplitude that determines the spatial structure of each variable. The variables $\hat{u}_1$, $\hat{w}_1$ are functions of x and z and $\hat{\eta}_1$ depends only on x. The expressions for the complex amplitudes read

$$\hat{u}_1 = -\frac{ig}{\omega}\left[1 - \beta\cosh(\gamma z)\right]\frac{\mathrm{d}\hat{\eta}_1}{\mathrm{d}x}, \tag{2.2.18a}$$

$$\hat{w}_1 = \frac{ig}{\omega}\left[z - \frac{\beta}{\gamma}\sinh(\gamma z)\right]\left(\frac{\mathrm{d}^2\hat{\eta}_1}{\mathrm{d}x^2} + \frac{1}{L_b}\frac{\mathrm{d}\hat{\eta}_1}{\mathrm{d}x}\right) - i\omega\hat{\eta}_1, \tag{2.2.18b}$$

$$\hat{\eta}_1 = e^{-\frac{1}{2L_b}x}\left(C_1 e^{d_0 x} + C_2 e^{-d_0 x}\right), \tag{2.2.18c}$$

with

$$\beta = \frac{1}{\cosh(\gamma H) + \frac{\check{A}_{v1}}{\check{s}_{f1}}\gamma\sinh(\gamma H)} \quad \text{and} \quad \gamma = \sqrt{-\frac{i\omega}{\check{A}_{v1}}}. \tag{2.2.19}$$

Note that $|\gamma|^{-1}$ is the Stokes depth that describes the height of frictional influence (Souza, 2013). The integration constants C_1 and C_2 are determined by the boundary conditions. The complex wave number d_0 is given by

$$d_0 = \sqrt{\left(\frac{1}{2L_b}\right)^2 - \frac{\omega^2}{gH\left(1 - \frac{\beta\sinh(\gamma H)}{\gamma H}\right)}}. \tag{2.2.20}$$

There are two unknown constants in both river (η_0 and Q) and tidal flows (C_1 and C_2). For each flow component, all unknown constants are solved simultaneously with the boundary and matching conditions (Eq. (2.2.4)). Values for eddy viscosity and slip parameter of both river and tidal flow are obtained iteratively. Starting from an initial guess of their values, solutions are calculated, which yield u_0 and u_1. New estimates of $\check{A}_{vn}$ and $\check{s}_{fn}$ are then determined from Eq. (2.2.10) and Eq. (2.2.14). Then the values of the friction parameters are computed again until changes in these values are less than a user-specified tolerance (here 10^{-5}). The full solution procedure is summarized using a flow chart (see Section S6).

2.2.5 Application to the Yangtze Estuary

The Yangtze Estuary is an estuarine network that connects the Yangtze river, also known as the Chang Jiang, with the East China Sea. Prodigious natural variability can be observed in both the river and the sea. The monthly averaged Yangtze river discharge varies from 10^4 $\mathrm{m^3\,s^{-1}}$(during the dry season, May to

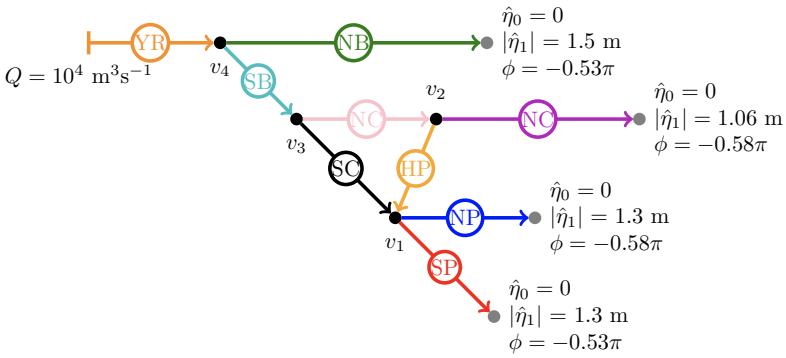

Figure 2.2: The network diagram for the Yangtze Estuary. Notations are explained in Fig. 2.1. Colour coding of channels is the same as that in subsequent plots for easy identification. In the absence of the shortcut channel, the HP is not considered. Forcing conditions are those applied to the reference case, with the shortcut channel being absent.

Channel	Label	L (km)	L_b (km)	H (m)	B_o (km)
North Branch (NB)	1	85	30	5	12
North Channel (NC)	2	60	52	7	20
North Passage (NP)	3	61	470	11	3.5
South Passage (SP)	4	54	21	7	30
South Channel (SC)	5	23	-368	9	6.2
South Branch (SB)	6	51	64	9	14
Yangtze River 1 (YR1)	7	50	206	10	6.6
Yangtze River 2 (YR2)	8	50	206	10	5.2
Yangtze River 3 (YR3)	9	50	206	10	4.1
Yangtze River 4 (YR4)	10	50	206	10	3.2
Yangtze River 5 (YR5)	11	370	206	10	2.5

Table 2.1: Geometry of the reference Yangtze Estuary network, including the channel length L, the length scale L_b at which channel width increases exponentially in the seaward direction, the water depth H and the width at the seaward boundary B_o.

	Description	Changes
1	Reference	Dry season, monthly-averaged tidal forcing
2	Wet season	River discharge $Q = 4 \times 10^4\,\mathrm{m^3\,s^{-1}}$ (Alebregtse and de Swart, 2016) Increase water depths in YR1-YR5 by 1-5 m respectively (Cai et al., 2019)
3	Spring tide	Increase the tidal amplitudes by 50% (Lu et al., 2015)
4	Shortcut channel	Add Hengsha Passage (Kuang et al., 2014a)
5	Before DWP	$H = 7$ m and $L_b = 60$ km in the North Passage (Alebregtse and de Swart, 2016)
6	Sea level rise	Undisturbed water depth +2 m (Kuang et al., 2017)

Table 2.2: List of experiments

October) to $4 \times 10^4\,\mathrm{m^3\,s^{-1}}$ (during the wet season, November to April) with an annual average of 28300 $\mathrm{m^3\,s^{-1}}$(Yang et al., 2015). During spring tide, the tidal range at the entrance is about 4.62 m, while the average tidal range is 2.67 m (Zhang et al., 2016). Due to large scale human interventions, such as the DWP in the North Passage and the construction of Qingcaosha Freshwater Reservoir, both tidal currents and the distribution of river water over different channels changed.

The default case considered in this study is the dry season (January 2014), during the mean tide, after the construction of the DWP and without the Hengsha Passage. The only external tide is the semi-diurnal tide with angular frequency $\omega = 1.4 \times 10^{-4}\,\mathrm{rad\,s^{-1}}$. Fig. 2.2 shows the network pattern of the Yangtze Estuary and indicates the values of forcing parameters. The parameters for all channels are given in Table 2.1. The modelled tides from the reference case will be first compared with observed tides. Next, several scenarios that mimic the wet season, spring/neap tide, a shortcut channel, the situation before DWP, and sea level rise will be compared to the reference case to investigate their effects on tides, river, and river water transport. Table 2.2 provides the list of experiments. Finally, for all cases, the bottom drag coefficient is $C_{100} = 0.0022$ corresponding to muddy beds (Soulsby, 1997). By fitting the modelled tidal elevation amplitudes to observed amplitudes, it was found that $\zeta_h = -0.67$, meaning that the eddy viscosity is maximum near $-0.67H$ for all channels and thereby also determines the magnitude of the eddy viscosity.

2.3 Results

2.3.1 Reference case

Fig. 2.3 shows the friction parameters of each channel for the reference case. The depth of each channel is attached to each channel in panel (a). Although

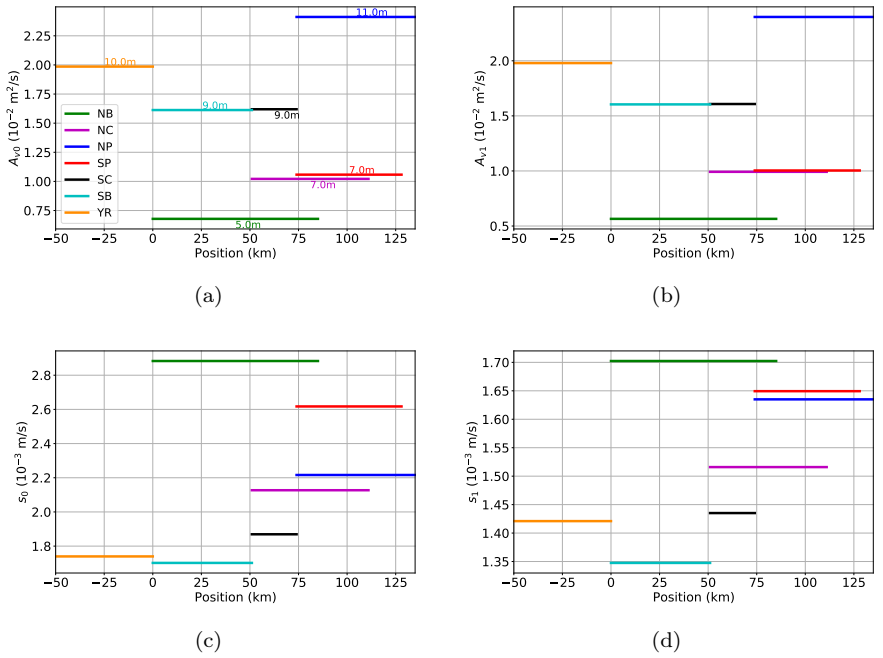

Figure 2.3: a. Eddy viscosity $\check{A}_{v0}$ of river flow versus position in the network. Here, $x = 0$ is the location of the most upstream branching point. b. As a, but for eddy viscosity $\check{A}_{v1}$ of tidal flow. c. As a, but for slip parameter $\check{s}_0$ of river flow. d. As c, but for slip parameter $\check{s}_1$ of tidal flow.

	Station name		Station name		Station name
1	Jiangyin	6	Nanmengang	11	Beicaozhong
2	Tianshengang	7	Shidongkou	12	Niupijiao
3	Hupu	8	Wusong	13	Zhongjun
4	Baimaokou	9	Changxing	14	Nancaodong
5	Qinglonggang	10	Hengsha	15	Sheshan

Table 2.3: Tidal stations of which data have been used to verify the model.

the formulation of eddy viscosity (Eqs. (2.2.6)-(2.2.7)) scales with both depth and velocity, the magnitudes of eddy viscosities turn out to be characterised mostly by the water depths. The eddy viscosities for the river and tidal flow (panel a and b) are therefore the largest in the North Passage (NP, the deepest branch) and the smallest in the North Branch (NB, the shallowest branch).

The slip parameters for the river and tidal flow (panel c and d) are the largest in the North Branch (NB) and the smallest in the South Branch (SB).

Fig. 2.4 (a) and (b) compare the amplitudes and phases of M_2 sea surface elevations of the reference case with those derived from harmonic analysis of observed sea surface variations. Dots are data from National Marine Data and Information Service (2013), retrieved from tidal tables for January 2014 of 15 different water stations listed in Table 2.3. These are the values used to calibrate the model. Upward triangles show results from Lu et al. (2015), who applied harmonic analysis to observed water levels. There is good agreement between modelled and observed tides (see also data presented in Guo et al. (2015), which is plotted in Alebregtse and de Swart (2016)). The tidal damping and amplification in the North Branch (NB) and the South Branch (SB) agree with the result in Zhang et al. (2012): in the NB, the tidal wave is first amplified and then damped, whereas in the SB, the tidal wave is damped. The slopes of phase curves in panel (b) are proportional to the phase speed ($c = \omega/\frac{\mathrm{d}\phi}{\mathrm{d}x}$) of the tidal wave. Typical values of the phase speed, depending on the water depth and on the values of the friction parameters, range from 7 to $10\,\mathrm{m\,s^{-1}}$. Depth-averaged tidal (M_2) current amplitudes (panel c) are almost identical to those from the 1D model of Alebregtse and de Swart (2016). The amplifications in both the North Branch (NB) and the South Passage (SP) are due to the strong width convergence. The amplification in the SP is also observed by Li et al. (2018). For all channels, the surface elevations due to the river flow (panel d) and due to resonance related to wave reflection decrease from the river to the sea. For most channels, the river flow velocities (panel e) exponentially decrease in magnitude towards the sea due to the seaward increasing channel width. The width of the South Channel decreases in the seaward direction and therefore the river flow is amplified in that channel. The North Passage has a nearly constant width (large value of parameter L_b), so the river current is almost constant. River water is mostly transported through the South Branch (panel f), after

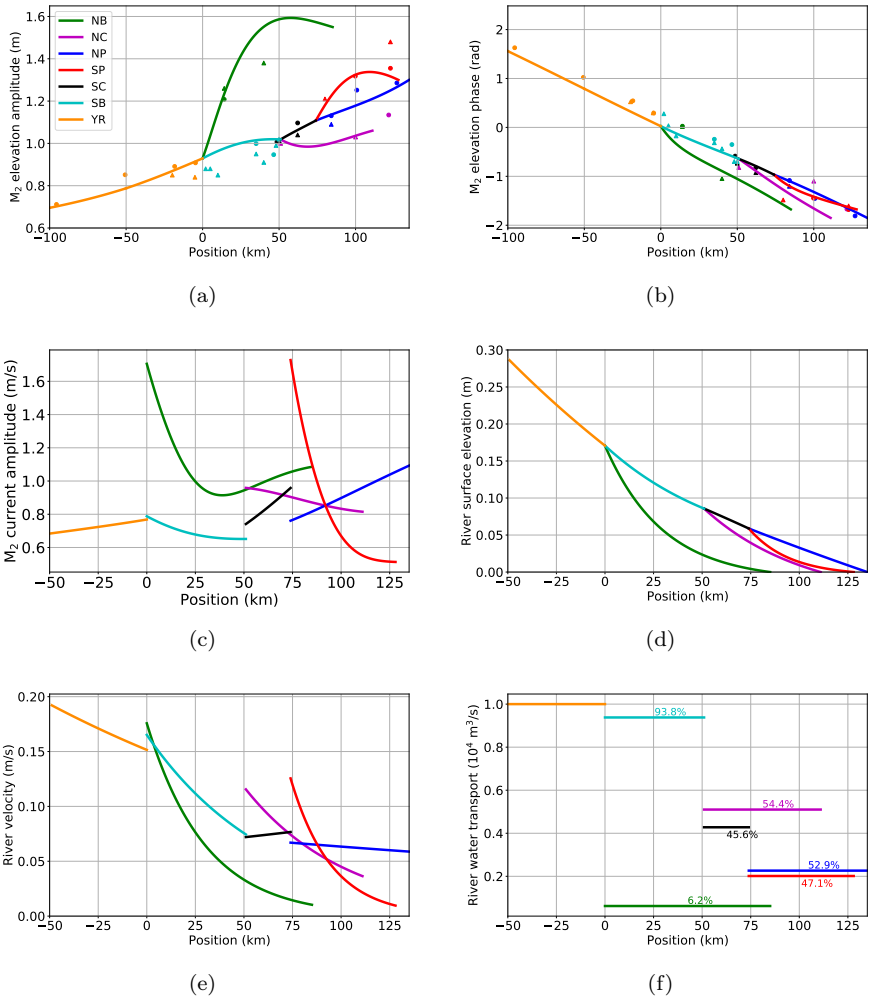

Figure 2.4: a. M_2 tidal elevation amplitude versus position in the network of the reference case. Here, solid lines are the model results and dots are the data from the tidal table. b. As a, but for tidal elevation phase. c. As a, but for tidal discharge amplitudes. d. As a, but for surface elevation due to the river flow. e. As a, but for river flow velocity. f. As a, but for river water transport. Note that x-coordinate for panel a and b is different due to the location of the data point near $x = -100\,\mathrm{km}$.

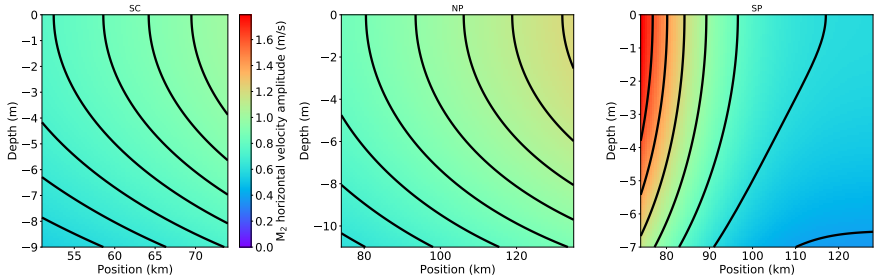

Figure 2.5: Spatial structure of horizontal tidal current amplitude in the South Channel (a), the North Passage (b) and the South Passage (c) in the x-z plane. Colour is the horizontal tidal velocity amplitude.

which the river water is distributed nearly evenly over subsequent channels. Percentages next to the lines indicate the river water diversion ratio, computed by the model. It is defined as the ratio of river water transport in one channel to the river water transport in its upstream channel. It should be noted that the river water diversion ratio is different from the net water diversion ratio as in e.g., Alebregtse and de Swart (2016), which additionally includes the net transport due to tides and nonlinear processes and is therefore comparable to the observed water diversion.

The vertical distribution of tidal velocity amplitude (Fig. 2.5) reveals that tidal current is the strongest near the surface, values can be up to $1.8\,\mathrm{m\,s^{-1}}$. Both the vertical and the horizontal structure of the tidal current amplitudes differ from channel to channel. Viewing upstream, modelled tidal current amplitude decreases in the North Passage and the South Channel, while it increases in the South Passage. These results agree with the results of other analytical studies (Jiang et al., 2013a, Alebregtse and de Swart, 2016), while observations suggest more longitudinal perturbations at smaller scales due to the complex geometry (Shao et al., 2017). The horizontal variation in the South Passage is much larger than that in the other two channels. At the branching point, there is a jump in tidal velocity amplitude; the tidal current amplitude in the South Passage is about twice as large as those of the North Passage and the South Channel. The large tidal current in the South Passage near the branching point is the result of its strong longitudinal width convergence. However, its width and depth are the smallest among the three channels that join at the branching point, so it has the least cross-section area. This in turn leads to the jump in the velocity at the junction of the NP, the SP and the SC.

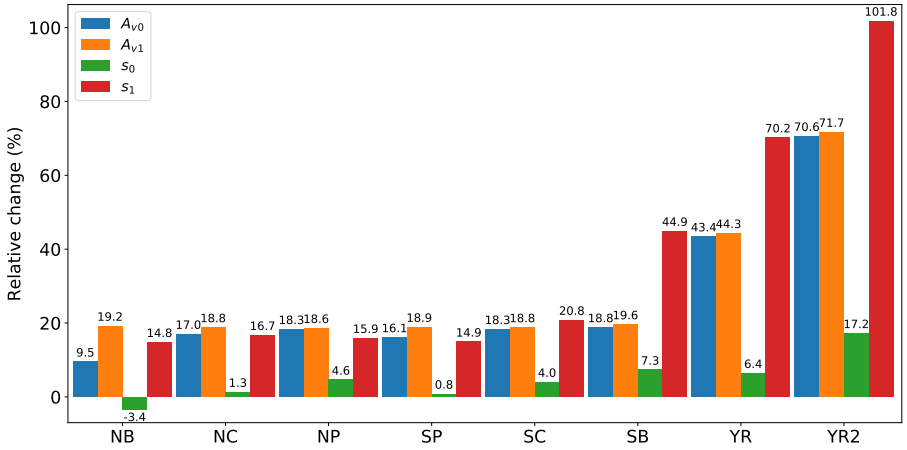

Figure 2.6: Relative changes in $\check{A}_{v0}$ (blue), $\check{A}_{v1}$ (orange), $\check{s}_0$ (green) and $\check{s}_1$ (red) during the wet season with respect to the dry season for the different channels.

2.3.2 Comparison of the wet season with dry season

During the wet season (river discharge is four times higher than that in the dry season), the water level set-up in the Yangtze River (YR) is significant and should be accounted for in order to get correctly simulated tidal propagation (see also Dijkstra et al., 2017a) Therefore depths of the YR1 to the YR5 are increased by 1-5 metres respectively. These depth modifications are based on the observed variations in the mean water level in relation to the river discharge (Guo et al., 2015, Cai et al., 2019). Note that although the increase in water depth is not continuous, the free surface is guaranteed to be continuous by the matching condition (Eq. (2.2.4c)).

The relative changes in friction parameters during the wet season with respect to the dry season are shown in Fig. 2.6. With larger river discharge, the friction parameters for both river and tide increase, except for the slip parameter of the river flow in the North Branch (NB). This influence decreases downstream and is much smaller on the slip parameter for the river flow. The increase in friction parameters is mostly because of the stronger river-tide interaction due to the larger river current, as the influence of larger discharge on water depth is negligible in the downstream part of the Yangtze Estuary.

Fig. 2.7 shows that the amplitudes of both tidal surface elevations and depth-averaged tidal currents (panel a and c) are smaller in the wet season than in the dry season and the overall dampening increases upstream. This result is consistent with that of Alebregtse and de Swart (2016). Positive phase differences (panel b) in the tidal surface elevations imply that the tidal waves travel slower during the wet season. Under the same tidal forcing, high water arrives at the first branching point about 13 minutes later ($1\,\mathrm{rad} \approx 7114\,\mathrm{s}$).

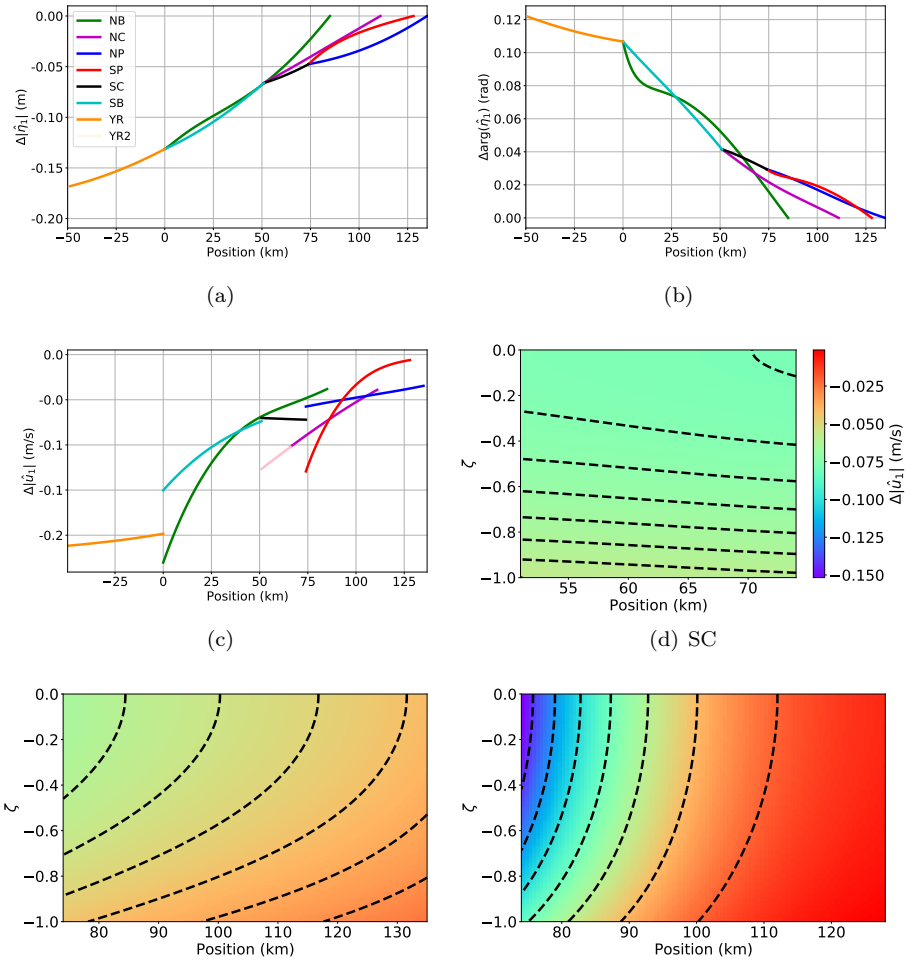

Figure 2.7: a. Difference between tidal elevation amplitude during the wet and dry season versus position in the network. b. As a, but for tidal elevation phase. c. As a, but for tidal discharge amplitude. d. Difference between the horizontal tidal current amplitude in the South Channel (SC) during the wet and the dry season in the x-ζ plane. Colour denotes the difference in the tidal velocity amplitude. e. As d, but for the North Passage (NP). f. As d, but for the South Passage (SP).

The differences between the horizontal tidal velocity amplitudes during the wet and dry season for longitudinal sections in the South Channel, the North Passage, and the South Passage are plotted in panels (d), (e), and (f). To make variables comparable between two scenarios at different depths in the cases that channel depths are adjusted, the ζ-coordinate ($\zeta = \frac{z}{H}$) is used instead of the z-coordinate in the difference plots. Here, the water depths in the SC, the NP and the SP are the same for both dry and wet seasons. Solid lines are levels with positive values and dashed lines are levels with negative values. Horizontal tidal velocity amplitudes are generally smaller during the wet season. At the sea boundaries of the North Passage and the South Passage, these amplitudes are hardly affected by the larger river discharge. For most locations, the change in tidal current amplitude at the surface is larger than that at the bottom.

Plots of the difference between the elevation and current due to the river, as well as the river water transport during the wet season and the dry season are shown in Fig. S2 of the Supplementary information (SI). It appears that the spatial patterns of these variables during the wet season are similar to those during the dry season, but at larger magnitudes.

Fig. S3 shows the sensitivity of selected variables to continuous change in the river discharge from the YR. As river discharge increases, tidal elevation amplitudes (panel a) decrease at all branching points and the time tidal waves need to travel to the branching points (panel b) increases. River set-up (panel c) at all branching points and river water transport (panel d) in each channel linearly increase when the river discharge from the YR is increased.

2.3.3 Comparison of spring tide with mean tide

By seeing the M_2 tide as a representative semi-diurnal amplitude, spring tide may be considered by increasing the amplitude of the M_2 tide to the amplitude of the semi-diurnal water motion a few days around the spring tide. This approach follows what is used in other studies (Valle-Levinson, 2010, Geyer and MacCready, 2014). During spring tide (external tidal amplitude is 50% larger than the mean tide), all friction parameters have larger values. For each channel, the relative changes of friction parameters for river flow are larger than those for tidal flow. The largest change in friction parameters (an increase of about 40%) is observed in the North Passage and in the South Passage.

Larger tidal forcing leads to the increase of both tidal elevation and tidal current amplitudes (Fig. 2.8 panel a and c). Nonetheless, the tidal waves travel slower, because of the larger friction (panel b). For example, the high water at the first branching point ($x = 0$) arrives 11 minutes later during spring tide than during mean tide in the model. When comparing the panel (d)-(f) with those of Fig. 2.5, it appears that the pattern of horizontal tidal velocity amplitudes does not change from mean tide to spring tide, only amplitudes get larger. The maximum increase is observed at the landward side of the South Passage. River flow is almost unaffected by the larger tidal forcings.

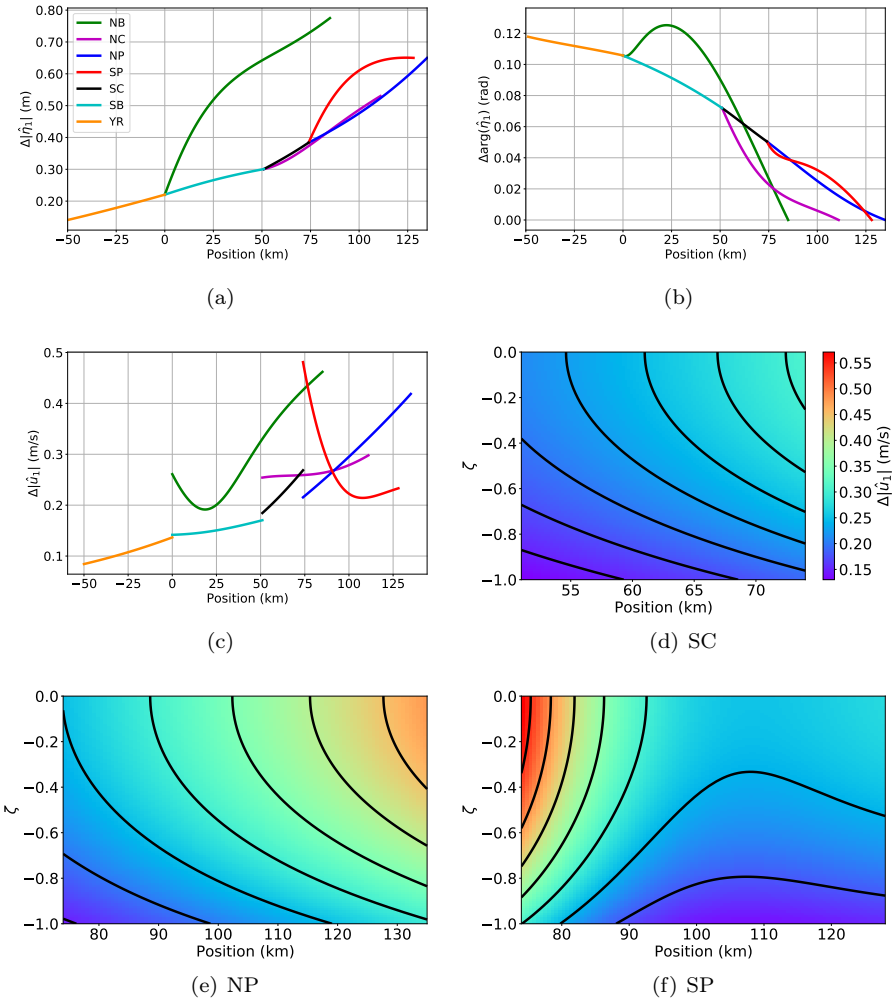

Figure 2.8: As Fig. 2.7, but for the difference between spring tide and mean tide.

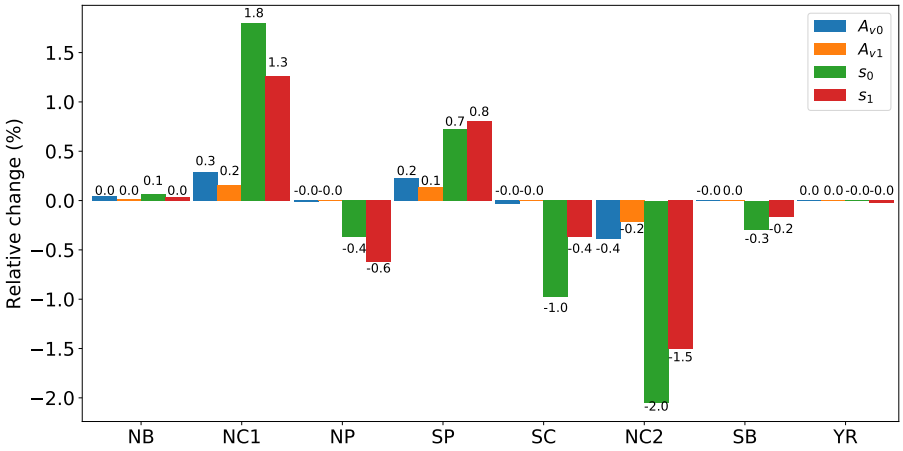

Figure 2.9: As Fig. 2.6, but for the relative changes in friction parameters including the HP with respect to the reference case.

The model is also run for the neap tide (50% lower tidal forcing), which shows changes, with respect to mean tide, that are opposite to those for spring tide: friction parameters decrease, tides travel faster, tidal elevation, and discharge amplitudes increase.

Fig. S4 shows the sensitivity of variables, as in Fig. S3, to values of the tidal forcing that occur during a spring-neap cycle. For larger tidal forcing, tidal elevation amplitudes (panel a) and river set-up (panel c) at the branching point increase. It takes longer for tidal waves to travel to the branching points (panel b). River water transport (panel d) is almost unaffected by the tidal forcing.

2.3.4 Effects of a shortcut channel (Hengsha Passage)

In this study, the presence of the Hengsha Passage (HP) splits the North Channel (NC) into two channels: the upstream part NC1 and the downstream part NC2. In the HP, positive x is defined to be from North to South (from the North Channel at $x = 66\,\text{km}$ to the branching point of the North Passage (NP), the South Passage (SP) and the South Channel (SC) at $x = 74\,\text{km}$). Since all friction parameters are channel-averaged, splitting the NC affects the averaging, thereby resulting in different values of eddy viscosities and slip parameters. To distinguish the effects of the HP from the effects of splitting the NC, results are first obtained by splitting the NC into two parts. It turns out that the effect of splitting the NC is negligible. Then, the HP is added and the results are compared to those obtained from split NC.

It is observed in this model that, in the HP, the tidal current amplitudes are

less than $1\,\mathrm{m\,s^{-1}}$, river velocity is small and the river water is transported from the NP to the NC at the rate of about $200\,\mathrm{m^3\,s^{-1}}$. The influence of the HP on friction parameters in other channels is shown in Fig. 2.9. Friction parameters in the channels connected to the HP are affected most by the HP, the effect is minor; only 1-2% and hence negligible within the accuracy of this model.

The effects of the HP on the tide, river, and river water transport are also mainly in the channels connected to it, i.e., the NC, the NP, the SP, and the SC (Fig. S5). Due to the presence of the HP, the tidal amplitude at the branching point of the SC, the NP, and the SP decreases by a few centimetres (panel a) and the tidal amplitude at the junction of the two parts of NC increases. Including the HP, the tidal wave travels slower in the seaward part of the NC (panel b) and faster in the landward part of the NC. These changes lie within the uncertainty margin of the model. Tidal discharge amplitude (panel c) increases in the seaward part of the NC and decreases in the landward part of the NC.

Surface elevations due to the river (panel d) and the river current (panel e) are nearly unaffected by the HP. The changes in the river current imply that the additional river water transport from the SC first enters the HP passages and is subsequently distributed over the two parts of the NC. Moreover, it can be seen from the difference in river water transport (panel f) that the amount of river water transported by the HP mostly goes back to the SC, although the amount is small.

2.3.5 Effects of the Deep Waterway Project (DWP)

The DWP altered the geometric characteristics of the North Passage (NP) in two aspects: the construction of two training walls that significantly reduced the channel convergence and dredging from 7 m (Jiang et al., 2012) to 11 m (Li et al., 2019).

The effects of the DWP on the friction parameters are mainly in the NP itself (Fig. S6). Before the DWP, eddy viscosities for both tide and river in the NP were about 58% smaller than the reference case because eddy viscosities scale with depth. The relative changes in friction parameters in other channels are small.

Tidal elevation amplitudes in all channels were slightly lower than those in the present-day situation (Fig. S7a) and the tidal waves travelled slower in most channels (panel b), except for the seaward part of the NP. The upstream amplification of tidal current amplitude was much stronger in the NP (panel c), due to the strong width convergence. Elevation (panel d), velocity (panel e), and transport (panel f) due to the river were similar to those of the reference case. The effects of DWP on the horizontal and vertical structure of tidal current amplitudes are shown in Fig. 2.10. Panels (a) and (c) are for the South Channel and for the South Passage, in both of which the differences are small. In the NP (panel b), tidal velocity amplitudes in the seaward part significantly increased after the DWP, while in the landward part they decreased. Before

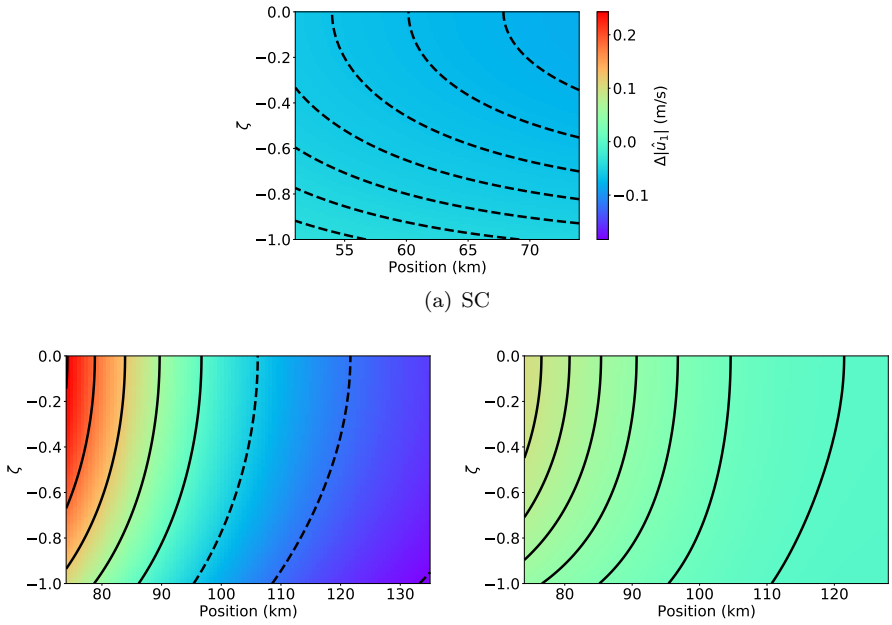

(a) SC

(b) NP

(c) SP

Figure 2.10: As Fig. 2.7 d-f, but for the difference between horizontal tidal velocity amplitudes prior to and after the Deep Waterway Project (DWP).

the DWP, the near surface tidal velocity amplitude in the NP was more than $0.2\,\mathrm{m\,s^{-1}}$ larger at the branching point and about $0.2\,\mathrm{m\,s^{-1}}$ smaller at the sea.

2.3.6 Effects of sea level rise

In this study, 2 m seal level rise (SLR) is simplified to a 2 m increase in water depths in all channels. Here, 2 m is the suggested maximum SLR based on the study of Kuang et al. (2014b). Tidal limit moves further upstream due to larger water depth. However, this does not affect the tidal characteristics in the downstream channels. The eddy viscosities for both tide and river increase (Fig. S8). The increases in the eddy viscosity for the river flow are slightly larger than that for the tidal flow for all channels with a maximum increase of over 56% in the NB and a minimum increase of about 14% in the NP. The slip parameters for river flow slightly decrease in the NP and the SP and increase in other channels.

With the same tidal forcings, tidal elevation amplitudes within the estuarine network will be enhanced by 2 m SLR (Fig. 2.11 a) and the amplification is stronger upstream. There is a fair agreement between modelled tidal am-

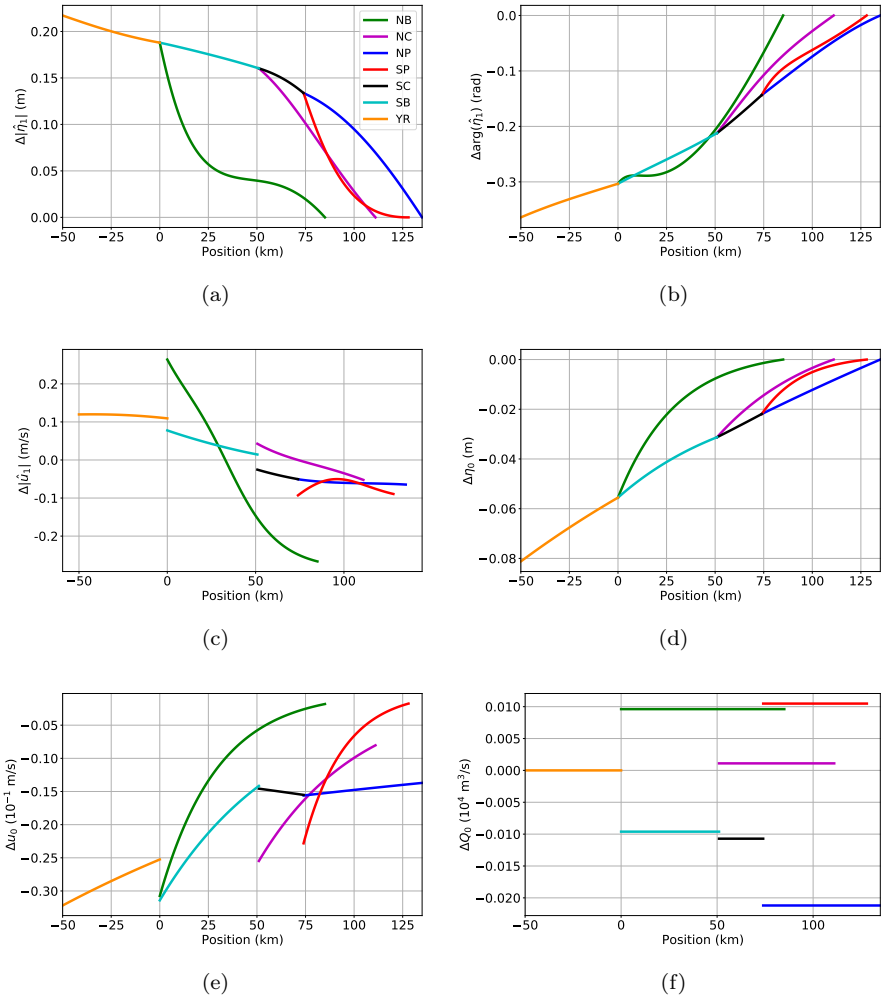

Figure 2.11: As Fig. 2.7, but for the difference between values of variables in the situation for 2 m sea level rise and those in the reference case.

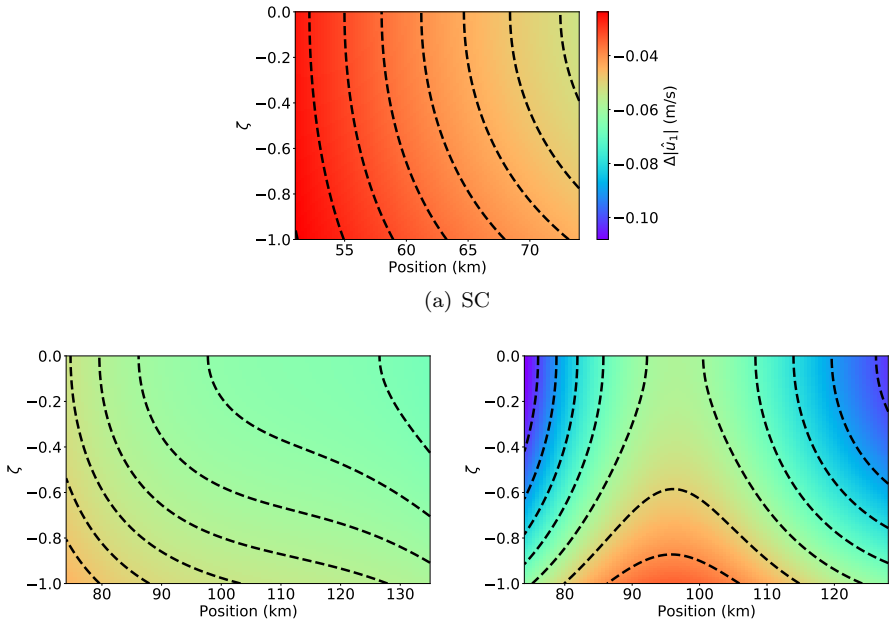

(a) SC

(b) NP

(c) SP

Figure 2.12: As Fig. 2.7 d-f, but for the difference between horizontal tidal velocity amplitudes after 2 m sea level rise and those in the reference case (no sea level rise).

plitudes and those obtained with the numerical model of Kuang et al. (2014b) under 2 m SLR. The tidal waves travel faster than those in the reference case (panel b). For example, the high water arrives about 32 minutes earlier at the first branching point $x = 0$. However, the numerical results from Kuang et al. (2014b) predict the advancement of time of high water due to 2 m SLR is about 45 minutes. This difference is most likely the consequence of simplified geometry. Changes in tidal current amplitudes are small except for that in the North Branch (NB) (panel c). Due to 2 m SLR, tidal current amplitudes increase in upstream of the North Branch and the South Branch and decreases in the North Passage are consistent with the findings of Kuang et al. (2014b). Surface elevation due to river (panel d) and the river flow velocity (panel e) slightly decrease. The NB and the SP receive a larger fraction of river water, about $100\,\mathrm{m^3\,s^{-1}}$, after SLR compared to the reference case (panel f). Horizontal tidal current amplitudes slightly decrease in the SC, the NP, and the SP (Fig. 2.11), with a maximum decrease of $0.1\,\mathrm{m\,s^{-1}}$ at the sea boundary of the SP at the surface.

Fig. S9 shows variables, as in Fig. S3, as continuous functions of imposed sea level rise. As the sea level rises, up to 2 m, the tidal elevation amplitudes

increase (panel a) and the river set-ups (panel c) decrease, tidal waves travel faster (panel b), and river water transport is hardly affected by sea level rise (panel d).

2.4 Discussion

This section will first summarise the key findings of each experiment and explain the observed changes where necessary. Meanwhile, results will be compared with those reported in other studies. Finally, some limitations of the model will be discussed.

2.4.1 Key findings

Wet versus dry season

Volumetric river discharge is proportional to the cross-sectionally averaged current, channel width and depth ($Q = UBH$). In our study, B was assumed to be independent of discharge and mean depths in the river channels were adjusted manually according to information provided by Cai et al. (2019). Hence, the results are for velocity and its vertical structure. Our results (Fig. 2.6) reveal that the vertical profiles of the river current are hardly affected by the larger discharge. This is because friction parameters affecting river flow hardly change between the wet and dry seasons. However, the eddy viscosities and slip parameters affecting the tide are larger during the wet season due to both enhanced internal stress and bottom stress generated by the tide-river interaction. This can be seen from Eq. (S3.9): the contribution of river velocity shear to the internal stress of tidal flow is three times larger than its contribution to the internal stress of the river flow. Due to this increased friction, the tidal wave decays faster and it travels slower when river discharge increases. These findings are consistent with those of earlier studies (e.g., Guo et al., 2015, Cai et al., 2019).

The effect of enhanced tidal decay due to enhanced frictions during the wet season is especially notable in the more upstream branches (Fig. 2.7 a). In the branches close to the sea, such as the NP, the fixed boundary condition (tidal amplitude) and enhanced friction lead to an enhanced local pressure gradient, which tends to increase the velocity amplitude (Fig. 2.7 c). The combined effect of enhanced friction and local pressure gradients means that the velocity does not change much in the NP.

Mean energy dissipation in each channel (Eq. (2.2.5) and (2.2.11)), averaged over both one tidal cycle and over the entire channel, increases for larger river discharge (Fig. S10). This is consistent with earlier findings by Zhu et al. (2016). It turns out that the contribution due to the internal stress is one order of magnitude smaller than that due to the bottom stress.

Spring tide versus mean tide

When tidal forcing increases, the ratio of friction to inertia increases, so tidal waves become more dissipative. Therefore, whether the tidal elevation amplitude becomes larger depends on the location. For the Yangtze Estuary, tidal elevation amplitudes increase with larger tidal forcing (Fig. 2.8a). Larger tidal forcing also causes enhanced tidal velocity shear (Fig. 2.8d-f), which results in larger eddy viscosities (Eqs. (2.2.6)-(2.2.7)) and hence larger internal friction. The fact that tidal waves travel slower in the network when tidal forcings are increased is thus caused by the increases in both sources of friction.

The Hengsha Passage (HP)

The overall effects of the Hengsha Passage on the tide, river and, river water transport are small and local, as was found in Section 2.3. There is an additional amount of river water that flows from the South Channel (SC) into the HP and flows back to the SC through the upstream part of the North Channel (NC2) (Fig. S5f). This explains that the most significant changes in friction parameters are in the NC2 (Fig. 2.9), i.e., the upstream part of the North Channel.

This model yields the same flow direction as that of Kuang et al. (2014a): water mass is transported from the NP to the NC during the maximum flood and from the NC to the NP during the maximum ebb. The tidal current amplitudes in the HP are smaller than those from Kuang et al. (2014a). This is because the configuration of the HP is slightly different in this study: the HP is not only connected to NP, but also the NC, the SP, and the SC. This is done to simplify the network configuration; otherwise the NP is split into a downstream part and an upstream part. With this configuration, the tidal elevation amplitudes difference between the two endpoints of the HP, which in general determines the tidal current amplitudes in the HP, is smaller than what is found by Kuang et al. (2014a). Consequently, the tidal current amplitudes in the HP are underestimated.

Effects of the Deep Waterway Project (DWP)

The results for depth-independent variables are similar to those of Alebregtse and de Swart (2016) and are also consistent with data presented in Jiang et al. (2013a). Therefore, the results are not presented in depth but are included in the SI.

Although the geometrical changes of the DWP are local (larger water depth and less width variation in NP), the intervention affected tides and river water transport in the entire network. Since the DWP involves changes in both depth and width, their effects on depth-independent variables (tidal elevation amplitudes, phases, river set-up, river current, and river water transport) are shown separately in Fig. S11. The effects of channel deepening and narrowing

were comparable in magnitude but opposite and hence compensated each other. This is because their opposite effect on the channel cross-sectional area.

Sea level rise

In this study, the sea level rise (SLR) scenario isolates the effect of depth increase only, ignoring some other effects of SLR. For example, Kuang et al. (2017) show that when SLR is 2 m, there will be about 0.2 m increase in the tidal forcing amplitudes at the open sea. In this chapter, the effects of the varying tidal forcing amplitudes have been investigated in the spring-neap modulation and therefore boundary conditions are not changed for SLR. It is also assumed that the stratification effect on eddy viscosity remains the same under SLR, and therefore the same calibration parameter as the reference case is used.

Due to a 2 m SLR and under the above assumptions, the eddy viscosities for both tide and river increase. This is because the eddy viscosity scales with the water depth (Eq. (2.2.6)). Despite the larger friction parameters, the tidal waves travel faster. The reason is that the increased undisturbed water depth leads to an increase in the shallow water wave speed $c = \sqrt{gH}$, the speed that tidal wave travels in the absence of friction. Additionally, a reduction of the set-up induced by the river is observed for 2 m SLR (Fig. S12). Eq. (2.2.16b) shows that the surface gradient is proportional to the eddy viscosity coefficient, but inversely proportional to the depth cubed. The latter effect is stronger than the former and therefore the surface gradient decreases. Since the set-up is fixed to be 0 at the sea, a smaller surface gradient leads to a smaller river set-up. For this reason, the changes in the mean depth inside the estuarine network are smaller than the imposed SLR (Fig. S13). Finally, SLR leads to weaker river velocity, because the cross-sections become larger, while the river water transport distribution in the network is hardly affected.

2.4.2 Model advantages and limitations

The exploratory nature of this model allows a fast and semi-analytical way to gain fundamental insight into the global tidal motion in networks. It has been used here to better understand the interaction between tidal propagation and friction. Additionally, it includes the distribution of river discharge, which is a contribution to the net water transport. However, the idealised nature of the model also imposes some restrictions on the interpretation of the model.

Lateral processes are omitted. These are important in estuaries that are partially to poorly mixed and that have significant lateral depth variations (e.g., Scully et al., 2009). Significant lateral flow has also been observed in the Yangtze Estuary (Li et al., 2019). The length scale being considered in this model is the tidal wavelength. This means that model results are representative for the average motion in width-averaged sense and over length scales of the order of at least 10 km. Smaller details are not resolved. Tidal flats are ne-

glected in this model, which are sinks for along-channel momentum (Hepkema et al., 2018) and have a large impact on the dynamics in the inner delta region of the Yangtze Estuary (Zhu et al., 2016).

The effect of density stratification on values of eddy viscosities (Burchard, 2002) is not accounted for. As is shown in e.g., Chen and de Swart (2016), this affects the vertical structure of the tidal current. It may result in a maximum current that does not occur at the surface, which is what is observed in e.g., the North Passage of the Yangtze Estuary (Jiang et al., 2013a).

Internally generated overtides are not modelled, which alter the semi-diurnal tidal elevation and usually arise from the nonlinear advection term and friction. Other tidal constituents such as S_2 and diurnal components are not included in the model, but can be added. The model only considers river water transport; it does not yield information about net water transport. The latter also involves net (Stokes) transport by tides, as well as transport due to residual currents induced by horizontal density gradients, tidal advection, tidal straining and wind, which are important in estuaries (Geyer and MacCready, 2014, Cheng et al., 2019) and will be considered in Chapter 3.

The time series of the horizontal flow velocity at one location in the North Passage during the wet season for spring tide is constructed from the model and compared to the measurement made by Wan and Zhao (2017) (Fig. 2.13), which is also comparable to the observation made by Li et al. (2019). Overall, there is a fair agreement between the modelled current vertical structure with that from observation, when taking into account the above-mentioned model limitations. First, the maximum flood and ebb currents from our model are smaller than observation. This is because the result from the model is width-averaged. The measurement was made in the middle of the channel and the current near the wall is supposed to be much smaller. Second, the maximum flood current in the middle of the water column near 6 h cannot be reproduced by our model. This is most likely due to the exchange flow, while the only residual flow in our model is the river. Third, the second slack tide near 8-8.5 h was not depth uniform. The phase difference at different water depths is most likely the consequence of overtides, which is not revolved in the present model.

2.5 Conclusions

This study focused on the hydrodynamic response of estuarine networks to imposed tidal forcing and river discharge, as well to changes in the response due to changes in forcing (including sea level rise) and geometrical characteristics of the network. For this, a generic, idealised 2DV estuarine network model was developed and applied to the Yangtze Estuary. The model describes primary tides and river water transport and accounts for river-tide interaction in the turbulence dissipation term. Various local and global modifications were explained via the interaction between eddy viscosity, bottom friction, and tidal

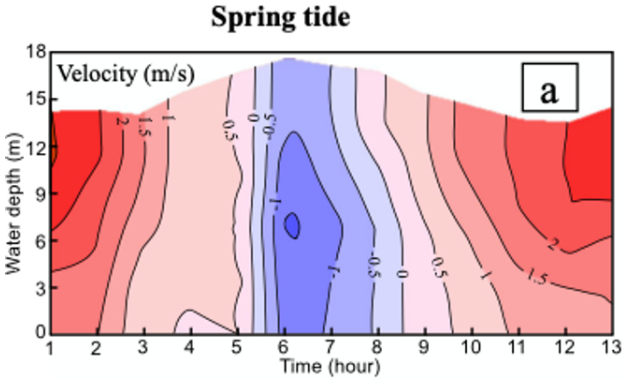

(a)

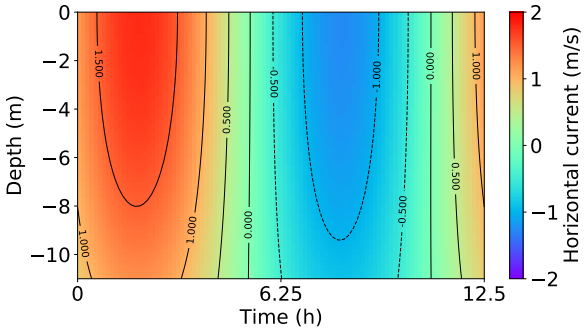

(b)

Figure 2.13: a. Observed vertical structure of the horizontal current near $x = 100$ km in the NP during the wet season for spring tide (Wan and Zhao, 2017). b. Time series reconstructed from the model under the same conditions as of a.

propagation in the network.

It turns out that the modelled tides and distribution of river water transport in the networks agree fairly well with observations and other model studies, as well as the current vertical structure. The behaviour of tides can be understood in terms of competition between friction and channel width convergence, while the distribution of river water transport is mainly controlled by the geometrical characteristics of each channel.

When river discharge is increased, the tidal wave travels slower and tidal elevations are dampened due to both larger bottom stress and internal stress. River flow is hardly affected by larger discharge; elevation and current due to the river homogeneously change with the prescribed river water discharge.

Varying the amplitude of tidal forcing at the seaward boundaries, that represents the spring-neap modulation, leads to changes in friction parameters whose values are positively correlated to the tidal forcing amplitude. When tidal forcing amplitude is increased, the tidal wave travels slower due to larger friction. The changes in tidal elevation amplitudes depend on the location, they are enhanced in the downstream part of the Yangtze Estuary. River water transport is nearly unaffected by the variation of tidal forcings.

Results are sensitive to the network geometry. If a connecting channel (Hengsha Passage) is added, changes are mainly local: it reduces the differences in both tidal elevation amplitudes and river set-up in adjacent channels and a net river water transport from the North Passage (NP) to the South Channel (SC) is observed. The effects of the Deep Waterway Project (DWP), a major intervention in which one of the channels (NP) was deepened and straightened (almost no width variations), were global. The effect of deepening was dominant while compensated by the straightening. Noticeable here is the strong increase of tidal currents in the seaward part of NP and a decline in its landward part.

Finally, a 2 m sea level rise results in larger tidal elevation amplitudes, the larger phase speed of the tidal waves and reduced river set-up with respect to the undisturbed water depth. River water transport is not sensitive to sea level rise.

3

Mechanisms controlling the distribution of net water transport in estuarine networks

This chapter is based on the article Wang, J., Dijkstra, Y. M., and de Swart, H. E. (2022) Mechanisms controlling the distribution of net water transport in estuarine networks. *Journal of Geophysical Research: Oceans* 127, e2021JC017982. https://doi.org/10.1029/2021JC017982

Abstract

Net water transport in estuaries is important for, e.g., salt intrusion and sediment dynamics. While net water transport is only determined by river run-off in single channels, in estuarine networks, it results from a complex interplay between tides and residual flows. This study aims to disentangle the various contributions of these physical drivers to net water transport in estuarine networks and investigate the sensitivities of net water transport to variable forcing conditions, interventions, and sea level rise (SLR). To this end, a processes-based perturbative network model is developed, which accounts for the vertical flow structure to resolve density-driven flow driven by a vertically well-mixed along-channel salinity gradient. Other identified drivers are river discharge and three tidal rectification processes: Stokes transport and its return flow, momentum advection, and velocity-depth asymmetry. The model is applied to the Yangtze Estuary. Net water transport due to tidal rectifications and density-driven flow can be comparable to river discharge. Specifically in the North Branch, the direction of net water transport may differ from the direction of river discharge. Varying river discharge mainly affects net water transport due to river as tide-river interaction is weak and density-driven flow is shown to be insensitive to salt intrusion. Conversely, variations in tidal amplitude strongly affect net water transport related to tidal rectification and density-driven flow. The deepening (narrowing) of one channel (Deep Waterway Project), affected the net water transport mostly through the density-driven flow (momentum advection). Furthermore, net water transport distribution in the Yangtze is insensitive to SLR up to 2 m because of the effects of SLR on transport due to different drivers compensating for each other.

3.1 Introduction

Knowledge of net (i.e., subtidal) water transport in estuaries is important because it strongly impacts water quality and ecological processes (Cloern et al., 2016). For a single-channel estuary in equilibrium, the net transport is determined by the river run-off. However, many systems like the Yangtze Estuary (China), the Pearl Estuary (China), and the Mahakam Delta (Indonesia) consist of multiple channels. In such estuarine networks, water from different channels is exchanged at junctions or branching points. It has been shown that this distribution of the net water transport in networks not only depends on river run-off, but also on density differences and tidal amplitude, making it highly complex (Hoitink and Jay, 2016, Alebregtse and de Swart, 2016). To better understand the net water transport and its sensitivity to river discharge and tides, it is useful to disentangle the contributions by these various physical drivers.

Net water transport in estuarine networks has received considerable attention (e.g., Ridderinkhof, 1988, Wu et al., 2006, Li et al., 2010, Buschman et al., 2010, Sassi et al., 2011, Zhang et al., 2017) and several methods exist for disentangling the different contributions to it. One such approach is the factor separation method (Stein and Alpert, 1993), which makes it possible to distinguish the effects of river, tides, and their interactions on net transport from numerical model results. Using this method, Sassi et al. (2011) proposed the framework of *differential water level setup* to explain the effect of tides on net water transport: river-tide interactions alter the subtidal water level in one channel, adjusting the pressure gradient in the adjacent channels and thus leading to a reallocation of net water transport at the junction. However, the factor separation method is not suitable for disentangling more contributions to subtidal transport, such as baroclinicity and several distinct contributions generated by tides. Alternatively, Alebregtse and de Swart (2016) present a framework for disentangling the various contributions of tidal rectification on net water transport in estuarine tidal networks using perturbation expansions. They used a process-based 1D model and identified the contributions by river discharge, Stokes transport and the associated return flow, horizontal advection within channels and at junctions, and depth-dependent friction. They showed that each of these contributions is responsible for generating net water transport in channels of an estuarine network. However, because of the 1D nature of their model, subtidal flow due to e.g., vertical advection of horizontal momentum and density-driven flow is missing. The latter is considered to be one of the strongest contributors to subtidal flows in many tidal channels, for example, in the North Passage of the Yangtze Estuary (Jiang et al., 2013a).

The goal of this study is to disentangle and analyse the contributions of different drivers for the distribution of net water transport in estuarine networks including density-driven flow and vertical advection and investigate their sen-

sitivity to river discharge, tide, human interventions, and sea level rise. To this end, the idealised process-based 2DV network model in Chapter 2 is extended in two aspects. First, tidal rectifications are taken into account. Second, the effect of the along-channel density gradient is considered, as well as its impact on vertical eddy viscosity parameterisation. Furthermore, it will be shown that our method naturally extends the conceptual framework of differential water level setup of Sassi et al. (2011).

The prototype estuarine network that is considered in this study is the Yangtze Estuary, China, for which the network model from Chapter 2 has been calibrated. The model yields characteristics of tides that agree fairly well with field data. The water motion in the Yangtze Estuary is primarily forced by the river discharge from the Yangtze River and tides from the East China Sea (Figure 3.1). The Yangtze Estuary is a good example for studying the sensitivity of net water transport to variable forcing conditions, as it is an estuary network characterised by a significant seasonal river discharge variation and spring-neap modulation (Yang et al., 2015). Moreover, the geometric characteristics of the Yangtze Estuary have been changed in the past century due to both natural and anthropogenic reasons, which in turn lead to the change in the distribution of net water transport over channels. To give a deeper insight into the effect of the various interventions and changes on net water transport, two cases will be studied. Firstly, we will assess the relative impact of the Deep Waterway Project comprised of both the narrowing and deepening of the North Passage. Secondly, the effects of sea level rise on the drivers of the distribution of net water transport will be investigated. While the aim of this study is qualitative, the computed net water transport will be compared to other studies that aimed at a more precise quantitative estimate of net water transport to verify the results and add a deeper process-level understanding of these numbers.

This chapter is structured as follows. Section 3.2 presents the model geometry and outlines the derivation of equations that govern the subtidal dynamics in estuarine networks. The model is then applied to the Yangtze Estuary and the motivation for the design of experiments is outlined. The results showing the response of net water transport in the Yangtze Estuary to different changes are contained in Section 3.3. This motivates the physical mechanism that explains the generation of net water transport in the estuarine network, which is explained in the discussion (Section 3.4) and followed by the conclusions (Section 3.5).

3.2 Model and Methods

3.2.1 Model

Domain and graph representation of a network

In this study, the estuarine network is schematised as a set of connected idealised channels, which can be mathematically denoted as a directed graph $G = \{V, E\}$. The notation used here is consistent with graph theory and hence slightly deviates from the notation of, e.g., Hill and Souza (2006). An example of the Yangtze Estuary is given in Figure 3.1, where channel labelling is explained. The graph consists of a set of vertices V and edges E. The direction of each edge denotes the direction of the positive x-axis. The set of vertices V contains vertices marking river heads V_R, vertices connecting to the sea V_S and internal vertices (junctions) V_I. Similarly, the set of edges E contains river channels E_R, sea channels E_S and internal channels E_I. Each edge $e_j \in E$ is an ordered set of two vertices, marking the up- and downstream ends of the channels, so that an edge may be denoted as $e_j \equiv e_{qr} = (v_q, v_r)$ if the edge runs from v_q to v_r, with j the channel label. The Cartesian coordinates x and z are used, where x is the along-channel coordinate increasing in the direction of the river flow (seaward) and z is the vertical coordinate pointing upward, with $z = 0$ the undisturbed water level.

For each channel e_j, the length is denoted by L_j, and the depth H_j is assumed constant. Both the transverse and longitudinal bed slopes are 0 in all channels. The width is assumed depth-independent and exponential,

$$B_j(x) = B(L_j) \exp\left(\frac{x - L_j}{L_{b,j}}\right), \quad 0 \leq x \leq L_j, \forall e_j \in E. \tag{3.2.1}$$

Here, $L_{b,j}$ is the length scale at which the width of channel e_j varies exponentially. Channel indices will be omitted in the rest of this chapter for equations that hold for all channels.

Equations of motion

The water motion is governed by the width-averaged shallow water equations. These equations can be decomposed into different harmonic components, assuming that every state variable can be represented by a superposition of a truncated harmonic series. The harmonic component of a state variable, or a term, is denoted by a subscript n. The truncated harmonic series contain the subtidal frequency ($n = 0$) and the semi-diurnal frequency (i.e., M_2, $n = 1$). A

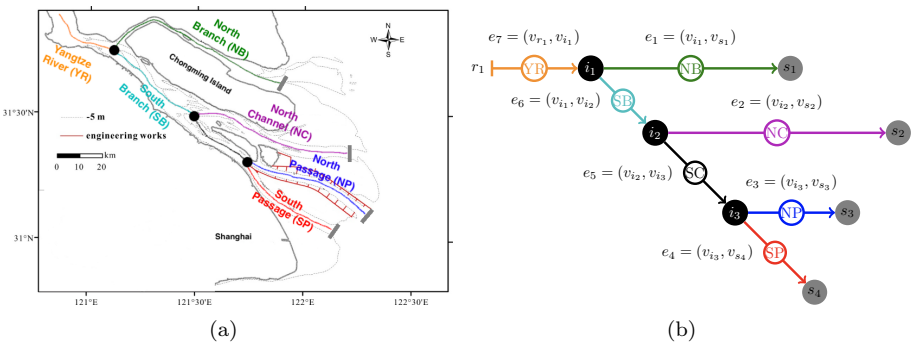

(a) (b)

Figure 3.1: a. Map of the Yangtze Estuary adapted from Jiang et al. (2013a). b. The digraph represents the channel network of the Yangtze Estuary. Solid grey circles denote open sea where tidal forcing is prescribed. The closed ends of river channels are shown in vertical bars, where the tidal current vanishes and a constant river discharge is prescribed. Each colour circle encloses the abbreviation for that channel.

detailed explanation is provided in Section S1. The resulting equations are

$$\frac{\partial u_n}{\partial t} + \left(u\frac{\partial u}{\partial x} + w\frac{\partial u}{\partial z}\right)_n = -g\frac{\partial \eta_n}{\partial x} - \left(\frac{g}{\rho_0}\int_z^\eta \frac{\partial \rho}{\partial x}\mathrm{d}z'\right)_n + \breve{A}_{vn}\frac{\partial^2 u_n}{\partial z^2}, \quad (3.2.2a)$$

$$\frac{\partial u_n}{\partial x} + \frac{\partial w_n}{\partial z} + \frac{1}{L_b}u_n = 0, \quad (3.2.2b)$$

where η is the free surface height, u is the along channel velocity, w is the vertical velocity and the gravitational acceleration $g = 9.81\,\mathrm{m\,s^{-2}}$. Note that in the advective term, the total velocity contains all frequencies, only the relevant frequencies are retained after the nonlinear interaction. For the constant vertical eddy viscosity $\breve{A}_{vn}$, the subscript n denotes the eddy viscosity acting on harmonic component n. The magnitude of eddy viscosity is different for tidal and subtidal flows, as discussed in detail in the next subsection. Water density ρ varies due to vertically well-mixed tidally-averaged salinity $s(x)$ as

$$\rho = \rho_0(1 + \beta_s s), \quad (3.2.3)$$

where the saline contraction coefficient $\beta_s = 8.3 \times 10^{-4}$ psu^{-1} and reference density of water $\rho_0 = 1000\,\mathrm{kg\,m^{-3}}$. As can be seen from the second term on the right-hand side of Eq. (3.2.2a), this density field creates a depth-dependent (so baroclinic) pressure gradient force. The longitudinal salinity profile in each channel is described by the subtidal salt mass balance in equilibrium:

$$\frac{\mathrm{d}}{\mathrm{d}x}(T_s) = 0, \quad T_s = Qs - BHK_h\frac{\mathrm{d}s}{\mathrm{d}x}. \quad (3.2.4)$$

Here, Q is the net water transport (see also Section 3.2.1), K_h is the horizontal eddy diffusivity, and T_s is the cross-sectionally averaged salt transport, which

is a constant for each channel.

The boundary conditions to Eq. (3.2.2) at the free surface $z = \eta$ are the no-stress condition and the kinematic boundary condition. The bottom $z = -H$ is assumed to be impermeable and a partial-slip condition (Engelund, 1970) is applied, i.e.,

$$\check{A}_{vn}\frac{\partial u_n}{\partial z} = 0 \qquad \text{and} \quad w_n = \frac{\partial \eta_n}{\partial t} + \left(u\frac{\partial \eta}{\partial x}\right)_n \quad \text{at} \quad z = \eta_n, \tag{3.2.5a}$$

$$\check{A}_{vn}\frac{\partial u_n}{\partial z} = \check{s}_{fn}u_n \quad \text{and} \quad w_n = 0 \qquad\qquad \text{at} \quad z = -H, \tag{3.2.5b}$$

where $\check{A}_{vn}\frac{\partial u_n}{\partial z}$ is the kinematic internal stress and $\check{s}_{fn}$ are the constant slip parameter, whose value differs for each harmonic component (see Section 3.2.1 for more details). At the seaside vertices $v \in V_S$, the water motion is forced by a prescribed sea surface elevation and a subtidal salinity is prescribed. At river head vertices $v \in V_R$, a constant river discharge is imposed and the salinity is assumed to vanish, viz.

$$\eta_{n,j} = \delta_{n1}Z_j\cos(\omega t - \phi_j) \text{ and } s_j = s_{\mathrm{sea},j} \quad \text{at } x = L_j,\ \forall e_j \in E_S, \tag{3.2.6a}$$

$$B_j\int_{-H_j}^{\eta_j} u_{n,j}\mathrm{d}z = \delta_{n0}Q_{R,j} \text{ and } s_j = 0 \qquad \text{at } x = 0,\ \ \forall e_j \in E_R, \tag{3.2.6b}$$

where ω is the angular frequency for the M_2 tide, Z_j, ϕ_j, and s_{sea} are the prescribed tidal amplitudes, phases, and salinity at the open sea, Q_R is the constant river discharge, and δ_{nk} is the Kronecker delta ($\delta_{nk} = 1$ if $n = k$ and 0 otherwise). When $n = 0$, the subtidal water level is 0 at the sea and a volume flux (river discharge) is prescribed at the river head. When $n = 1$, the water level at the sea is periodic (M_2) and the cross-sectionally integrated tidal current vanishes at the tidal limit.

At each vertex $v \in V_I$, conservation of mass is assumed for water motion. From the momentum balance, it follows a condition for the depth-averaged dynamic pressure, which is discussed in Section S5. Salinity is assumed to be continuous and salt mass transport is assumed to be conserved. These conditions read

$$g\eta_{n,j} + \frac{\mu}{2}\left(\overline{u_j^2}\right)_n = g\eta_{n,k} + \frac{\mu}{2}\left(\overline{u_k^2}\right)_n \quad \text{and} \quad s_j = s_k, \qquad \forall v_i \in V_I,\ \forall j,k \text{ such that } v_i \in e_j, e_k, \tag{3.2.7a}$$

$$\sum_{e_j \in I_i} B_j H_j \overline{u_j} = \sum_{e_j \in O_i} B_j H_j \overline{u_j} \quad \text{and} \quad \sum_{e_j \in I_i} T_{s,j} = \sum_{e_j \in O_i} T_{s,j}, \qquad \text{for sets } I_i = \{e \in E | e = (v_q, v_i)\} \text{ and } O_i = \{e \in E | e = (v_i, v_q)\}, \tag{3.2.7b}$$

where a bar $\bar{\cdot}$ denotes the average over depth, and μ is the fraction of kinetic energy dissipated at the junction (van de Kreeke, 1988). Eq. (3.2.7b), describing

mass conservation for both water and salt at junctions, differentiates between the set of channels downstream of a junction O_i and the set of channels upstream of a junction I_i. In this study, upstream and downstream are defined with respect to the negative and positive x-directions.

Turbulence model

The values of the effective eddy viscosity and slip parameter are generally different for each harmonic component (Godin, 1999). These values are computed assuming that in each channel, the total energy dissipation due to viscous effects over one tidal cycle at each frequency is the same as the energy dissipation obtained from a space- and time-dependent turbulence model. The space- and time-dependent turbulence model used here is extended compared to Chapter 2 to account for the effect of periodic density stratification on eddy viscosity (Jiang et al., 2013a):

$$A_v(x,z,t) = l^2\left|\frac{\partial u}{\partial z}\right|\left(1+\left|\frac{\partial \rho}{\partial x}\right|\frac{|\hat{u}_1|}{\omega\Delta\rho}\cos(\omega t-\alpha)\right). \tag{3.2.8}$$

Here, $\Delta\rho$ is the vertical density difference scale (fixed on input) and $\hat{u}_1$ is the complex amplitude of the M_2 velocity (computed in the model). Note that the vertical density stratification is considered here, but not in the momentum equation Eq. (3.2.2a). This is because the contribution to salinity gradient by the vertical variation in salinity is much smaller than the depth-averaged salinity (Pritchard, 1954). Additionally, α is the phase difference between the M_2 velocity and the M_2 eddy viscosity. Its value is chosen such that the M_2 eddy viscosity attains the maximum at the end of the flood. The mixing length l (Kundu et al., 2016), which contains a calibration parameter, is parameterised by a parabolic profile adapted from Chen and de Swart (2016) and is the same as that used in Chapter 2. The partial slip parameter in the space- and time-dependent turbulence closure is assumed to be linear in the local bottom velocity magnitude $|u_b|$,

$$s_f = C_{100}|u_b|, \tag{3.2.9}$$

where C_{100} is the bottom drag coefficient, the value of which depends on the bottom type and typically ranges from 0.001 to 0.006 (Soulsby, 1997).

Net water transport

Denoting the time average over one tidal cycle by $\langle\cdot\rangle$, the net water transport Q is defined to be the tidally-averaged volumetric flow rate, i.e.,

$$\begin{aligned} Q = \left\langle B(x)\int_{-H}^{\eta} u\mathrm{d}z\right\rangle &= B\left(\int_{-H}^{0}\langle u\rangle\,\mathrm{d}z + \left\langle\int_{0}^{\eta} u\mathrm{d}z\right\rangle\right) \\ &\approx B\left(\int_{-H}^{0}\langle u\rangle\,\mathrm{d}z + \langle \eta u|_{z=0}\rangle\right). \end{aligned} \tag{3.2.10}$$

On the right hand side, the first term is the transport up to the mean sea level $z = 0$. The second term is the correction to the transport due to free surface variations and follows from the first term in the power series of u about $z = 0$, provided that the free surface variation is much smaller than the mean water depth.

3.2.2 Construction of approximate solutions

Approximate solutions of the system (3.2.2)-(3.2.7) are constructed using the perturbation method (as detailed in Section S2). Equations are nondimensionalised, scaled, and written in terms of asymptotic expansions of state variables in a small parameter ε. Here, ε is the ratio of prescribed tidal elevation amplitude to the undisturbed water depth (Ianniello, 1977, 1979). Next, state variables are written in terms of an asymptotic series

$$u_n = u_n^0 + u_n^1 + \cdots, \tag{3.2.11}$$

and similar for η and w, where the superscript denotes the order of ε. Collecting terms at the same order of ε results in a system of equations at each order of ε. The leading order system and the associated solutions, featuring the M_2 tidal motion and river flow, are identical to that in Chapter 2. The first order solutions are developed below.

Focusing on the subtidal flow, the solution procedure allows for distinguishing several contributions. At the leading order, there is only the contribution by the river discharge. At the first order, we obtained linear equations for the momentum and depth-integrated continuity equations that read as

$$g\frac{\mathrm{d}\eta_0^1}{\mathrm{d}x} - \check{A}_{v0}^{\,0}\frac{\partial^2 u_0^1}{\partial z^2} = -\underbrace{\sum_n \left\langle u_n^0 \frac{\partial u_n^0}{\partial x} + w_n^0 \frac{\partial u_n^0}{\partial z} \right\rangle}_{F_{\mathrm{adv}}} + \underbrace{\frac{g}{\rho_0}\frac{\mathrm{d}\rho}{\mathrm{d}x}z}_{F_{\mathrm{baroc}}} + \underbrace{\check{A}_{v0}^{\,1}\frac{\partial^2 u_0^0}{\partial z^2}}_{F_{\mathrm{rivc}}}, \tag{3.2.12a}$$

$$B(x)\left(\int_{-H}^{0} u^1 \mathrm{d}z + \underbrace{\sum_n \left\langle \eta_n^0 u_n^0|_{z=0} \right\rangle}_{F_{\mathrm{Stokes}}}\right) = Q^1, \tag{3.2.12b}$$

where Q^1 is the first order contribution to the subtidal transport. It turns out that the eddy viscosity and slip parameter acting on the first order flow are the same as those acting on the leading order flow. All terms denoted by underbraces only involve known quantities from the leading-order solution. Detailed physical interpretations of these terms are provided in Section 3.2.3. These equations are linear in the first-order unknowns u_0^1 and η_0^1. Therefore, the superposition principle can be applied to decompose the subtidal system:

the solutions are constructed by adding contributions of different forcing mechanisms (Ianniello, 1977). The forcing terms are indicated by an underbrace: F_{adv} is the momentum advection by the leading-order flow, F_{Stokes} is the Stokes transport, F_{rivc} is a first order correction to the river flow and F_{baroc} is the baroclinic forcing. The boundary conditions at the mean sea surface and bottom respectively read

$$\check{A}_{v0}{}^{0}\frac{\partial u_0^1}{\partial z} = -\underbrace{\sum_n \left\langle \eta_n^0 \frac{\partial^2 u_n^0}{\partial z^2} \right\rangle}_{F_{\text{vda}}} \qquad \text{at} \quad z = 0, \tag{3.2.13a}$$

$$\check{A}_{v0}{}^{0}\frac{\partial u_0^1}{\partial z} - \check{s}_{f0}^0 u_0^1 = 0 \qquad \text{at} \quad z = -H, \tag{3.2.13b}$$

At the free surface, the additional term $\left\langle \eta_n^0 \frac{\partial^2 u_n^0}{\partial z^2} \right\rangle$ is the result of Taylor expansion of the no-stress condition about $z = 0$. It is interpreted as the velocity-depth asymmetry (F_{vda}, see Section 3.2.3). The first-order horizontal boundary conditions describe no additional tidal forcing at the seaward boundary and no additional river discharge at the landward boundary. Furthermore, we require the continuity of momentum and mass, i.e.,

$$\eta_{0,j}^1 = 0 \qquad \text{at } x = L_j, \forall e_j \in E_S, \tag{3.2.14a}$$

$$B_j \int_{-H_j}^{0} u_{0,j}^1 \mathrm{d}z = 0 \qquad \text{at } x = 0, \quad \forall e_j \in E_R, \tag{3.2.14b}$$

$$g\eta_{0,j}^1 + \underbrace{\frac{\mu}{2}\sum_n \left\langle \overline{(u_{n,j}^0)^2} \right\rangle}_{F_{\text{dp}}} = g\eta_{0,k}^1 + \underbrace{\frac{\mu}{2}\sum_n \left\langle \overline{(u_{n,k}^0)^2} \right\rangle}_{F_{\text{dp}}}, \text{ at vertices,} \quad \text{i.e., } \forall v_i \in V_I, \forall j,k \text{ s.t. } v_i \in e_j, e_k, \tag{3.2.14c}$$

$$\sum_{e_j \in I_i} Q_{0,j}^1 = \sum_{e_j \in O_i} Q_{0,j}^1, \qquad \text{at vertices, i.e., for sets} \quad I_i = \{e \in E | e = (v_q, v_i)\} \quad \text{and} \quad O_i = \{e \in E | e = (v_i, v_q)\}. \tag{3.2.14d}$$

Here, F_{dp} is the forcing that creates first order subtidal flow in each channel such that the leading order momentum transfer is continuous, i.e., continuous dynamic pressure. In order to determine the eddy viscosity and slip parameter, a perturbation method is also applied to the space- and time-dependent turbulence closure (see Section S3 for details).

Eq. (3.2.12)-(3.2.14) are linear inhomogeneous equations for each forcing term F, which can be solved independently. Therefore, the first order velocity can be written as,

$$u^1 = u^1_{\text{baroc}} + u^1_{\text{adv}} + u^1_{\text{Stokes}} + u^1_{\text{vda}} + u^1_{\text{dp}} + u^1_{\text{rivc}}. \tag{3.2.15}$$

Analytical solutions for the first order velocities are presented in Section S4.2. Detailed derivation and solution procedures for a single channel can be found in the user manual of iFlow (SI of Dijkstra et al., 2017a).

3.2.3 Forcing mechanisms of different drivers for net water transport

It turns out that each of the forcing terms identified in Eq. (3.2.12)-(3.2.14) contributes to the net water transport, additional to the river flow at the leading order. Due to the linearity of the ordered equations, the net water transport can be written as

$$Q = Q_{\mathrm{river}} + Q_{\mathrm{baroc}} + Q_{\mathrm{adv}} + Q_{\mathrm{Stokes}} + Q_{\mathrm{vda}} + Q_{\mathrm{dp}} + Q_{\mathrm{rivc}}. \tag{3.2.16}$$

Each term in Eq. (3.2.16) is the result of one type of subtidal forcing mechanisms, which will be described with a focus on the contribution by tides in this subsection. Note that the net water transport in a single channel in equilibrium is the same as the imposed river discharge and other residual flows have zero contribution due to mass conservation (Ianniello, 1979, Cheng et al., 2010). In a network, however, any type of subtidal flow may contribute to the net water transport and mass conservation is still fulfilled (Sassi et al., 2011, Alebregtse and de Swart, 2016). For example, a single channel with imposed river discharge cannot import water from the sea. In contrast, a sea channel in a network may import water from the sea because this amount of water can be exported back to the sea through other sea channels. It will be demonstrated in Section 3.4.1 how each of these forcing mechanisms contributes to the net water transport. Note that the rectification processes (horizontal advection, Stokes transport and its return flow, velocity-depth asymmetry, and dynamic pressure) are forced by both leading order river and tidal flow, but the forcing by the tidal flow is dominant, on which the below interpretations are based.

River ($F_{\mathbf{river}}$) The leading order approximation to the externally prescribed river discharge.

Baroclinicity ($F_{\mathbf{baroc}}$) The consequence of the salinity gradient, resulting in a density-driven flow.

Advection ($F_{\mathbf{adv}}$) Advection of the along-channel momentum, by both horizontal and vertical currents.

Stokes transport ($F_{\mathbf{Stokes}}$) Tidal flow is periodic and after each tidal cycle, there will be a net displacement of water particles in the direction of tidal wave propagation (Stokes drift). To satisfy mass conservation, this is compensated by a return flow that transports water in the opposite direction, which is forced by the Stokes transport. The sum of Stokes transport and the transport due to its return flow is a constant in each channel in a network.

Velocity-depth asymmetry ($F_{\mathbf{vda}}$) It is due to the correlation between free surface height and flow curvature at the free surface, which varies over one

Channel	Label	L (km)	L_b (km)	H (m)	B_o (km)
North Branch (NB)	1	85	30	5	12
North Channel (NC)	2	60	52	7	20
North Passage (NP)	3	61	470	11	3.5
South Passage (SP)	4	54	21	7	30
South Channel (SC)	5	23	-368	9	6.2
South Branch (SB)	6	51	64	9	14
Yangtze River 1 (YR1)	7	50	206	10	6.6
Yangtze River 2 (YR2)	8	50	206	10	5.2
Yangtze River 3 (YR3)	9	50	206	10	4.1
Yangtze River 4 (YR4)	10	50	206	10	3.2
Yangtze River 5 (YR5)	11	370	1660	10	2.5

Channel	Elevation amplitude (m)	Elevation phase (rad)
NB	1.5	-0.53π
NC	1.06	-0.58π
NP	1.3	-0.58π
SP	1.3	-0.53π
Angular frequency ω	1.4×10^{-4} (s^{-1})	

Table 3.1: Geometry and M_2 tidal forcing of the reference Yangtze Estuary network, including the channel length L, the length scale L_b at which channel width increases exponentially in the seaward direction, the water depth H and the width at the seaward boundary B_o.

tidal cycle and so does the vertical profile of the velocity. The velocity at each depth is therefore not symmetric over one tidal cycle. It hence acts as depth-dependent friction on depth-averaged flow.

Continuous dynamic pressure ($F_{\mathbf{dp}}$) This contribution amounts to tidal rectification due to advection at junctions. It is the consequence of momentum conservation at junctions (see Section S5 for more details).

A correction to river flow ($F_{\mathbf{rivc}}$) The friction parameters for the river flow are calculated assuming that they are only affected by the river and tidal flows. The influence of other subtidal flows on the friction parameters for the river flow is accounted for by this contribution. Physically, it is a correction to the river flow that parametrically accounts for the effect of periodic density stratification on vertical mixing.

3.2.4 Design of experiments and parameter values

The reference case for this study is the Yangtze Estuary in the dry season (January 2014), to which the model has been calibrated to yield characteristics of both river and tides that agree fairly well with field data in Chapter 2. Analysis of the turbulence model shows that (as detailed in Section S3), the additional

Section	Description	Changes
3.3.1	Reference	Dry season $Q_R = 1 \times 10^4\,\mathrm{m^3\,s^{-1}}$, monthly-averaged tidal forcing (Table 3.1)
3.3.2	Wet season	Increase river discharge up to $4 \times 10^4\,\mathrm{m^3\,s^{-1}}$ (Alebregtse and de Swart, 2016)
3.3.3	Spring-neap	Vary tidal amplitudes from 50% to 150% of the default case (Lu et al., 2015)
3.3.4	Before DWP	$H = 7$ m, $b_o = 3.5$ km and $L_b = 60$ km in the NP (Jiang et al., 2012)
3.3.5	Sea level rise	Increase undisturbed water depth up to 2 m (Kuang et al., 2017)

Table 3.2: List of experiments

term in Eq. (3.2.8) that accounts for the density stratification in vertical eddy viscosity only has an influence on the subtidal dynamics and hence new calibration is not required. The typical density difference $\Delta\rho$ between the bottom and the surface is about $7\,\mathrm{kg\,m^{-3}}$ (Jiang et al., 2013a). Table 3.1 contains the geometric characteristics of each channel. Water motion is forced from both the seaward and landward boundaries. At the sea, a constant river discharge $Q_R = 10^4\,\mathrm{m^3\,s^{-1}}$ is imposed and the monthly-averaged semi-diurnal lunar tide (M_2) is prescribed at the sea (Table 3.1). The effects of seasonal variation in river discharge, spring-neap modulation, channel deepening/narrowing, and sea level rise on the distribution of net water transport over different channels will be investigated by varying the prescribed discharge, tidal amplitudes, local channel depth/convergence, and water depth in all channels so that the sensitivity of water transport distributions to these changes can be investigated. The list of experiments is provided in Table 3.2. Head loss is not accounted for in this study and hence $\mu = 1$, meaning that there is no kinetic energy dissipation at junctions. The bottom drag coefficient C_{100} is 0.0022. The horizontal diffusion coefficient $K_h = 250\,\mathrm{m^2\,s^{-1}}$ is used for all cases in the salt model. It will be shown and explained in Section 3A that the results for the net water transport are insensitive to K_h.

The spring-neap variation is caused by the combination of M_2 and S_2 (semi-diurnal solar) tides, which may be seen as a slow (i.e., 14 days) modulation of the semi-diurnal tide. While the term M_2 tide is used in this study, it represents all components with the semi-diurnal (or D_2) period. For this reason, different phases of the spring-neap cycle are represented by varying the prescribed M_2 amplitudes at the sea. From neap to spring, the prescribed monthly averaged tidal amplitudes are multiplied by 0.5 to 1.5, as practical approximations, according to the observations by Lu et al. (2015).

Geometric characteristics in the North Passage (NP) were changed by the Deep Waterway Project (DWP) in two aspects: channel dredging that deep-

ened the channel from 7 m to 11 m and the construction of training walls, which increased the convergence length from 60 km to 470 km, with the width at the junction unchanged. Their combined effect on net water transport will be first investigated, followed by their individual effects.

Sea level rise (SLR) increases the mean water depth and thereby tidal amplitudes. The effects of changing tidal amplitudes have been investigated separately and therefore the SLR will be represented by increasing water depth. A reasonable upper bound for global SLR by 2100 would be 2 m (Nicholls et al., 2011), which was also used by Kuang et al. (2017) for the Yangtze Estuary. So the same upper bound for SLR will be used in this study.

To analyse the results, the distribution of the net water transport over the different channels will be quantified by the net water diversion ratio (nWDR) (Li et al., 2010). At one junction, it is the ratio of the net water transport in one downstream channel over the sum of net water transports in all downstream channels. In this study, there are at most two downstream channels connected by a junction and hence the nWDR reads

$$\text{nWDR} = \frac{Q_j}{Q_j + Q_k}, \quad \text{for} \quad e_j, e_k \in O_i, \tag{3.2.17}$$

where O_i is the set of all downstream channels of a branching point $v_i \in V_I$. The nWDRs of the North Branch, the North Channel, and the North Passage are sufficient for describing the distribution of net water transport in the Yangtze Estuary, because the values for the other branching channels can be obtained by subtracting the nWDRs of these three channels from unity. In addition, using Eq. (3.2.16), the nWDR can be further decomposed into different components according to the associated physical drivers.

3.3 Results

3.3.1 Reference case

The modelled net water transport for the reference case in all channels of the Yangtze Estuary is presented in Fig. 3.2. Coloured boxes in each bar represent the subtidal transport components in one channel. The colours indicate the contributions of the individual processes and the black line shows the sum of all contributions. Positive numbers indicate net downstream transport. The leading order river flow contributes the most to the net water transport in each branch, except for the North Branch (NB), which is the shallowest and the narrowest channel.

The directions of each component of the net water transport in all channels are identical to those found by Alebregtse and de Swart (2016), except for the transport due to baroclinic forcing (baroc) and the first order correction to river flow (rivc), which are not considered in their model. However, the magnitude of

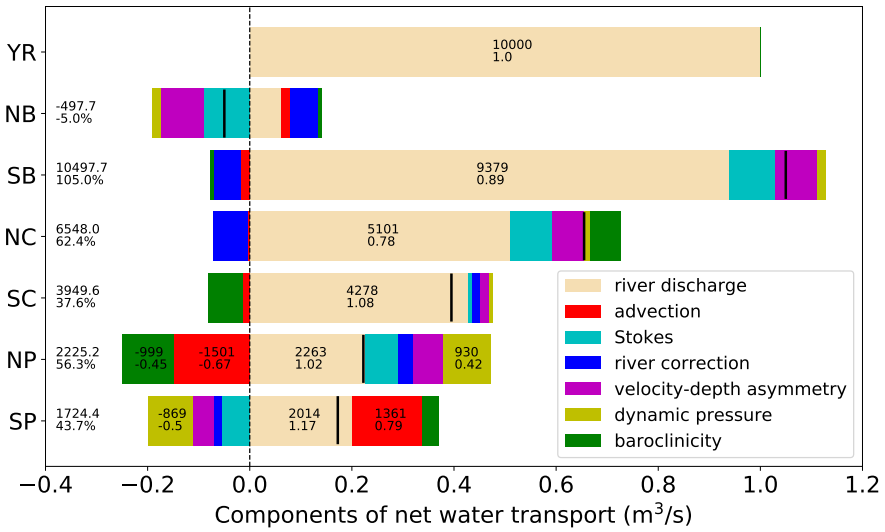

Figure 3.2: Net water transport in the Yangtze Estuary for the reference case. Values on the left of each bar are the net water transport (upper, $m^3\,s^{-1}$) and the net water diversion ratio (lower). Values within each box are the water transport of the component (upper) and the fraction of the component in the net water transport. Values are hidden for fractions less than 20% and for the NB. In each channel, the magnitude of the net water transport (the upper number on the left) is also indicated by a black vertical line.

each transport component is different. The net water transport due to velocity-depth asymmetry (vda) and Stokes and its associated return flow (Stokes) is larger compared to Alebregtse and de Swart (2016), which implies that a 1D model may underestimate the transport related to flow vertical structure.

The superposition of the various contributions leads to the negative net water transport in the NB. This has also been observed (Wu et al., 2006, Li et al., 2010, Zhang et al., 2017). Wu et al. (2006) concluded that the negative transport is the consequence of the funnel-shaped bottom of the NB and the river-tide interaction, locally near the junction. However, in our model, the geometric characteristics are extremely simplified and small scale dynamics near the junctions is not resolved. The recreation of landward net water transport in the NB with this model therefore suggests that it is the consequence of hydrodynamical processes over a much larger spatial scale and hence a robust feature. We further add that this is mainly due to two kinds of tidal rectification processes: Stokes and its return flow and velocity-depth asymmetry. This is because the NB is the shallowest channel with the largest tidal range, causing both the total depth ($H + \eta$) and velocity highly asymmetric between high water and low water. The numerical results of Zhang et al. (2017) showed that, during the dry season, the averaged net water transport in the NB excluding the river water transport is about $-1500\,\mathrm{m^3\,s^{-1}}$, which is comparable to our model results, about $-1200\,\mathrm{m^3\,s^{-1}}$. Using the factor separation method (Stein and Alpert, 1993), they decomposed the flow discharge into three components: river, tide and river-tide interaction. The transport due to the tide was subsequently decomposed into Stokes transport, return flow transport and a residual term. They showed that the Stokes transport and the return flow transport should be the processes that are most responsible for the negative net water transport in the NB. It is important to realise that the factor separation method is intrinsically different from the decomposition presented in this study. The transport by Stokes return flow in Zhang et al. (2017) contains all the transport components due to tidal rectification in this study. Hence, their finding also supports the results of the present study.

3.3.2 Wet season

River water transport in each channel increases linearly with the river discharge from the Yangtze River (YR) and therefore the river water diversion ratio, the diversion ratio when river water transport is the only contribution to net water transport, is unaffected by the prescribed discharge (see Chapter 2). All other contributions to the net water transport are not sensitive to the river discharge (not shown). First, this is because the tidal rectification terms are mostly driven by the leading order tide, and tide-river interaction is minor in the downstream part of the estuary. Second, even though the salt intrusion limits move seaward for increasing river discharge, the net transport due to baroclinic pressure is insensitive to river discharge because the salt intrusion limits do not move

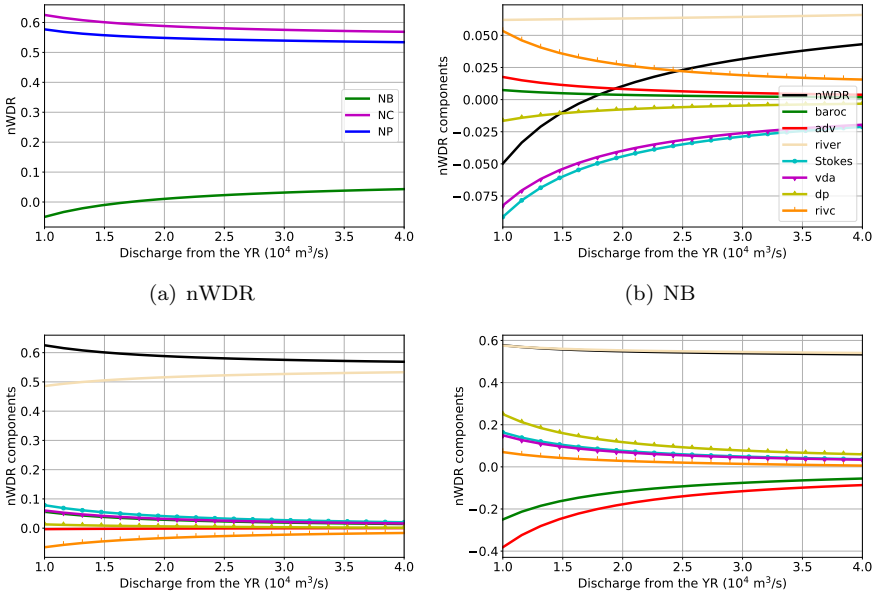

(a) nWDR (b) NB

(c) NC (d) NP

Figure 3.3: Sensitivity of net water diversion ratio (nWDR) and its component to river discharge from the Yangtze River (YR). a. nWDR in the NB, the NC, and the NP versus discharge from the Yangtze River. b. Contribution of each subtidal flow to the nWDR of the NB (branching point i_1). The black curve is the nWDR of the NB as in a. c. As b, but for the NC (branching point i_2). d. As a, but for the NP (branching point i_3).

across the junctions. This is explained in Section 3A. Third, the correction to river flow is forced by river discharge. This contribution is therefore the most sensitive to river discharge among insensitive first order contributions.

The sensitivity of the net water diversion ratio (nWDR) to the discharge from the YR at three junctions is contained in Fig. 3.3(a). At every junction, results are shown for one of the two downstream channels, as the value of nWDR for the other channel can be obtained by subtracting the value in this figure from unity. The nWDR for the North Branch (NB) changes sign from negative to positive when the prescribed discharge is about $1.7 \times 10^4\,\mathrm{m^3\,s^{-1}}$, meaning that the net water transport in the NB changes direction from landward to seaward. This is because, for increasing river discharge, all subtidal transport components change very little, except the river discharge itself, which is directed seaward. It can also be seen that a larger river discharge leads to a more even distribution of the nWDR, which confirms the finding of Li et al. (2010). Specifically, for increasing river discharge, the nWDR converges to the

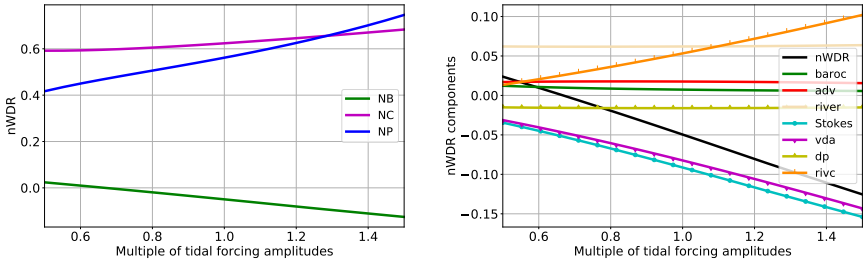

(a) nWDR

(b) NB

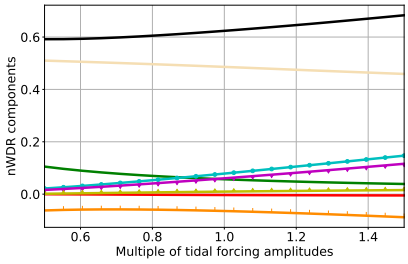

(c) NC

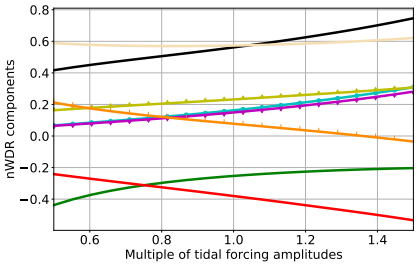

(d) NP

Figure 3.4: As Fig. 3.3, but for the sensitivity of net water diversion ratio (nWDR) to multiple tidal forcing amplitudes at the sea.

diversion ratio of river discharge. The reason for this is, again, other transport components are not sensitive to increasing river discharge. This is further illustrated in panels (b), (c), and (d), which show the components of nWDR at the NB, the NC, and the NP, respectively. Black curves are the nWDR as in panel (a). Other curves represent the fractions of the associated net water transport component, and they add up to the black curve in each panel. Increasing discharge, the relative contributions of the first order components decrease and the nWDR (black line) converges to the river contribution (beige line).

3.3.3 Spring-neap tide

The river water transport is not sensitive to the prescribed tidal amplitude (see Chapter 2). For the baroclinic contribution to the net transport, it will be argued in Section 3A that the net water transport is insensitive to changes in our model configuration of the Yangtze Estuary, so K_h is kept constant. Still, the baroclinic contribution to the net water transport decreases under larger tidal forcing amplitudes, because larger tidal amplitudes cause larger vertical eddy viscosity, which reduces the gravitational circulation induced by the horizontal density gradient. Naturally, the components that are forced by the tides (ad-

vection, Stokes, velocity-depth asymmetry, and dynamic pressure) are sensitive to the tidal amplitude and their magnitudes increase almost linearly for larger tidal amplitudes. The first order correction to river water transport is also sensitive to the tidal amplitude, as tides affect the generation of turbulence. Its magnitude decreases in the North Passage, the South Passage, and the South Channel, while transport increases in the other channels.

From neap to spring tide, the net water diversion ratio (nWDR) for the North Passage (NP) is almost doubled (Fig. 3.4a). This is the result of the cumulative change in all first order contributions to the subtidal transport (panel d). For increasing tidal amplitudes, the decrease in Q_{rivc} in the NP is similar to that in the South Branch (SB, not shown). This suggests that the changes in Q_{rivc} in the South Passage (SP) and the North Channel (NC) compensate each other, that is, a redistribution of river water. Therefore, for larger tidal forcing at subtidal timescale, less river water is exported from the NP and this amount of water is exported through the North Branch (NB). The net transport direction in the NB changes sign from neap to spring tide, which again confirms that the landward transport in the NB during the dry season is mostly due to tidal rectification processes and hence is weak or absent during neap. The nWDR of the NC is less sensitive (panel c).

3.3.4 Deep Waterway Project (DWP)

The combined effects of deepening and narrowing on net water transport are shown in Fig. 3.5. This Figure is similar to Fig. 3.2 but shows the difference in net water transport compared to the case before the DWP. The total difference in the net water transport is attached to the left of each bar and indicated by a black vertical line.

The effect of the construction of the DWP was local, as the net water transports in the North Branch and the South Branch were hardly affected. The DWP increased the net water transport in the North Passage (NP). This was caused by several different mechanisms. First, river water transport was redistributed over channels due to the geometric changes caused by the DWP. After the DWP, less river water was transported into the North Channel (NC) and the South Passage (SP). They were discharged into the sea through the NP. Second, the subtidal transport due to continuous dynamic pressure changed in the same way as the river discharge and the magnitude was also comparable. However, the contribution of the redistribution by river discharge and dynamic pressure was small compared to those arising from two tidal rectification processes, Stokes and velocity-depth asymmetry. Both the two tidal rectification processes contributed to the change in the subtidal transport in the same way as the river discharge, while the magnitude of each of them was more than twice as large as that of the river flow. This pattern was largely compensated by the transport due to momentum advection and density-driven flow.

The effects of only deepening and only narrowing of the NP on net water

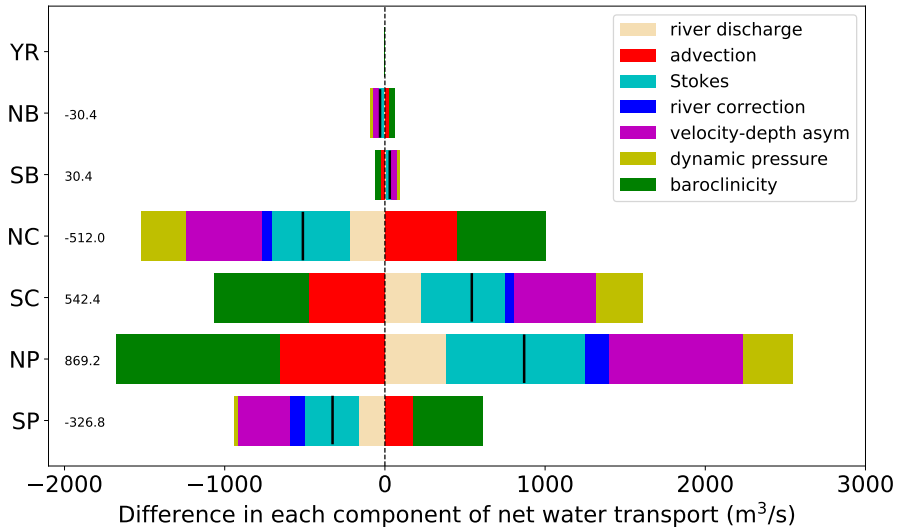

Figure 3.5: Effect of the DWP on each component of the net water transport. Each box represents the difference in the corresponding subtidal transport component between after and before the construction of the DWP. The value on the left of each bar is the sum of all boxes in the bar, i.e., the difference in the net water transport ($m^3\,s^{-1}$). In each channel, the change in the net water transport is also indicated by a black vertical line.

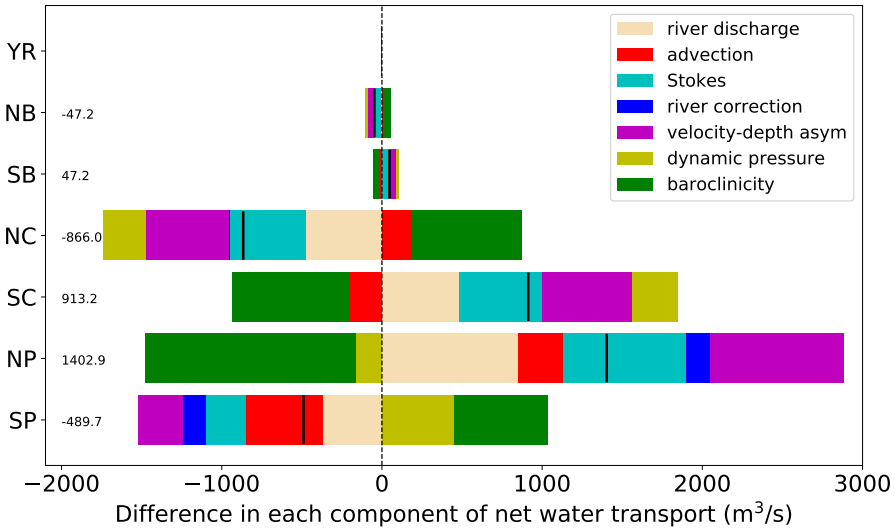

(a) Deepening

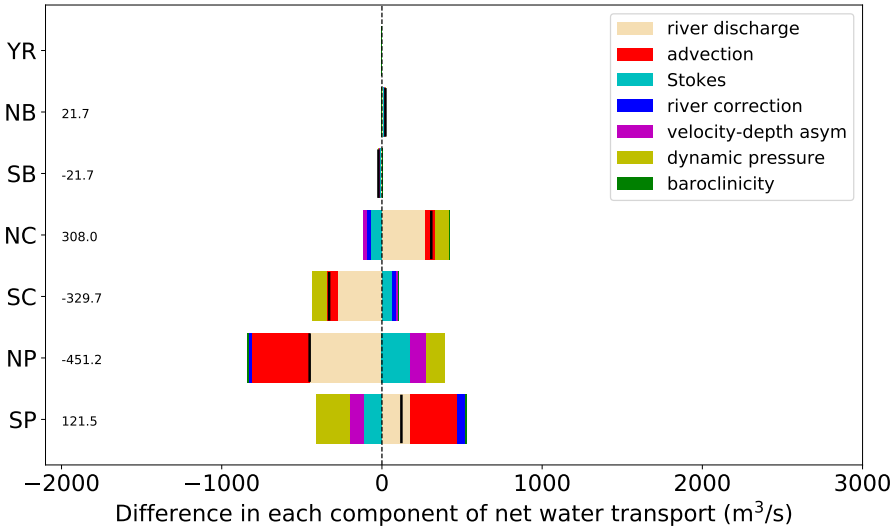

(b) Narrowing

Figure 3.6: As Fig. 3.5, but for the difference in subtidal transport components between after and before only dredging (a) and only narrowing (b) in the NP.

transport are contained in Fig. 3.6a and b respectively. Overall, the effect of narrowing on net water transport was much less strong but opposite to the effect of dredging. This is because deepening and narrowing had opposite effects on the channel cross-section area. For larger water depth in the NP (panel a), the density-driven flow was stronger in the NP and thereby induced more landward transport. It can be seen that the changes in the transport due to Stokes and velocity-depth asymmetry, the two most significant tidal rectification processes that both increased the transport in the NP, were due to the deepening. The reason for the same response of the transport due to Stokes and velocity-depth asymmetry to deepening and narrowing can be understood with the transport mechanism provided in Section 3.4.1. On the other hand, the effect of narrowing in the NP (panel b) was less significant. The effect of the narrowing was the same as described in Chapter 2: the net water transport in the NP was decreased and redirected to the South Passage (SP) and the North Channel through the South Channel, because the amount of net water transport reduced in the NP (with respect to before the narrowing) has to be discharged into the sea to fulfil mass conservation. This is due to the change in river discharge, as other transport contributions almost cancel with each other. It should be noted that the sum of Fig. 3.6a and b is qualitatively but not quantitatively the same as Fig. 3.5. This is because narrowing has a different quantitative effect on a channel of 7 m depth, which is shown here, and 11 m depth. For this reason, the magnitude reduction in the transport due to advection in Fig 3.6b is smaller than that in Fig. 3.5. This implies that the effect of narrowing on subtidal transport is larger for a deeper channel.

3.3.5 Sea level rise

Each subtidal transport component is sensitive to SLR (Fig. 3.7). For each channel, subtidal transport induced by the density-driven flow is larger in magnitude after sea level rise, because the density-driven flow scales with depth. SLR enhances the transport due to advection in the North Passage, the South Passage, and the North Branch, while greatly cancelled by the transport induced by the dynamic pressure. Qualitatively, the effect of SLR on the subtidal transport due to Stokes and velocity-depth asymmetry is the same for all channels.

The net effect of sea level rise (SLR) on the net water diversion ratio (nWDR) is, however, not too sensitive (Fig. 3.8a). This is mainly due to the effect of SLR on different transport components cancelling each other, such as the cancellation between advection and dynamic pressure in the North Branch (panel b). In the North Passage (NP, panel d), the sum of density-driven flow and advection together is cancelled by the sum of dynamic pressure and first order river flow, resulting in the curve for nWDR being almost parallel to the curve for Stokes and velocity-depth asymmetry. Although each transport component in the North Channel (NC) is sensitive to SLR, their contributions to

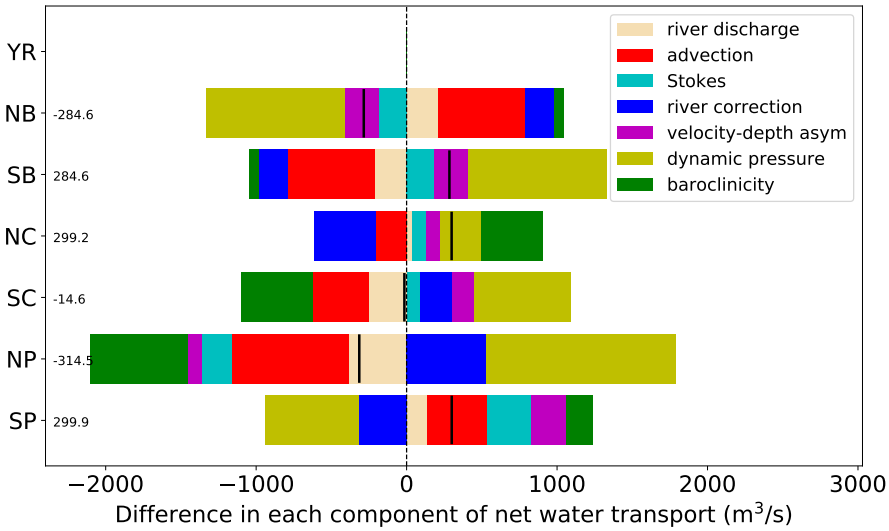

Figure 3.7: As Fig. 3.5, but for the difference of subtidal transport components between after and before 2 m sea level rise.

the nWDR are not sensitive (panel c) because their magnitudes are not comparable to the net water transport in the NC. This conclusion is specific to the Yangtze and the effect of SLR on nWDR in other networks could be different, depending on the relative importance of the various mechanisms.

3.4 Discussion

3.4.1 Net water transport mechanism in networks

The decomposition of net water transport discussed in this study yields a natural extension of the theory of differential water level setup of Sassi et al. (2011) that explains the effect of tides on net water transport. They found that tides affect the subtidal water level in channels and thereby modify the subtidal pressure gradient at junctions. This reallocates the river discharge at junctions from channels with a relatively high setup to channels with a lower setup until the setup is equal. This conclusion was drawn from considering the difference between the subtidal water level with and without tides. It therefore describes the net effect of tides, which contains all the forcing mechanisms that are related to tides in this study. Here, it will be shown that this theory can be generalised to explain the creation of net water transport by arbitrary subtidal forcing, which also contains the net effect of tides, in estuarine networks.

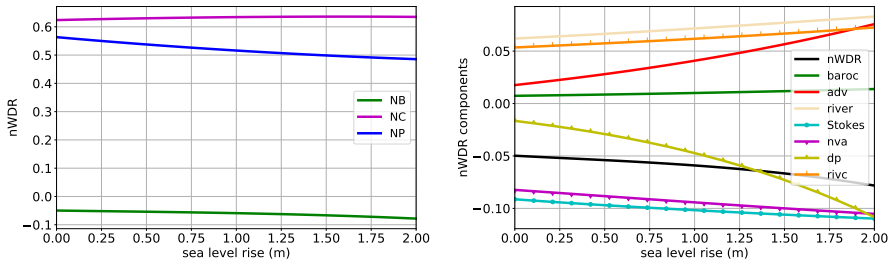

(a) nWDR

(b) NB

(c) NC

(d) NP

Figure 3.8: As Fig. 3.3, but for the sensitivity of net water diversion ratio (nWDR) to sea level rise.

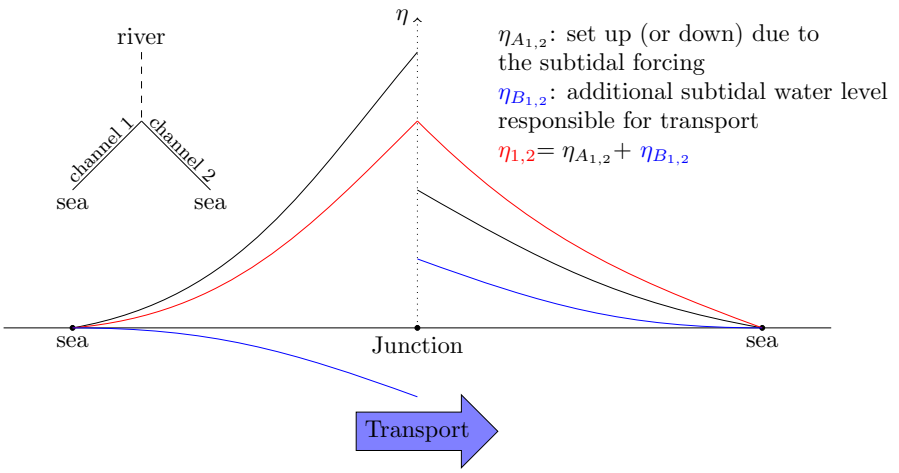

Figure 3.9: A conceptual figure shows the subtidal transport mechanism in a network of three channels. The two sea channels are labelled by 1 and 2. Black curves are the subtidal water level (subscript A) as the response to the subtidal forcing. Blue curves are the subtidal water level (subscript B) due to the subtidal transport, forced by the pressure difference at the junction created by the black curves. The total subtidal water level (red) is continuous. Note that the subtidal water level is the same as the mean sea level at the sea.

Any type of subtidal forcing within a channel will be reflected in the subtidal momentum balance through two terms: the barotropic pressure gradient due to surface elevation and the internal friction (Eq. (3.2.12a)). Here, we focus on the first: the pressure gradient. Now consider a three-channel system with one river channel and two sea channels, as depicted in Fig. 3.9. As a consequence of mass conservation, the net transport in the river channel is always the same as the imposed river discharge. This means that for any subtidal forcing, net transport can only be generated in the two sea channels. The subtidal forcing in each channel directly leads to a barotropic pressure gradient and thereby subtidal water level setup (or set-down), as illustrated by the black curves in Fig. 3.9. At the junction, this setup/set-down from both channels is, in general, discontinuous. To compensate for this discontinuity in pressure gradient at the junction, there must exist additional subtidal transport. This causes a setup in the receiving channel and a set-down in the other channel (blue curves) such that the total subtidal water level (red curves) is continuous at the junction. Hence, the theory of differential water level setup can actually be applied to each of the contributions identified in this study.

This mechanism can be also seen from the analytical solutions to all subtidal flows (see Section S4.2). For example, taking the limit of no-slip condition, the barotropic pressure gradient in the solution to the density-driven flow depends

on the unknown water transport Q_{baroc}:

$$\frac{\mathrm{d}}{\mathrm{d}x}\eta_{\mathrm{baroc}} = -\frac{3\check{A}_{v0}^{\ 0}}{gH^2}\left(\frac{2gH^3\beta_s}{\check{A}_{v0}^{\ 0}}\frac{\mathrm{d}s}{\mathrm{d}x} + \frac{Q_{\mathrm{baroc}}}{B(x)H}\right). \tag{3.4.1}$$

By integrating along the channel, on the right-hand side, the first term yields the subtidal water level of density-driven flow (black curves in Fig. 3.9) induced by the subtidal forcing (salinity gradient induced baroclinic pressure gradient force), the second term gives the subtidal water level responsible for the transport (blue curves in Fig. 3.9), and there is an unknown integration constant that needs to be determined together with the unknown transport Q_{baroc} using the channel matching and boundary conditions (Eq. 3.2.14) such that mass is conserved and subtidal water level is continuous at junctions. The solution to the density-driven flow in channels of a network is

$$u_{\mathrm{baroc}} = \frac{gH^3\beta_s}{48\check{A}_{v0}^{\ 0}}\left(1 - 9\left(\frac{z}{H}\right)^2 - 8\left(\frac{z}{H}\right)^3\right)\frac{\mathrm{d}s}{\mathrm{d}x} + \frac{Q_{\mathrm{baroc}}}{B(x)H}\left(\frac{3}{2} - \frac{3}{2}\left(\frac{z}{H}\right)^2\right), \tag{3.4.2}$$

which contains two parts. The first term is the classical solution to the density-driven flow in a single channel (Hansen and Rattray, 1965). It is zero after averaging over depth and hence does not contribute to transport. The second term, which shares the same structure as the river flow (Ianniello, 1977), has the depth-averaged value of transport per unit cross-sectional area and therefore is responsible for the transport. The special case is the subtidal contribution by continuous dynamic pressure at junctions: it is essentially forced by the difference in the momentum advection at junctions (see Section S5 for details) and hence not an internal forcing spread over an entire channel. Similar to the river discharge, it is an external forcing for every channel (the black curve is null), but the transport is distributed such that the leading order momentum is conserved at junctions.

Note that every contribution to the net water transport is created at the global scale: the transport created by each driver is determined by the associated setup (or set-down) over all channels. Therefore, it is not the local properties at junctions that are important, but the flow in all the channels throughout the estuarine network.

3.4.2 Generalisation and limitations

The method used in this study is generic and therefore some results can be generalised. First, in any estuarine network where the river-tide interaction is relatively weak, the sensitivity of net water transport to river discharge reflects that of the river discharge contribution only, as other contributions to the net transport are mostly generated by tides. Second, in such estuaries larger tidal amplitudes will typically reduce the transport created by the gravitational circulation. Moreover, the magnitude of each contribution to net water transport

due to tides is expected to be positively correlated to the tidal amplitudes. Their net effect is hence the consequence of the balance of all these contributions in different channels. Hence, this is strongly dependent on the estuary under consideration. In general, such a network needs to be analysed globally rather than focusing on one or some of the channels, or on local dynamics near a junction.

The idealised nature of the model imposes some limitations, some of which are discussed in Chapter 2. These include, for example, instantaneous adjustment of the system to time-varying forcing (Geyer and MacCready, 2014) and the simplified geometry that does not explicitly resolve lateral process (Scully et al., 2009) and tidal flats (Hepkema et al., 2018). Also, the effect of changing vertical density stratification is not dynamically resolved. The baroclinic pressure assumes negligible vertical stratification and the eddy viscosity assumes a small prescribed vertical tidal density gradient, that may no longer be representative if the estuary becomes more strongly stratified. This may, for example, occur around the neap tide, under large channel deepening or sea level rise. Nonetheless, the model result is not sensitive to the vertical density difference (see Fig. S1. A more complex description of density-dependent and time-dependent eddy viscosity, as well as internally generated overtides, may be added to this framework to enhance complexity and realism, which is beyond the scope of this study.

3.5 Conclusions

Using a process-based model, the net water transport in channels of estuarine networks is disentangled and attributed to various physical processes and drivers: the river discharge, vertically well-mixed salinity induced along-channel density gradient, Stokes transport and its return flow, advection of horizontal momentum, velocity-depth asymmetry, and continuous dynamic pressure at junctions. The mechanism for the distribution of net water transport of each physical driver is explained by generalising the conceptual framework of differential water level set-up.

The model is subsequently applied to the Yangtze Estuary, a typical estuarine network, to investigate the sensitivity of the distribution of net water transport over its channels to river discharge, spring-neap modulation, local deepening and narrowing and sea level rise. Besides the river water transport itself, net water transport due to other physical drivers are quantitatively insensitive to prescribed river discharge; drivers related to tide only change slightly due to weak tide-river interaction and the baroclinic transport is weakly dependent on salt intrusion. Hence, for increasing river discharge, the distribution of net water transport converges to the river water distribution. Conversely, the river discharge distribution is less sensitive to the transport driven by the tide and density gradients. Notably, assuming a stationary spring/neap state

(instantaneous hydrodynamic adjustment), by varying the tidal forcing from neap to spring tide, the direction of net water transport in the North Branch changes from seaward to landward because of tidal rectification processes. It was found that the deepening and narrowing of a channel have opposite effects on net water transport. The effect of the Deep Waterway Project in the Yangtze Estuary was dominated by the deepening, leading to increased net water transport in the North Passage. Each identified driver is sensitive to sea level rise. However, in the model configuration of the Yangtze Estuary, the cancelling of components against each other causes the net water transport in each channel of the Yangtze to be not so sensitive to sea level rise up to 2 m, with a maximum decrease in the North Passage of about 20%.

3A Sensitivity of baroclinic transport to horizontal diffusivity

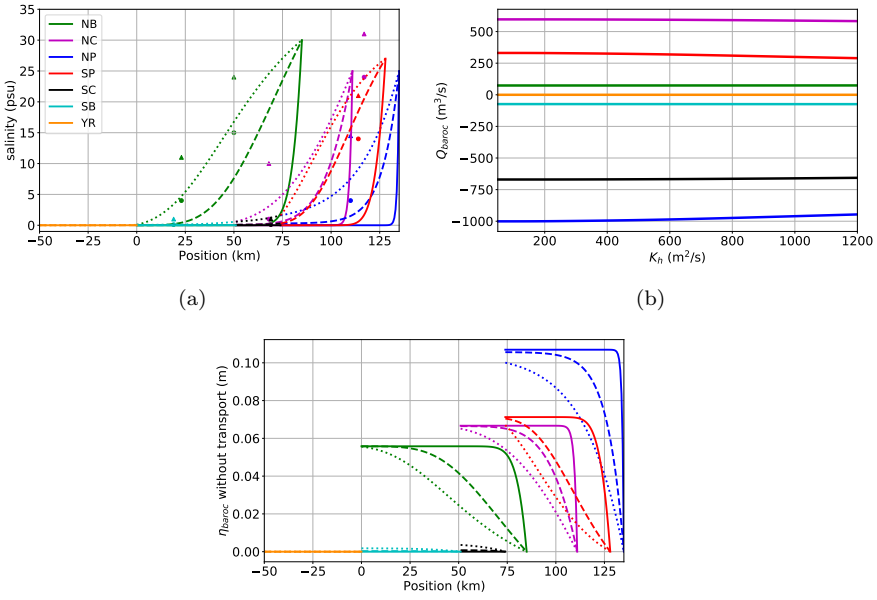

Figure 3.10: a. Tidally-averaged salinity profile for the reference case computed with $K_h = 50\,\mathrm{m^2\,s^{-1}}$ (dotted), $K_h = 500\,\mathrm{m^2\,s^{-1}}$ (solid) and $K_h = 1200\,\mathrm{m^2\,s^{-1}}$ (dashed). Dots (triangles) are measurements made at low (high) water slack (Zhang et al., 2011). b. Sensitivity of the net water transport induced by baroclinic forcing to K_h. c. Subtidal water level directly created the baroclinic forcing in each channel for different K_h. Water levels at the seaward side of each channel are set to 0.

In contrast to a single channel, in which the transport is independent of the salinity (Cheng et al., 2010, Dijkstra et al., 2017a), in channels of a network, however, the transport due to density-driven flow depends on the salinity, for which salinity equation (Eq. (3.2.4)) is employed. To test the sensitivity of the baroclinic transport to salinity, horizontal diffusivity K_h is varied between $50-1200\,\mathrm{m^2\,s^{-1}}$. The resulting salinity is compared to the observation made by Zhang et al. (2011) (Fig. 3.10(a)). This shows that the bounds on K_h envelope the observations and thus capture the uncertainty. However, in all channels of the network, the net water transport induced by the baroclinic forcing is not sensitive to the value of K_h (Fig. 3.10(b)). This lack of sensitivity can be easily explained by the subtidal transport mechanism for networks. The subtidal

water level created by the baroclinic forcing in each channel (Fig. 3.10(c)) is not continuous at branching points and therefore results in pressure difference at vertex points. A barotropic pressure needs to compensate for this and creates additional return flow that generates the subtidal transport. Although a larger value of K_h leads to longer salt intrusion length, the salt intrusion limit (e.g., 1 psu) in most channels is still bounded within each channel. The baroclinic pressure built up in one channel depends on the salinity difference at the ends of the channel and hence hardly changes with K_h (Fig. 3.10(c)). This in turn leads to the net water transport due to baroclinic forcing remaining the same for different K_h. In other words, for a well-mixed estuary, as long as the salt intrusion limit does not move significantly from one channel to another, the influence of K_h on the net water transport is negligible. In the North Passage (NP), for K_h larger than $500\,\mathrm{m^2\,s^{-1}}$, the salt intrusion limit moves to the South Branch and thereby causes the transport in the NP slightly increases. Following the same reason, increasing river discharge causes the salt intrusion limits to move further seaward such that these limits remain in the sea channels and hence the transport due to density-driven flow is unaffected.

4

Dependence of turbidity maxima on fluvial sediment input and local deepening/narrowing

This chapter is based on the manuscript Wang, J., Dijkstra, Y. M., and de Swart, H. E. (2022) Turbidity maxima in estuarine networks: dependence on fluvial sediment input and local deepening/narrowing with an exploratory model, accepted by Frontiers in Marine Science.

Abstract

An estuarine turbidity maximum (ETM) results from various subtidal sediment transport mechanisms related to e.g., river, tides, and density gradients, which have been extensively analysed in single channel estuaries. However, ETMs have also been found in estuaries composed of multiple interconnected tidal channels, where the water and suspended fine sediments are exchanged at the junctions with the possible occurrence of sediment overspill. The overall aim of this study is to understand the processes that determine the ETM dynamics in such channel networks. Specifically, focusing on the ETM formation due to sediment transport by river flow and density-driven flow, the dependence of ETM locations in an idealised three-channel network on fluvial sediment input and the local deepening and narrowing of a seaward channel is investigated. Sensitivity results show that, keeping river discharge fixed, a larger fluvial sediment input leads to the upstream shift of ETMs and an increase in the overall sediment concentration. Both deepening or narrowing of a seaward channel may influence the ETMs in the entire network. Furthermore, the effect of either deepening or narrowing a seaward channel on the ETM locations in the network depends on the system geometry and the dominant hydrodynamic conditions. Therefore, the response of the ETM location to local geometric changes can only be understood by analysing the dominant sediment transport mechanisms. Additional to the convergence of sediment transport mechanisms in single estuarine channels, ETM dynamics in networks is found to be strongly affected by net sediment transport between the branches of a network. We find that considering the sensitivity of net sediment transport to geometric changes is needed to understand the changing ETM dynamics observed in a real estuarine network.

4.1 Introduction

Estuarine turbidity maxima (ETMs) are locations where a local maximum in subtidal suspended sediment concentration is attained in estuaries. They have a large impact on the estuarine ecosystem functioning by, e.g., light attenuation (McSweeney et al., 2017) and inhibited primary production (Cloern et al., 2016). They also lead to enhanced deposition of sediment that hampers the accessibility of ports, which requires constant maintenance dredging in navigational channels (van Maren et al., 2015). It is therefore important to acquire knowledge about the processes that cause their presence and how they respond to human interventions such as dredging and the construction of dams and training walls.

Available literature (for a review see Burchard et al., 2018) reveals that many processes may cause the manifestation of ETMs. Interestingly, all these mechanisms identified for ETMs are considered in estuaries that consist of a single channel. However, many estuaries consist of a network of interconnected channels (e.g., those of the Pearl and Yangtze in China, Rhine-Meuse-Scheldt in the Netherlands, and Mahakam in Indonesia). Field observations in such estuarine networks have revealed the existence of ETM in multiple channels at the same time (e.g., Salahuddin and Lambiase, 2013, Wan and Zhao, 2017). The complexity of networks over single channels arises from, e.g., the exchanges of water and fine sediments between different channels (McLachlan et al., 2020). This may cause the net sediment transport in one channel to be landward, hereafter referred to as sediment overspill. The physical processes related to ETM formation have not been studied in the context of channel networks.

Hence, the focus of this study is on gaining a more fundamental understanding of the mechanisms that determine the ETM dynamics in estuarine channel networks. Specifically, the aim is to understand the dependence of ETMs in an estuarine network on fluvial sediment discharge and on changes in depth and width in one channel of the network. To do so, the contributions and sensitivity of various physical processes and of sediment overspill between channels will be investigated. In this study, we focus on estuaries where the transport of sediment is mainly due to river flow and density-driven flow.

To address these aims, an idealised semi-analytical width-averaged model of an estuarine network will be developed and analysed. This choice is motivated by earlier work (see e.g., Chernetsky et al., 2010), in which it was demonstrated that such a model allows for separating the contributions of various physical processes to the transport and accumulation zones of fine sediments in single channels. Furthermore, an idealised model is fast and flexible, which makes it suitable for extensive sensitivity analysis. The model will be applied to an idealised three-channel network. Thereafter, to discuss the implications of considering human interventions, robust sensitivity results will be generalised and discussed within the literature.

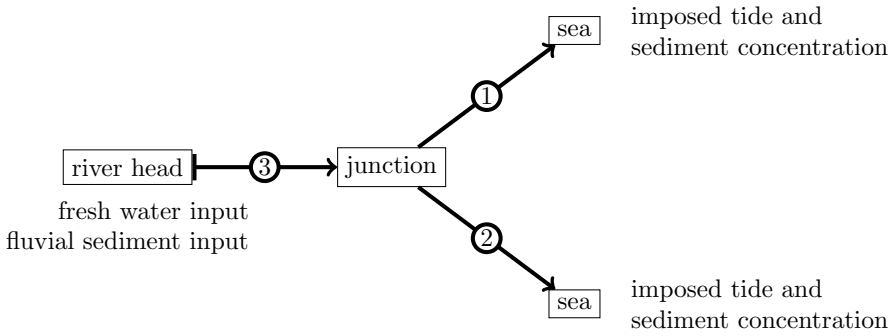

Figure 4.1: Sketch of the three-channel estuarine network considered in this study. Numbers in circles indicate channel numbers.

The model and methods of analysis are detailed in Section 4.2 and 4.3, respectively. Results are presented in Section 4.4, followed by a discussion (Section 4.5) and the conclusions (Section 4.6).

4.2 Model

The model used to study the ETM dynamics is an extension of *iFlow* (Dijkstra et al., 2017a) to a network. The iFlow model is a modular modelling framework for a systematic analysis of the width-averaged water motion and sediment transport in a tidally dominated estuarine system. Here, the geometry, water motion, and suspended sediment dynamics will be briefly described and the key aspects of the model will be stated with the matching conditions for suspended sediment. The reader is referred to Dijkstra et al. (2017a) for the full governing equations and boundary conditions within each channel.

4.2.1 Geometry and water motion

The network considered in this study is shown in Fig. 4.1. Each channel j (where $j = 1, 2, 3$) has a length L_j and is represented by a constant depth H_j. Both the transverse and longitudinal bed slopes are 0 in all channels. Positions in each channel are specified by Cartesian coordinate systems x_j and z_j, where x_j is the along-channel coordinate increasing from the landward boundary ($x_j = 0$) to the seaward boundary ($x_j = L_j$) and the z-axis points vertically upward from the bottom $z_j = -H_j$ to the free water level $z_j = \eta_j$ with respect to the mean sea level $z = 0$. The depth-independent width B_j is either constant or an exponential profile

$$B(x) = B_o \exp\left(\frac{x - L}{L_b}\right), \tag{4.2.1}$$

where B_o is the channel width at $x = L$ and L_b is the upstream width convergence length scale. Here and further in this chapter, the channel indices are omitted for legibility if the equation holds for all channels.

Neglecting the Coriolis effect and horizontal turbulent diffusion, the water motion in all channels is governed by the Reynolds-averaged and width-averaged shallow water equations (Ianniello, 1977). These determine the horizontal velocity $u(x, z, t)$, the vertical velocity $w(x, z, t)$, and the level of the free surface $\eta(x, t)$ with respect to $z = 0$ in every channel, where t denotes the time. Turbulence in the model is determined by a vertical eddy viscosity A_v, which is assumed to be constant in the vertical and in time and is proportional to the mean water depth. A linear equation of state is assumed, in which the water density depends on only a prescribed tidally and depth-averaged salinity through the haline contraction coefficient β_s.

The water motion is externally forced by a prescribed semi-diurnal (M_2) tidal water level at every seaward boundary and a tidally-averaged river discharge at the landward boundary. The water motion in different channels is connected assuming the conservation of mass and momentum (van de Kreeke, 1988).

4.2.2 Suspended sediment dynamics

The modelled suspended sediment in all channels is assumed to consist of one non-cohesive fine sediment fraction with uniform grain size d_s, dry density ρ_s, and constant settling velocity w_s. In every channel, the width-averaged sediment concentration $c(x, z, t)$ is governed by the suspended sediment mass balance. Following Smith and McLean (1977), the erosive flux at the bed is assumed to be proportional to the magnitude of the bottom stress τ_b and to the availability (Friedrichs et al., 1998), i.e.,

$$E = \hat{M} \frac{w_s \rho_s}{\rho_0 g' d_s} |\tau_b(x, t)| f(x), \tag{4.2.2}$$

where ρ_0 is the reference density of water, $g' = \frac{g}{\rho_0}(\rho_s - \rho_0)$ is the reduced gravity, and $\hat{M}$ is the erosion parameter. Here, f is the availability that measures the subtidal abundance of sediment available for erosion near the bed. In this study, only the case $0 < f \ll 1$ is considered. The availability $f(x)$ is determined using the morphodynamic equilibrium condition (Friedrichs et al., 1998, Talke et al., 2009, Chernetsky et al., 2010). Essentially, the morphodynamic equilibrium implies two assumptions have been made: the tidally averaged amount of sediment in suspension does not change over a tidal cycle and the tidally averaged deposition is balanced by the tidally averaged erosion near the bed. Consequently, the net sediment transport $\mathcal{F}$ is constant in every channel. Denoting the averaging over a tidal cycle by $\langle \cdot \rangle$, it reads

$$\mathcal{F} = \left\langle B \int_{-H}^{\eta} \left(uc - K_h \frac{\partial c}{\partial x} \right) \mathrm{d}z \right\rangle, \tag{4.2.3}$$

where K_h is a constant horizontal eddy diffusivity.

A time-mean, depth-averaged sediment concentration c_{sea} is prescribed at the seaward boundary of each sea channel and a tidally averaged fluvial sediment mass flux $\mathcal{F}_{\text{river}}$ is imposed at the river head. Sediment concentration in different channels is matched through the mass conservation of sediment. Moreover, it is assumed that the depth-averaged subtidal concentration is continuous at each junction. For the network in Fig. 4.1, the matching conditions at the junction read

$$\bar{c}_1 = \bar{c}_2 = \bar{c}_3, \qquad \text{at the junction,} \tag{4.2.4a}$$

$$\mathcal{F}_3 = \mathcal{F}_1 + \mathcal{F}_2, \qquad \text{at the junction,} \tag{4.2.4b}$$

where a bar denotes the average over depth and a tidal cycle, i.e.,

$$\bar{c} = \frac{1}{H} \left\langle \int_{-H}^{\eta} c \, \mathrm{d}z \right\rangle \tag{4.2.5}$$

is the depth-averaged subtidal concentration.

4.3 Methods and design of experiments

4.3.1 Solution method

Note that the erosion strength is proportional to sediment availability f. As all terms in the sediment concentration equation are linear in c, one can write

$$c = f \, c|_{f=1} \equiv f \, \frac{\hat{C}}{H} \, . \tag{4.3.1}$$

Here, $c|_{f=1}$ is the sediment concentration when there is an unlimited supply of sediment at the bed, and $\hat{C}$ is called the subtidal carrying capacity. Physically, the carrying capacity $\hat{C}$ (kg m^{-2}) is the depth-integrated concentration when there is always sediment available for erosion near the bed, i.e., the subtidal maximum amount of sediment in suspension in the water column over a unit area. Note that in the present model $\hat{C}$ is fully determined by the water motion.

The governing equations for water motion and suspended sediment involve nonlinear terms and various time scales. Hence, approximate solutions are constructed by using a perturbation expansion and harmonic decomposition (e.g., Ianniello, 1977, Chernetsky et al., 2010). The reader is referred to the user manual of iFlow (supporting information of Dijkstra et al. (2017a)) for details about the derivation and solutions. It is assumed that the water level variation is much smaller than the mean water depth and the semi-diurnal (M_2) frequency is the most dominant component of water motion. It follows that the water motion and suspended sediment concentration contain at least a subtidal, M_2, and M_4 component. Higher overtides are ignored here (M_6,

M_8, $\cdots$). Application of the morphodynamic equilibrium condition in every channel yields an expression for the constant net sediment transport $\mathcal{F}$ of the form (Chernetsky et al., 2010)

$$\mathcal{F} = BT(x)f + BF(x)\frac{\mathrm{d}f}{\mathrm{d}x}, \tag{4.3.2}$$

where the function T is referred to as the subtidal advective transport capacity per unit (p.u.) width (Dijkstra et al., 2019), i.e., the advective transport p.u. width when the water column is everywhere saturated during the entire tidal cycle. It contains most sediment transport processes such as the transport by residual current and tidal pumping. The quantity F describes dispersive sediment transport capacity p.u. width. The effect of spatial settling lag (de Swart and Zimmerman, 2009) is explicitly contained in both T and F. Therefore, similar to the carrying capacity, the transport capacities T and F are the flow properties that are fully determined by the flow conditions and independent of the actual sediment concentration. In every channel, both T and F are continuous functions of x. Their expressions can be found in the user manual of iFlow (Dijkstra et al., 2017a).

The analytical solution to Eq. (4.3.2) for constant $\mathcal{F}$ is

$$f(x) = \exp\left(-\int_{x_0}^{x}\frac{T}{F}\,\mathrm{d}x'\right)\left(f(x_0) + \mathcal{F}\int_{x_0}^{x}\frac{1}{BF}\exp\left(\int_{x_0}^{x'}\frac{T}{F}\,\mathrm{d}x''\right)\mathrm{d}x'\right). \tag{4.3.3}$$

Here, x' and x'' are dummy variables for integration and x_0 is any location in the channel where the value of availability is specified. Hence, $f_(x)$ is found if the net sediment transport $\mathcal{F}$ is given and availability is known at any location in the channel.

The prescribed concentration at the sea can be converted into availability using

$$\bar{c} = \frac{1}{H}\hat{C}\,f. \tag{4.3.4}$$

The net sediment transport $\mathcal{F}$ in each river channel is the same as the imposed sediment input $\mathcal{F}_{\mathrm{river}}$. Using Eq. (4.3.3) with Eqs. (4.2.4) and Eq. (4.3.4) at the junctions and seaward boundary, the distribution of $\mathcal{F}$ throughout the network and an analytical solution for f and hence the concentration are obtained.

4.3.2 Analysis

In this study, an ETM will be referred to as the local maximum in the depth-averaged subtidal sediment concentration $\bar{c}$. The ETM dynamics will be analysed using the carrying capacity $\hat{C}$ and availability f (Eq. (4.3.4)). Here, it will be briefly described how the changes in $\hat{C}$ and f can be explained. Note that

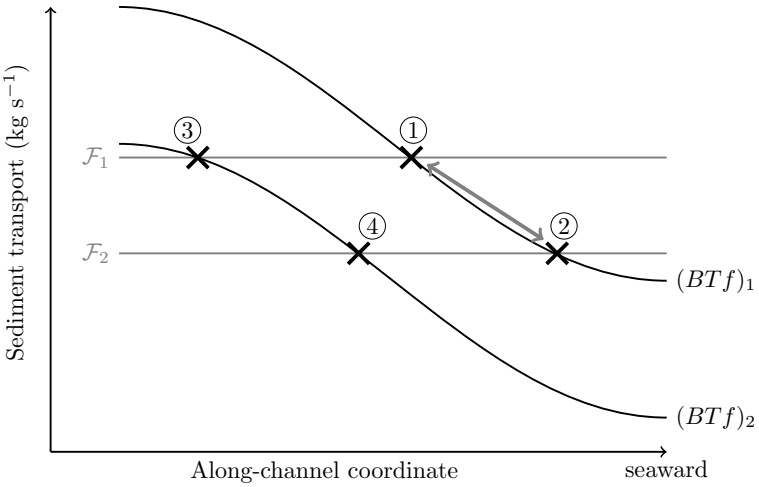

Figure 4.2: A conceptual figure showing the effects of changing net sediment transport $\mathcal{F}$ (grey) and advective transport BTf (black) on the location of sediment trapping (cross), assuming the small influence of net sediment transport on the availability.

the carrying capacity $\hat{C}$ is fully determined by local resuspension. Any change in carrying capacity can be understood by considering the changes in tidal current amplitudes. The availability f describes the average duration over a tidal cycle when sediment is actually available for erosion near the bed. It carries the information of horizontal processes as it results from the net sediment transport $\mathcal{F}$ and transport capacity p.u. width T (Eq. (4.3.2)). The changes in the availability will be explained in terms of the net sediment transport $\mathcal{F}$ and transport capacity p.u. width T.

The location where availability f attains a local maximum will be referred to as the location of *sediment trapping*. The availability gradient $\frac{\mathrm{d}f}{\mathrm{d}x}$ vanishes at the trapping location and Eq. (4.3.2) reduces to $\mathcal{F} = BTf$, i.e., the net sediment transport equals the advective transport. Note that the gradient of transport capacity is required to be negative ($\frac{\mathrm{d}T}{\mathrm{d}x} < 0$) for the existence of the sediment trapping location. An ETM can be observed near the location of sediment trapping if the carrying capacity is spatially uniform (Eq. (4.3.4)). The effects of changing net sediment transport $\mathcal{F}$ and advective transport BTf on sediment trapping location are conceptualised in Fig. 4.2. The intersection ① of $\mathcal{F}_1$ and $(BTf)_1$ is the location of sediment trapping (subscript is the channel index). A reduced net sediment transport $\mathcal{F}_2$ causes the location of sediment trapping to move seaward to the location of crossing ②. Keeping the net sediment transport $\mathcal{F}_1$ fixed, a reduced advective transport $(BTf)_2$ leads to the sediment trapping location shifting landward to the location of crossing ③.

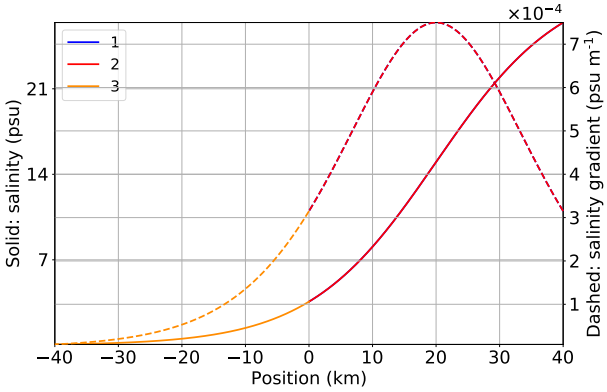

Figure 4.3: The salinity (solid line) and its gradient magnitude (dashed line) for all experiments.

The combination of the two changes leads to the trapping location crossing ① travelling to crossing ④. Depending on the gradient of the advective transport, the sediment trapping location may move in either direction with respect to the location of crossing ①. In Fig. 4.2, it moves slightly landward.

Following the definition for salt water overspill (Wu et al., 2006), sediment overspill is observed in a channel if the net sediment transport $\mathcal{F}$ is negative (landward) in that channel.

4.3.3 Design of experiments

The default parameter values for the reference case of the idealised three-channel system (Fig. 4.1) are contained in Table 4.1. Channel 3 is made sufficiently long (1040 km), such that the tidal influence vanishes at the tidal limit. The area of interest in channel 3 is the most seaward 40 km. The water motion is forced by a constant river discharge $Q_{\text{river}} = 1000\ \text{m}^3\,\text{s}^{-1}$ (positive value indicates seaward) from the landward boundary of channel 3 and M_2 water level amplitude of 1 m at the seaward boundary of both channel 1 and 2. A subtidal depth-averaged sediment concentration $c_{\text{sea}} = 0.05\ \text{kg}\,\text{m}^{-3}$ is prescribed at the seaward boundary of channel 1 and channel 2 and the fluvial sediment input is $\mathcal{F}_{\text{river}} = 50\ \text{kg}\,\text{s}^{-1}$, imposed at the river head. The prescribed salinity profile and its gradient are shown in Fig. 4.3. Note that the three channels share the same along-channel coordinate, where $x = 0$ is the junction.

In order to address the specific aim, three sets of experiments will be conducted to show the sensitivity of the ETM dynamics to different parameters. First, the fluvial sediment input is varied from 0 to $100\,\text{kg}\,\text{s}^{-1}$, while keeping the fresh water discharge fixed. This is equivalent to varying an imposed sediment concentration at the landward boundary. Second, the fluvial sediment

	Parameter	Unit	Default	Exp 1	Exp 2	Exp 3
Q_{river}	River discharge	$\text{m}^3\,\text{s}^{-1}$	1000			
$\mathcal{F}_{\text{river}}$	Fluvial sediment input	$\text{kg}\,\text{s}^{-1}$	50	0-100	50	
$L_{1,2,3}$	Channel length	km	40, 40, 1040			
B_1	Channel 1 width	m	500			see text
B_2	Channel 2 width	m	500			
B_3	Channel 3 width	m	1000			
H_1	Channel 1 mean depth	m	15		5-20	13
H_2	Channel 2 mean depth	m	11		13	
H_3	Channel 3 mean depth	m	13			
ρ_0	Reference water density	$\text{kg}\,\text{m}^{-3}$	1000			
ρ_s	Sediment dry density	$\text{kg}\,\text{m}^{-3}$	2650			
g	Acceleration of gravity	$\text{m}\,\text{s}^{-2}$	9.81			
s_f	Slip parameter	$\text{m}\,\text{s}^{-1}$	0.001			
A_v	Vertical eddy viscosity	$\text{m}^2\,\text{s}^{-1}$	$0.0005H$			
K_v	Vertical eddy diffusivity	$\text{m}^2\,\text{s}^{-1}$	$0.0005H$			
K_h	Horizontal eddy diffusivity	$\text{m}^2\,\text{s}^{-1}$	100			
β_s	Haline contraction coef.	psu^{-1}	7.6×10^{-4}			
w_s	Settling velocity	$\text{m}\,\text{s}^{-1}$	2×10^{-3}			
d_s	Sediment grain size	m	2×10^{-5}			
$\hat{M}$	Erosion parameter		10^{-3}			

Table 4.1: Parameter values

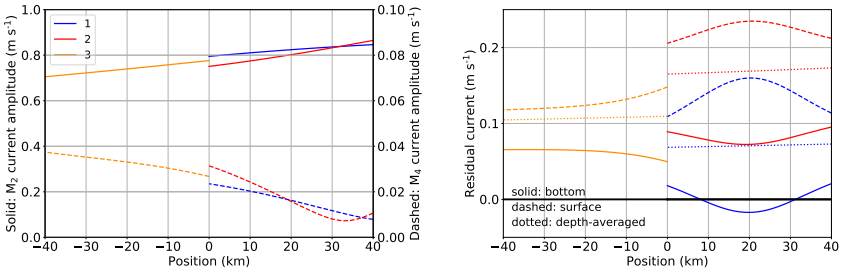

(a) (b)

Figure 4.4: Tidal and subtidal currents for the reference case. (a) Depth-averaged M_2 (solid lines) and M_4 (dashed lines) current amplitudes. (b) Residual currents on the bottom (solid lines), near the surface (dashed lines), and depth-averaged (dotted lines).

input is reset to $50\,\mathrm{kg\,s^{-1}}$, the mean water depth in all channels is set to 13 m, and the mean water depth in channel 1 is varied from 5 to 20 m. Third, the depth of channel 1 is set to 13 m and its width at the sea is varied from 500 to 2000 m, with its width at the junction fixed at 500 m, i.e., increasing width divergence. Its width profile follows Eq. (4.2.1).

4.4 Results

4.4.1 Reference case

The spatial structure of the subtidal concentration is determined by the current, the characteristics of which are shown in Fig. 4.4. The width and depth-averaged M_2 tidal current amplitudes (Fig. 4.4a, solid) are around $0.8\,\mathrm{m\,s^{-1}}$ and slightly decrease upstream. They are one order of magnitude larger than that of the internally generated M_4 overtide (dashed line), which increases upstream. The phase of the M_2 tidal current decreases upstream in all channels, from which it follows an almost spatially uniform upstream phase velocity of $10\,\mathrm{m\,s^{-1}}$ (Fig. S14 in Supplementary information). The internally generated overtides (M_4) are phase-locked to the forcing tide (M_2). The phase speed of the M_4 current is also about $10\,\mathrm{m\,s^{-1}}$. The residual current is seaward everywhere at the surface (dashed line) and is landward near the bottom (solid line) in channel 1 for x between 10 and 30 km (Fig. 4.4b). This is due to the density-driven exchange flow by construction (imposed salinity field), as follows from Fig. S15, which shows all components in the residual flow. The depth-averaged residual current (dotted line) is seaward in all channels due to the prescribed river discharge. In channel 3, it is slightly larger than the river flow velocity ($\frac{Q_{\mathrm{river}}}{B_3 H_3}$). This is because the latter is a mass transport velocity, which also

accounts for Stokes transport by the tidal wave. This difference vanishes at the river head where the river discharge is imposed. The depth-averaged residual current is much larger in channel 2 than that in channel 1.

The subtidal suspended sediment concentration in all three channels for the reference case is shown in Fig. 4.5a, with the depth-averaged values contained in Fig. 4.5b. Two ETMs can be observed. One is near $x = 10$ km in channel 1 and the other is near $x = 15$ km in channel 2. The along-channel structure of the concentration is mainly controlled by the structure of the availability f (Fig. 4.5c, solid line). In every channel, the carrying capacity $\hat{C}$ (Eq. (4.3.1)) follows the M_2 current amplitude and it increases downstream (Fig. 4.5c, dashed line). This results in a small shift of the locations of the ETM towards the sea with respect to the locations of the sediment trapping (maximum in f).

Fig. 4.5d shows the net sediment transport $\mathcal{F}$ (solid line) together with the advective transport BTf (dashed line). Each of the downward intersections of the net sediment transport $\mathcal{F}$ and advective transport BTf corresponds to a sediment trapping location and is indicated by a cross, confirming the two sediment trapping locations near $x = 10$-15 km. The net sediment transports in channel 1 and channel 2 are $3\,\mathrm{kg\,s^{-1}}$ and $47\,\mathrm{kg\,s^{-1}}$, respectively, with the sum the same as the imposed net sediment transport in channel 3 ($\mathcal{F}_3 = 50\ \mathrm{kg\,s^{-1}}$). Sediment overspill is not observed in the reference case.

In Fig. 4.5e, along-channel profiles of the total transport capacity per unit width T are shown (black lines), as well as its various components. In this particular setting, the most dominant contributions to T are the residual transports by density-driven flow (baroclinic, magenta) and river flow (cyan). The density-driven flow imports sediment from the sea in channel 1 and exports sediment into the sea through channel 2. The river flow flushes sediment seaward in all channels. All other contributions to T, such as the transport of sediment by tidally rectified currents, tidal pumping, sediment dispersion, and spatial settling lag, are summed in "other" (red).

4.4.2 Fluvial sediment input

The sensitivity of the net sediment transport in channel 1 and channel 2 to the prescribed fluvial sediment input is illustrated in Fig. 4.6. There is a net exchange of sediment from channel 1 to channel 2 of $5\ \mathrm{kg\ s^{-1}}$. This is best seen in Fig. 4.6 for the fluvial sediment input is 0, where the net sediment transports in channel 1 and channel 2 are equal in magnitude but have opposite directions. Additionally, the net sediment transport in both channel 1 and channel 2 are linear in the prescribed fluvial sediment input, meaning that a fixed fraction of the fluvial sediment is allocated into each channel. This is explained in Section S7.

The sensitivity of ETMs in the system to fluvial sediment input is summarised in Fig. 4.7. The black curves in the plots containing the depth-averaged subtidal concentration $\bar{c}$ (top row) and availability f (bottom row) indicate the

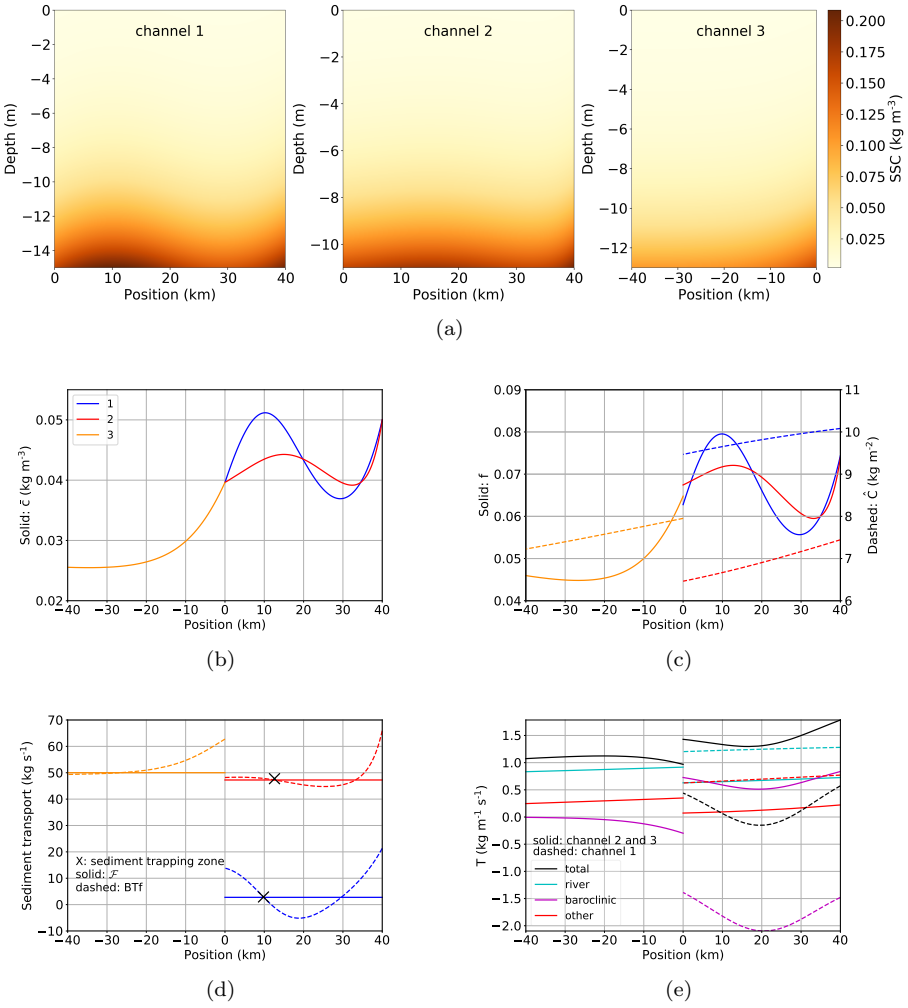

Figure 4.5: Results for the reference case. (a) Subtidal suspended sediment concentration (SSC) in the three channels. (b) The subtidal depth-averaged SSC $\bar{c}$. (c) availability f (solid lines) and carrying capacity $\hat{C}$ (dashed lines). (d) The net sediment transport $\mathcal{F}$ (solid lines) and the advective transport BTf (dashed lines). (e) Difference contributions to T, the transport capacity per unit of width.

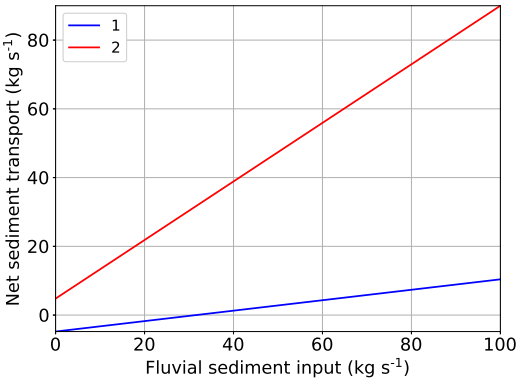

Figure 4.6: Sensitivity of net sediment transport in channels 1 and 2 to fluvial sediment input.

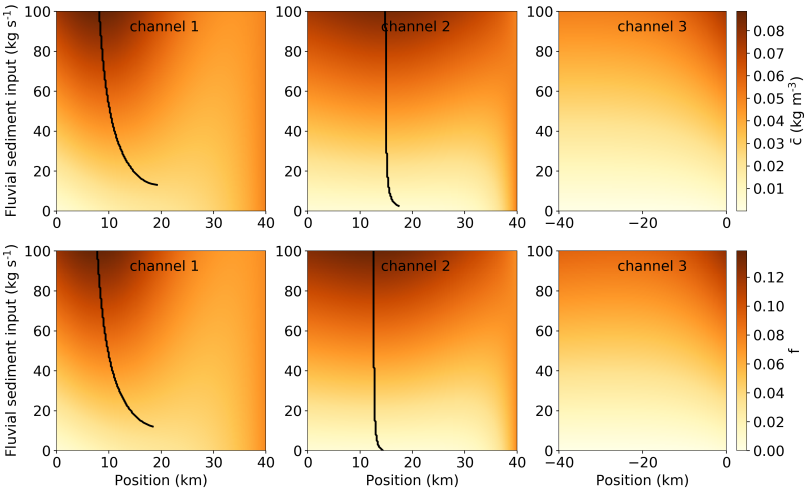

Figure 4.7: Sensitivity of along-channel distributions of depth-averaged subtidal concentration (1st row) and availability (2nd row) to fluvial sediment input. Black curves indicate the location of local maxima.

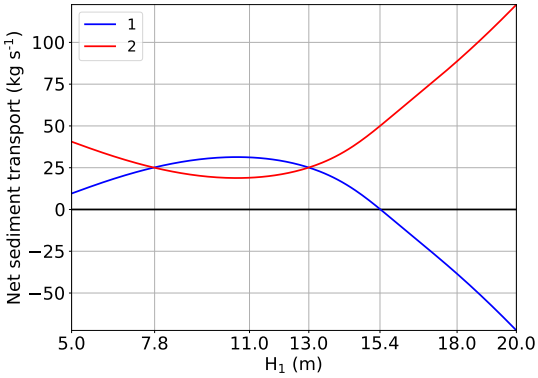

Figure 4.8: Sensitivity of net sediment transport in channel 1 and channel 2 to the mean water depth of channel 1.

location of ETM and zone of sediment trapping, respectively. As fluvial sediment input increases, availability f rises in all channels, which in turn leads to the increase in sediment concentration $\bar{c}$. Changing fluvial sediment input has no influence on the carrying capacity $\hat{C}$ and transport capacity p.u. width T. To analyse the locations of trapping and the associated ETMs, the framework illustrated earlier in Fig. 4.2 is used. With increasing fluvial sediment input, the net sediment transports in both channels increase faster than the advective transport BTf, so that the intersections between advective transport capacity BTF and net sediment transport $\mathcal{F}$ indicating the locations of sediment trapping move upstream. Furthermore, the upstream shift of the location of sediment trapping in channel 2 is much weaker than that in channel 1, albeit channel 2 receives more sediment from the upstream channel. This is because the magnitude of availability in channel 2 increases faster than that of channel 1 locally near the ETM location (Fig. 4.2).

4.4.3 Local deepening

In this experiment, the depths of both channel 2 and channel 3 are 13 m, while varying the depth of channel 1. Fig. 4.8a shows the sensitivity of net sediment transport in both channel 1 and channel 2 to the mean water depth of channel 1 H_1. When H_1 is also 13 m, channel 1 and channel 2 are identical. In that case, the fluvial sediment input is equally distributed into channel 1 and channel 2. Net sediment transport in channel 1 is larger than that in channel 2 when H_1 is between 7.8 and 13 m. Sediment overspill is observed in channel 1 for H_1 larger than 15.4 m.

To analyse and understand the dependence of the ETM location on the local deepening of channel 1, the sensitivities of along-channel distributions of

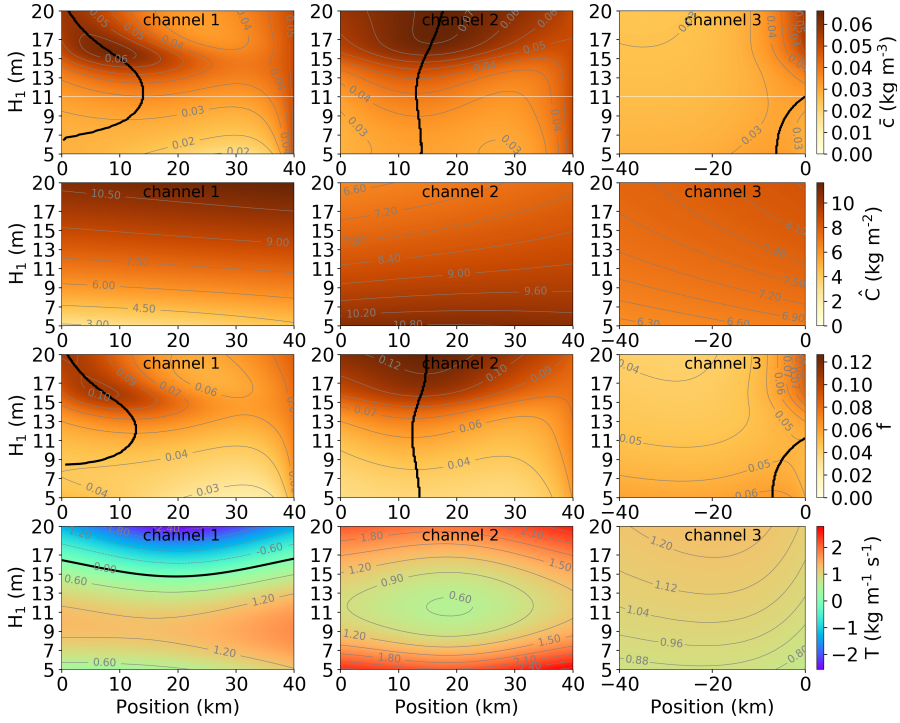

Figure 4.9: Sensitivity of along-channel profiles of depth-averaged subtidal concentration (1st row), carrying capacity p.u. width (2nd row), availability (3rd row), and transport capacity (4th row) to the mean water depth of channel 1. The white line in the first row is where $H_1 = 11$ m.

depth-averaged subtidal concentration $\bar{c}$ (1st row), carrying capacity $\hat{C}$ (2nd row), availability f (3rd row), and transport capacity p.u. width T (4th row) to channel 1 mean water depth H_1 are presented in Fig. 4.9. For $H_1 = 5$ m, there is an ETM in channel 2 and channel 3 (1st row). As H_1 increases, the ETM in channel 2 slightly moves upstream and the ETM in channel 3 moves downstream towards the junction and disappears. A third ETM appears in the system in channel 1 when its depth reaches about 7 m and shifts rapidly downstream for increasing depth. For $H_1 > 11$ m, the shift of the ETMs in both channel 1 and channel 2 changes direction. The concentration in the ETM in channel 2 gradually increases with the depth of channel 1, whereas the intensity of the ETM in channel 1 attains a maximum when $H_1 \approx 16$ m. The concentration at the sea ($x = 40$ km) in both channel 1 and channel 2 is unaffected by the depth of channel 1 due to the imposed boundary condition.

The carrying capacity $\hat{C}$ (2nd row) in each channel changes with little along-channel variation to the depth of channel 1 H_1. In channel 2 and channel 3, the changes in the carrying capacity are due to the changing erosion strength caused by the M_2 tidal current amplitudes. Since the carrying capacity scales with depth (Eq. (4.3.1)), the changes in $\hat{C}$ of channel 1 characterise the along-channel uniform effect of increasing depth. As the depth of channel 1 increases from 5 to 20 m, the relative changes in carrying capacity are 250%, −44%, and 22% in channel 1, channel 2, and channel 3 respectively.

The dependence of availability f (3rd row) on the mean water depth of channel 1 H_1 in every channel is qualitatively the same as that of the concentration in the first row of Fig. 4.9, because the carrying capacity is fairly uniform in along-channel direction (Eq. (4.3.1)).

To further understand the response of the location of maximum availability f to increasing H_1, the advective sediment transport capacity p.u. width T (4th row) will be analysed. The black contour in the plots for the T is the 0 level. For increasing depth of channel 1 H_1, the changes of T in channel 1 and in channel 2 are on average opposite. This is because of the net sediment transport associated to the net water transport. Since the sum of the net water transports in channel 1 and channel 2 is the prescribed river discharge, an increase in the net water transport in one of the channels implies a decrease in the net water transport in the other. Consequently, the advective transport capacities in channel 1 and channel 2 respond oppositely to increasing H_1.

Here, it will be explained what causes the different responses of the ETM locations for H_1 smaller and larger than 11 m in both channel 1 and channel 2. For increasing H_1, the depth of channel 2 remains 13 m. Hence, the sediment transport in channel 2 is only influenced by the changing net water transport, primarily due to river flow and density-driven flow. The net water transport due to river flow scales with depth, while the net water transport due to density-driven flow scales with depth squared (see Chapter 3). For a relatively small depth of channel 1 ($H_1 < 11$ m), the river flow contribution to the sediment transport capacity T in channel 2 is more important than the

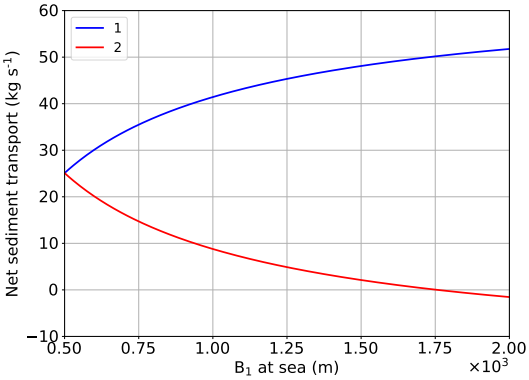

Figure 4.10: Sensitivity of net sediment transport to the width of channel 1 at sea.

density-driven flow contribution (Fig. S16). The increasing H_1 therefore leads to weaker river flow and less seaward net sediment transport in channel 2. The sediment transport capacity in channel 2 decreases more rapidly than the net sediment transport, causing the upstream shift of the ETM in channel 2 (Fig. 4.2). For a relatively large depth of channel 1 ($H_1 > 11$ m), the density-driven flow contribution to the sediment transport capacity T in channel 2 is more important. Hence, a larger H_1 enhances the seaward net water and sediment transports due to density-driven flow in channel 2 that leads to the ETM in channel 2 shifts seaward. As increasing H_1 has opposite effects on the sediment transport due to river flow and density-driven flow, the response of the ETM in channel 1 is opposite to that in channel 2. The migration of the ETM in channel 1 is larger in magnitude than that in channel 2. This is because the exchange flow pattern in channel 1 is intensified by its increasing depth, which is the only difference between the two channels in terms of the residual flow contribution to sediment transport.

4.4.4 Channel widening

In this experiment, the mean water depth is 13 m in all channels. When the width of channel 1 B_1 at the sea is 500 m, channel 1 and channel 2 are geometrically the same, with net sediment transport being equally distributed over the two channels (Fig. 4.10a). As B_1 at the mouth increases (i.e., width divergence of channel 1 increases), more river discharge is allocated to channel 1. Therefore, the river current increases in channel 1 and decreases in channel 2, which directly causes the net sediment transport to increase in channel 1 and to decrease in channel 2 by river flushing. When B_1 at the sea reaches 2 km, the density-driven flow contribution to sediment transport is still dominant in channel 2. In channel 1, however, river and other contributions exceed that

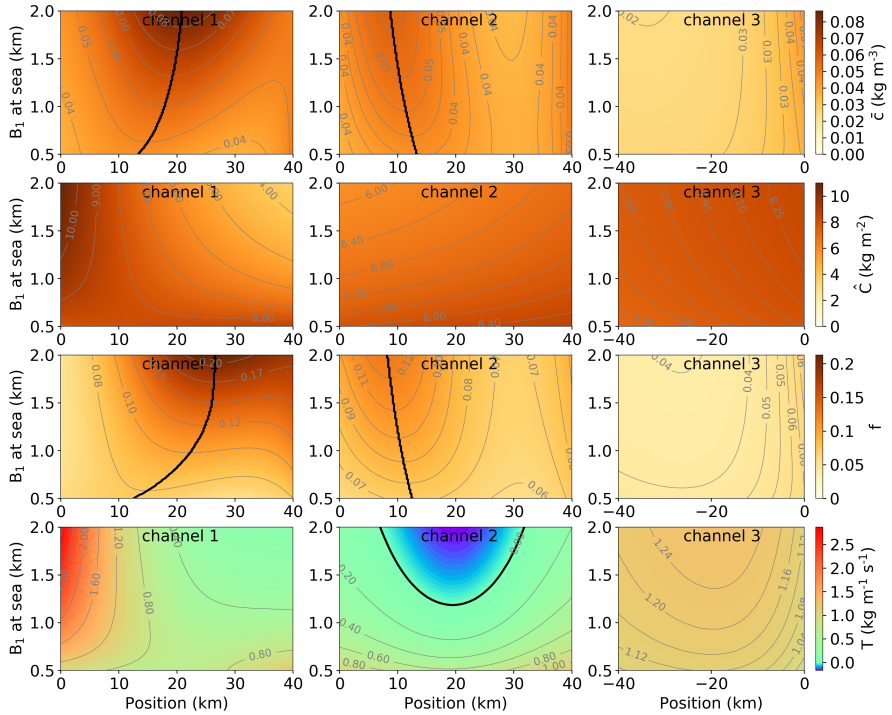

Figure 4.11: Sensitivity of along-channel distribution of depth-averaged subtidal concentration (1st row), transport capacity p.u. width (2nd row), availability (3rd row), and carrying capacity (4th row) to the width of channel 1 at the sea.

of the density-driven flow near the junction (Fig. S17). Sediment overspill is observed in channel 2 for B_1 at the mouth larger than 1.75 km.

The sensitivity of the ETM dynamics to the width divergence of channel 1 is summarised in Fig. 4.11. As the width of channel 1 B_1 increases from 5 to 20 km, the ETM in channel 1 gradually shifts downstream and intensifies by a factor of up to 2 (1st row). In channel 2, the ETM slightly moves upstream and the concentration increases from 0.04 to 0.065 kg m^{-3} at the ETM. No ETM is observed in channel 3, where the concentration is nearly unaffected by the width divergence of channel 1.

The changes in the carrying capacity $\hat{C}$ in all channels are due to the changes in the tidal current amplitudes (2nd row). In channel 1, the carrying capacity $\hat{C}_1$ hardly changes near the junction, while a noticeable reduction can be observed near the sea. This is because the tidal current in channel 1 near the junction is constrained by that in channel 2, the upstream tidal amplification due to stronger upstream width convergence in channel 1 results in the reduc-

tion in the tidal current downstream. Consequently, the erosion in channel 1 is decreasing downstream for stronger upstream width convergence, which is reflected in the carrying capacity $\hat{C}_1$. There is an almost uniform decrease in the carrying capacity along channel 2. In channel 3, little change in the carrying capacity can be observed.

The availability f in all channels again responds in a qualitatively similar manner as the concentration to increasing width of channel 1 at the sea (3rd row). However, the downstream shift of the location of sediment trapping is much stronger than that of the ETM in channel 1, as the consequence of the decreasing gradient in the carrying capacity $\hat{C}_1$. Namely, the width variation in channel 1 leads the tidal currents to vary within the channel and hence the carrying capacity is less spatial uniform, causing the location of ETM differs from the location of sediment trapping.

Although B_1 at the sea is being increased, the transport capacity p.u. width T in channel 1 hardly change near the sea, while significantly increasing near the junction (4th row). In channel 2, the transport capacity p.u. width T_2 decreases with increasing B_1 at the sea.

As the density-driven flow is hardly affected by the channel width (Fig. S17), the ETM dynamics is mostly due to the changing distribution of the river discharge. With the widening of channel 1, the river discharge in channel 1 increases but decreases in channel 2. This directly causes the ETM shifts downstream in channel 1 and upstream in channel 2. In channel 1, the enhanced tidal amplifications due to stronger upstream width convergence lead to a higher resuspension rate near the junction, which alleviates the downstream shift of the ETM with respect to the sediment trapping location.

4.5 Discussion

The goal of this study is to gain more insight into the sensitivity of ETMs and the methods for analysing the ETM dynamics in an estuarine network. This study presents the first step, by choosing a simple network geometry and selecting model parameters such that the river flow and density-driven flow is the dominant driver (i.e., gravitational circulation) for ETM formation. This means that results can be qualitatively related to channel network estuaries where gravitational circulation is also important, including the Yangtze (Pu et al., 2016) and Amazon (Geyer, 1993) during the dry season. In nature, also other mechanisms can be important for sediment trapping that results in ETMs, such as tidal pumping in Ems Estuary (Allen et al., 1980) and the Gironde Estuary (Castaing and Allen, 1981), wind-driven current in the Mandovi Estuary (Kessarkar et al., 2009), and topographic trapping in the Columbia River Estuary (Hudson et al., 2017). Although beyond the scope of this study, it is possible to explore the effects of these mechanisms on ETMs in a network by extending the presented modelling framework to a different configuration.

In the application of the results, some important limitations should be recalled. Firstly, the attention has been restricted to availability-limited conditions ($0 < f \ll 1$) and low concentrations that do not affect the water motion. For a system with a higher concentration, even in equilibrium, there can be net deposition over one tidal cycle that contributes to a bottom pool of easily erodible sediment on the bed, where the concentration is limited by erosion. Examples are the Weser estuary (Geyer, 1993), the South Passage in the Yangtze Estuary (Li et al., 2022), and San Francisco Bay (Schoellhamer, 2011). Secondly, the salt intrusion length depends on the channel depth (Geyer and MacCready, 2014, and references therein), which also has an influence on the turbulence model. The effect of depth on the salinity profile and the influence of salinity on turbulence are not considered in this study, which would further complicate the dependence of the ETM locations on the channel depth. Thirdly, the bed slope is assumed to be 0 in both the transverse and longitudinal directions. The sediment transport due to the bed slope can be potentially important (Iwantoro et al., 2022), which can be parametrically accounted for within the presented modelling framework.

Nonetheless, the sensitivity results presented in Section 4.4 contain some robust responses of the ETM dynamics to changing fluvial sediment input and local geometries. These results will be placed into a broader context and ETM responses will be compared with those reported in the literature below.

4.5.1 Fluvial sediment input

In this study, the fluvial sediment input is the imposed net sediment transport at the river head. Fig. 4.6 shows that the net sediment transport in any channel downstream of a junction is proportional to fluvial sediment input (see also Eq. (S7.1)). One of the key findings is, for an ETM near the maximum availability in a channel of an estuarine network, a larger seaward net sediment transport leads to the upstream shift of this ETM and vice versa (Fig. 4.2). This implication is not restricted to the sediment trapping caused by river flow and density-driven flow, but applies in general as long as the concentration does not significantly alter the water motion. These findings are similar to the theoretical results found by Festa and Hansen (1978) using a subtidal model of a single channel. This study shows this conclusion can be extended to the behaviour of ETMs in a network.

It has been observed in several estuarine networks that a reduced fluvial sediment input causes a downstream shift of ETMs. The construction of the Three Gorges Dam in the Yangtze River substantially reduced the fluvial sediment input into the Yangtze Estuary, with the river discharge almost unaffected, which causes the reduction of seaward net sediment transport in all distributary channels (Luo et al., 2022). By analysing in-situ field measurements, combined with the Landsat images from 1979 to 2008 in the Yangtze Estuary, Jiang et al. (2013b) reported that lower fluvial sediment input caused ETMs to

shift seaward. The Pearl Estuary has also experienced a reduction in the fluvial sediment input due to upstream damming over the last two decades. Zhan et al. (2019) studied the inter-annual variability of the suspended sediment concentration in the Pearl Estuary from 2002-2014, when the yearly averaged river discharge was constant, but the fluvial sediment supply decreased. A clear seaward shift of the upstream boundary of the high concentration region was observed. Furthermore, due to the reduced fluvial sediment input in both the Yangtze Estuary and the Pearl Estuary, an overall decline in the sediment concentration was observed (Luo et al., 2022, Zhan et al., 2019), which is also captured by our sensitivity results (Fig. 4.7).

4.5.2 Local deepening and narrowing

Both deepening and narrowing in one channel may affect ETMs in multiple channels (Figs. 4.9 and 4.11). The local change of the channel geometry affects the net sediment transport as well as transport capacity and the shift of the ETMs depends on the specifics of these changes.

Using a subtidal model that accounts for the influence of sediment concentration on water density, Talke et al. (2009) showed that an ETM shifts upstream with increasing depth in a single channel with a fixed river discharge. A larger water depth causes a more intensified exchange flow pattern due to the salinity-induced density-driven flow, leading to the upstream shift of the ETM. In a network, however, the response of the location of an ETM to the deepening is more complex (Fig. 4.9). The essential difference is that the river discharge is fixed at the river head in the upstream channel, but not in the channels that are located seaward of the junction. Hence, instead of the river discharge, one needs to consider the net water transport in each channel. Focusing on the river and density-driven flow, the actual response of the ETM location to the deepening of a channel depends on which process is the dominant contribution to the net water transport, as explained in Section 4.4.3. Hence, deepening may cause either an upstream or downstream shift of the ETM.

Similarly, keeping the river discharge fixed, the decreasing of upstream width convergence (narrowing) in a single channel enhances the river current that tends to shift the ETM downstream. The North Channel of the Yangtze Estuary experienced narrowing and reduction in width convergence as the consequence of a land reclamation project. The ETM indeed shifts downstream, as reported by Teng et al. (2021). To explain this, by careful analysis of remote sensing data in the North Channel under various flow conditions, a conceptual model is proposed to argue that the seaward shift is partly due to the enhanced ebb-dominance that causes a seaward shift of the convergence in sediment transport. Also in the Yangtze Estuary, the first stage of the Deep Waterway Project (DWP) involved only the construction of the training walls in the North Passage (NP), i.e., narrowing and reducing upstream width convergence. However, Jiang et al. (2012) reported that the ETM in the NP slightly shifts upstream

after the first stage of the DWP. The reason is, in a network, the weaker width convergence locally in a channel also decreases the net water transport distributed into this channel, causing less seaward sediment flushing by the net water flow (Fig. 4.10).

4.6 Conclusions

This study shows that, to understand the ETM dynamics in a channel network, it is useful to represent the subtidal sediment concentration by the product of the subtidal carrying capacity and the sediment availability. The former is determined by the erosion pattern due to the tidal current and characterises the capacity of the flow to suspend sediment. The latter features the amount of sediment available for erosion near the bed. The availability is determined such that the subtidal suspended sediment concentration is in equilibrium and net deposition is balanced by the net erosion in every channel. It therefore links the sediment transport and the ETM location. Channels are connected at a junction by requiring the conservation of sediment mass flux and assuming the continuity of depth-averaged subtidal sediment concentration.

For a sufficient long estuarine channel network where the tidal current amplitudes are fairly spatially uniform, the location of an ETM is close to the location of sediment trapping in every seaward channel. Sensitivity results show that, keeping river discharge fixed, a reduced fluvial sediment input reduces the global concentration and causes the downstream shift of the location of sediment trapping and the associated ETM location. Both local deepening and narrowing of one channel affect the ETM dynamics in the entire channel network. The effect of local deepening on the ETM locations is case-specific. This is because, on the one hand, the deepening of a channel in a network enhances the river current in that channel, which shifts the ETM seaward, while on the other hand intensifies the density-driven exchange flow and landward net water transport that shifts the ETM landward. Whereas in the other undeepened channel that shares the same upstream channel with the deepened channel, the river current decreases, which shifts the ETM landward. Although density-driven exchange flow is unaffected, the net water transport due to density-driven flow increases in the seaward direction that shifts the ETM seaward. Hence, the actual response of the ETMs in the network due to the deepening of one of the channels depends on which sediment transport process is more dominant. If an ETM is formed in each of the seaward channels due to density-driven flow and river flow, then the local narrowing of the channel causes the upstream shift of the ETM in the narrowed channel and downstream shift of the ETM in the other channel as the consequence of the redistribution of the water transport. These results have been compared to the ETM dynamics in real world estuarine channel networks. We argue that the observed changing ETM dynamics in a real estuarine network in response to deepening

and narrowing can only be explained by considering the specific processes in a network mentioned above.

5

Synthesis

Estuarine channel networks are estuaries with multiple interconnected channels. Here, conclusions of the preceding chapters that answer the specific research questions formulated in Chapter 1 are provided and further research opportunities are suggested.

5.1 Conclusions

5.1.1 Research question 1

$\mathcal{Q}1$ How do tidal propagation and the distribution of river water transport depend on the river discharge, external tidal forcing, local geometric changes, and sea level rise, when the flow vertical structure is accounted for?

To answer this question, in Chapter 2, a semi-analytical estuarine channel network model was developed to solve the width-averaged linearised water motion in the channels, forced by a sinusoidal tidal water level at every seaward boundary and a constant river discharge at every tidal limit. The river-tide interactions were parametrically accounted for in the turbulence model that computes the friction parameters: the vertical eddy viscosity and bottom slip parameter for both the river and tidal flow. The water motion in the channels was matched at junctions assuming the conservation of mass and the continuity of water level.

Applying the model to the Yangtze Estuary, it was found that an increase in either the river flow or tidal flow enhances the bottom stress and internal

stress experienced by both the river flow and tidal flow. A larger river discharge therefore leads to a reduction in the tidal current and phase speed of the tidal wave through enhanced river-tide interactions. The river water transport in every channel is proportional to the river discharge. However, it is insensitive to the tidal forcing, to which the tidal flow is positively correlated. The distribution of river water transport over the channels is determined by the channel geometry and the friction experienced by the river flow, which depends on tides.

A shortcut channel reduces the water level difference in the channels that it connects. Consequently, the tidal range and the set-up due to river discharge are enhanced in one of the adjacent channels and reduced in the other. Accordingly, the river water transport is reallocated from the channel with a higher residual set-up to the other. The local deepening and narrowing of one channel have opposite effects on both the tidal and river current, because of their opposing impacts on the channel cross-sectional area. Deepening significantly reduces the friction for both the river and tidal flow in the deepened channel and slightly enhances the friction experienced by the river and tidal flow in adjacent channels.

Assuming the prescribed tidal amplitudes are unaffected by the sea level rise, a larger mean water depth increases the channel cross-section area and hence reduces the river current and set-up. It also increases the phase speed of the tidal propagation, which in turn leads to a longer resonance length. Therefore, the effects of sea level rise on tidal range and current depend on whether the system is closer or further away from the resonance and the balance with the declining friction.

5.1.2 Research question 2

$\mathcal{Q}$2 What are the contributions of the river, tides, and horizontal density gradients to the distribution of net water transport in estuarine channel networks and their sensitivities to river discharge, tide, human interventions, and sea level rise?

Besides the mean flow due to the river discharge, mean flow driven by tidal rectification and horizontal density gradients were added to the model in Chapter 3 in order to analyse the distribution of net water transport over the channels. This was achieved by the perturbation method that expands each state variable (free water level and velocities) into a power series of the tidal Froude number, which is much smaller than unity. Compared to the model used in Chapter 2, the additional nonlinear terms responsible for the tidal rectification describe the horizontal advection of both the along-channel and vertical momentum, Stokes transport, and velocity-depth asymmetry. By taking advection into account, the continuity of water level (barotropic static pressure) was replaced by the continuity of total pressure, which contains an additional dynamic pressure due to the water motion. Therefore, the net water transport in every channel is the

sum of the river water transport, tidally rectified transport, and density-driven transport.

Chapter 3 confirmed that the distribution of net water transport over the channels of an estuarine network and the relative importance of these net water transport contributions depend on the geometric and tidal characteristics of the entire system, rather than locally determined near the junctions. In a river channel containing the river head (tidal limit), tidally rectified flow and density-driven flow only influence the vertical profile of the subtidal exchange flow and do not contribute to water transport, similar to a single channel estuary. Hence, the net water transport in a river channel is solely due to the river discharge. However, in a seaward channel of a network, the net water transport is not only due to the density and tides in this channel, but in all channels. The underlying mechanism works as follows. The internal forcing, such as the density gradients and momentum advection, directly contributes to the water level setup/down in every channel, i.e., a barotropic pressure. The transport in each channel has to be such that the total pressure at a junction is continuous. The net transport in each channel therefore depends on the density and tides in all channels. Nonetheless, an estimation of the direction of the net water transport can be made. First, consider density-driven transport. If a seaward channel is the deepest and contains the sharpest density gradient, then the density-driven transport is landward in this channel, because more water level setup (barotropic pressure) can be built up in this channel compared to the others. Second, the net water transport due to tidal momentum advection tends to be seaward in a tidal channel with a significant upstream amplification in the tidal current amplitudes. Third, the velocity-depth asymmetry and the Stokes transport and its return flow may induce more landward net water transport in a channel than others if this channel has the largest tidal range to depth ratio in the network.

The sensitivity of every contribution to the net water transport in the channels of the Yangtze Estuary to river discharge, tidal forcing, local deepening and narrowing, and sea level rise were assessed. The distribution of the net water transport over the channels in the Yangtze Estuary is dominated by the river flow even in the dry season. It is therefore insensitive to the river discharge, which only influences the transport due to the river flow. The net water transport due to tides in every channel scales almost linearly with the external tidal forcing. The deepening of the North Passage increases the river and tidal contributions but decreases the density-gradient contribution to the net water transport in the North Passage. The narrowing due to a reduction in the width convergence in the North Passage primarily causes the channel to receive less river water transport from the upstream channel. The distribution of net water transport in the Yangtze Estuary is not sensitive to sea level rise up to 2 m. This is because every component in the net water transport compensates as the sea level rises.

5.1.3 Research question 3

$\mathcal{Q}$3 What is the dependence of ETMs in an estuarine network on fluvial sediment discharge and on changes in depth and width in one channel of the network?

To understand and analyse the estuarine turbidity maximum (ETM) dynamics in estuarine channel networks, a width-averaged hydrodynamic network model was coupled to a width-averaged suspended sediment concentration model for a single fraction of non-cohesive fine sediment. The sediment concentration model was forced by a prescribed tidally and depth-averaged suspended sediment concentration at each seaward boundary and a fluvial sediment discharge at each river head. The along-channel distribution of the sediment was obtained assuming the morphodynamic equilibrium condition, i.e., over one tidal cycle, the amount of sediment suspended in the water column does not change and the net deposition is balanced by the net erosion on the bed. At junctions, it was assumed that the subtidal horizontal mass flux is conserved and the subtidal depth-averaged sediment concentration is continuous. Compared to the model used in Chapter 3, the hydrodynamic model in Chapter 4 was adjusted in two aspects. First, to better focus on the suspended sediment dynamics, the river-tide interactions were disabled. The vertical eddy viscosity scaled with mean water depth and the slip parameter was constant. Second, to model the sediment transport by tidal pumping, the internally generated overtide was considered.

The developed model was applied to an idealised three-channel estuary, with one river channel debouches into two seaward channels. The geometric characteristics of each channel were designed such that the ETMs were primarily formed due to the river flow and the density-driven flow. Sensitivity results showed that for the same river discharge, a larger fluvial sediment input leads to the upstream shift of all ETMs in the network. The local deepening of a seaward channel causes the ETM in the upstream channel to move downstream. However, the ETMs in the seaward channels may shift in either direction depending on the relative strength of sediment transport due to river flow and density-driven flow. If more sediment is transported by the river flow, the ETM shifts downstream in the deepened channel and upstream in the other seaward channel. Whereas if more sediment is transported by the density-driven flow, the opposite would be observed. The local narrowing of a seaward channel causes the ETM to shift upstream in the narrowed channel and downstream in the other seaward channel.

5.2 Outlook

As a first step to better understand the hydrodynamics and suspended sediment dynamics in estuarine channel networks, several important processes that

deserve future research are neglected in this thesis. They have been described in Section 2.4.2, Section 3.4.2, and Section 4.5, such as the lateral processes (Scully et al., 2009), realistic bathymetry (e.g., tidal flats, Hepkema et al., 2018), adjustment timescale (Geyer and MacCready, 2014), and other sources for exchange flow (e.g., Dijkstra et al., 2017b). Other processes regarding suspended sediment concentration also deserve consideration in the context of estuarine networks, such as the distribution of sediment grain sizes, sediment-fluid interaction, flocculation, and consolidation (Winterwerp and van Kesteren, 2004). Below, the outlook will be provided. First, a few implications for the Yangtze Estuary management will be first given. This will be followed by a discussion of the research opportunities using the modelling framework presented in this thesis.

5.2.1 Implications for the Yangtze Estuary management

Relation between landward net water transport and saltwater spilling-over

It has been shown that, in the Yangtze Estuary, the tidal contribution to the net water transport is responsible for the landward net water transport in the North Branch during the dry season, especially the contributions due to the velocity-depth asymmetry and the Stokes transport and its return flow. It is worth investigating the relationship between the net water transport and the saltwater spilling-over, which at least requires the salt dynamics to be coupled with the hydrodynamics.

Motivated by the correlation between the net water and suspended sediment transports in Chapter 4, it can be hypothesised that a landward net water transport implies saltwater spilling over. Subsequently, the results in Chapter 3 suggest that the saltwater spilling over can be alleviated if the tidal range to depth ratio is reduced in the North Branch. That is, either the tidal range needs to be reduced or the water depth needs to be increased. Since the deepening of the North Branch locally enhances the density-driven flow and may amplify the landward net water transport, the reduction of tidal range should be considered in the North Branch, which can be achieved by e.g., reducing the width convergence by training wall construction. This needs to be further examined by the applications of numerical models.

5.2.2 Research opportunities using the modelling framework of this thesis

Friction experienced by tidal waves

In Chapter 2, the river-tide interaction was described using the friction parameters: the vertical eddy viscosity in the shear stress and the slip parameter

in the bottom stress. They are related to the stress experienced by the flow, which is not the same as the friction experienced by the tidal wave or the river flow.

A few extensions can be made to better describe and understand the friction experienced by the tidal wave. First, the horizontal and vertical frictions should be distinguished. The wave-like solution to the tidal flow contains the wave numbers in both the horizontal and vertical directions. Second, the real part of each of the wave numbers describes the exponential decay of the tidal wave in the corresponding direction. It would be interesting to investigate the sensitivities of these real parts of the wave numbers to different changes.

Wind contribution to the net water flow

In Chapter 3, the net water flow is the consequence of river, tides, and horizontal density gradients. The net water flow can be also attributed to e.g., wind (Lange and Burchard, 2019) and tidal straining (Dijkstra et al., 2017b). Here, the focus is on the wind.

The wind field acts as a momentum input for the water motion on the surface. A constant wind field directly contributes to the net water flow in a network. A time-dependent wind field may contribute to the net water flow through its temporal correlation with the tides. However, to accurately represent the net water flow due to the wind in an estuarine channel network, it is important to adjust the boundary conditions at the sea. This is because the wind alters the sea level on the continental shelf, which causes a different mean sea level at each seaward boundary. The effect of the difference in the prescribed mean sea level on the net water flow can be larger than that of the momentum input to the water in the channels.

Channel matching conditions

Assuming the sediment concentration is well-mixed in the cross-channel direction, it remains an open question that, apart from mass conservation, what is the other appropriate matching condition for sediment concentration at a junction (Wang et al., 1995). Especially when the sediment concentration is higher, the net deposition of sediment into a bottom pool on the bed over one tidal cycle should be allowed (Geyer, 1993, Burchard et al., 2018). This has been achieved in a single channel (Brouwer et al., 2018). However, it is still not physically clear what the continuous quantity is at a junction if such a bottom pool forms near the junction. The availability cannot be continuous: if there is net deposition in one channel near a junction, then there will be net deposition for all channels near the junction. The continuous bottom pool leads to undetermined availability when the concentration is low. The suspended stock cannot be continuous if there is net deposition in every channel near a junction, because this is the case when the suspended stock in every channel at

the junction is the same as the carrying capacity, which is not necessarily continuous. The continuous total stock is a possible candidate. However, the total stock is piece-wise continuous in a single channel (see Appendix of Burchard et al., 2018), i.e., it is not continuous on the boundary of the activated bottom pool. Furthermore, it is recommended to enable the bedload sediment transport in the bottom pool before taking the bottom pool into account during the matching for sediment concentration. Otherwise, the junction may behave as a sediment source without the mass conservation for the bedload sediment.

River turbidity maximum

In this thesis, erosion is only caused by tidal motion. However, in the upstream part of the Yangtze River, the river current velocity is sufficiently high to erode, carry, and transport sediments. Conceptually, in the absence of tides and density gradients, the velocity of the river flow decreases downstream due to the width divergence and the suspended sediment carried by the river flow will be dumped on the bed. This may lead to a locally elevated sediment concentration, which can be studied using an idealised 1D model.

Supplementary information

S1 Time structure of the model solutions

In Eq. (3.2.2), the hydrodynamic equations are projected onto a residual component and onto one that is oscillatory with angular frequency ω. Here, it is briefly explained why this can be done.

The hydrodynamic equations used in this study are the 2DV (width-averaged) shallow water equations:

$$\frac{\partial u}{\partial t} + u\frac{\partial u}{\partial x} + w\frac{\partial u}{\partial z} = -g\frac{\partial \eta}{\partial x} + g\beta_s\frac{ds}{dx} + A_v\frac{\partial^2 u}{\partial z^2}\,, \tag{S1.1a}$$

$$\frac{\partial u}{\partial x} + \frac{\partial w}{\partial z} + \frac{1}{B}\frac{dB}{dx}u = 0\,. \tag{S1.1b}$$

Here, t is time, x an along-channel coordinate and the z-axis points vertically upward. Furthermore, u and w are velocity components in x and z-direction, $z = \eta$ is the sea surface with respect to mean sea level $z = 0$ and s is salinity (which is assumed to be steady). Parameter g is the acceleration due to gravity, β_s is the coefficient of isohaline contraction, and A_v is the vertical eddy viscosity. Finally, B is the channel width, which is assumed to vary exponentially with x (see Eq. (2.2.1)).

These equations are nonlinear, however, it is assumed that the nonlinear terms are small compared to the linear ones (see Chapter 3 and Section S2). Moreover, it is assumed that the water motion is forced by a given, steady river discharge and by prescribed sea surface variations at the seaward boundaries of the domain that consist of a single tidal constituent with angular frequency ω. Consequently, solutions for u, w, η will be Fourier series, e.g.,

$$u = \sum_{n=0}^{\infty} u_n \cos(n\omega t - \varphi)\,,$$

where $u_n(x,z)$ and $\varphi(x,z)$ are amplitudes and phases, respectively. For this reason, the hydrodynamic equations can be projected onto these Fourier components.

In the estuarine tidal networks considered in this study the residual component $n=0$ and the primary tide ($n=1$) dominate over the other components, which are overtides. This follows from the scaling analysis that is presented in Section S2. Thus, only these two components will be considered.

Finally, note that Eqs. (S1.1a)-(S1.1b) can also be written in conservative form:

$$\frac{\partial}{\partial t}(Bu)+\frac{\partial}{\partial x}(Buu)+\frac{\partial}{\partial z}(Buw)=-gB\frac{\partial \eta}{\partial x}+gB\beta_s\frac{ds}{dx}+A_v\frac{\partial^2}{\partial z^2}(Bu)\,, \tag{S1.2a}$$

$$\frac{\partial}{\partial x}(Bu)+\frac{\partial}{\partial z}(Bw)=0\,. \tag{S1.2b}$$

S2 Scaling and perturbation expansion

In order to apply the perturbation expansion, Eqs. (3.2.2)-(3.2.7) are first made dimensionless using scaling arguments so that the relative magnitudes of each term can be identified. For this, the following typical scales are used,

$$t = \omega^{-1}\tilde{t}, \qquad (x, L, L_b) = L_0(\tilde{x}, \tilde{L}, \tilde{L_b}), \qquad u = U_0\tilde{u}, \qquad w = W_0\tilde{W}$$

$$B = B_0\tilde{B}, \qquad (z, H) = H_0(\tilde{z}, \tilde{H}), \qquad \eta = N_0\tilde{\eta}, \qquad \frac{\partial\rho}{\partial x} = \hat{\rho}_x\widetilde{\frac{\partial\rho}{\partial x}},$$

where a tilde implies a dimensionless variable, H_0 is the largest channel depth, $L_0 = \frac{\sqrt{gH_0}}{\omega}$ is the frictionless tidal wave length, B_0 is the largest channel width, N_0 is the largest prescribed tidal elevation amplitude and $\hat{\rho}_x$ is the typical magnitude of the horizontal density gradient. Motivated by the width-averaged continuity, $\frac{\partial u}{\partial x}$ and $\frac{\partial w}{\partial z}$ are of the same order, which implies $W_0 = \frac{H_0}{L_0}U_0$. An approximate balance between local inertia $\frac{\partial u}{\partial t}$ and barotropic pressure gradient $g\frac{\partial\eta}{\partial x}$ is assumed, which gives $U_0 = \frac{gN_0}{\omega L_0}$. Using $L_0 = \frac{\sqrt{gH_0}}{\omega}$, the horizontal velocity scale can be rewritten as $U_0 = \frac{\omega N_0 L_0}{H_0}$. Substituting above scaled variables into the system (3.2.2)-(3.2.7) yields the dimensionless system

$$\frac{\partial\tilde{u}_n}{\partial\tilde{t}} + \varepsilon\left(\tilde{u}\frac{\partial\tilde{u}}{\partial\tilde{x}} + \tilde{w}\frac{\partial\tilde{u}}{\partial\tilde{z}}\right)_n = -\frac{\partial\tilde{\eta}_n}{\partial\tilde{x}} - \Gamma\widetilde{\frac{\partial\rho}{\partial\tilde{x}}}(\varepsilon\tilde{\eta}_0 - \tilde{z}) + \widetilde{A}_{vn}\frac{\partial^2\tilde{u}_n}{\partial\tilde{z}^2}, \tag{S2.1a}$$

$$\frac{\partial\tilde{u}_n}{\partial\tilde{x}} + \frac{\partial\tilde{w}_n}{\partial\tilde{z}} + \frac{L_0}{L_b}\tilde{u}_n = 0, \tag{S2.1b}$$

$$\frac{\partial\tilde{\eta}_n}{\partial\tilde{t}} + \left(\frac{\mathrm{d}}{\mathrm{d}\tilde{x}} + \frac{L_0}{L_b}\right)\int_{-\tilde{H}}^{\varepsilon\tilde{\eta}_n}\tilde{u}_n\,\mathrm{d}\tilde{z} = 0, \tag{S2.1c}$$

where $\Gamma = \frac{gH_0\hat{\rho}_x}{\omega U_0\rho_0}$ is a dimensionless number that describes the relative importance of the horizontal density gradient, $\varepsilon = \frac{N_0}{H_0} = \frac{U_0}{\sqrt{gH_0}}$ is the Froude number, $\widetilde{A}_{vn} = \frac{A_{vn}}{\omega H_0^2}$ is the dimensionless eddy viscosity and the last equation is the depth-integrated width-averaged continuity. Recall that a checkmark on the eddy viscosity coefficient denotes the constant eddy viscosity. The dimensionless boundary conditions are

$$\widetilde{A}_{vn}\frac{\partial\tilde{u}_n}{\partial\tilde{z}} = 0 \quad \text{and} \quad \tilde{w}_n = \frac{\partial\tilde{\eta}_n}{\partial\tilde{t}} + \varepsilon\tilde{u}_n\frac{\partial\tilde{\eta}_n}{\partial\tilde{x}} \qquad \text{at} \quad \tilde{z} = \varepsilon\tilde{\eta}, \tag{S2.2a}$$

$$\widetilde{A}_{vn}\frac{\partial\tilde{u}_n}{\partial\tilde{z}} = \tilde{s}_{fn}\tilde{u}_n \quad \text{and} \quad \tilde{w} = 0 \qquad \text{at} \quad \tilde{z} = -\tilde{H}, \tag{S2.2b}$$

where $\tilde{s}_{fn} = \frac{s_{fn}}{\omega H_0}$ is the dimensionless slip parameter. The dimensionless horizontal boundary conditions and matching conditions read (recall that the first subscript denotes the harmonic component and the second subscript denotes

the channel label)

$$\tilde{\eta}_{n,j} = \delta_{n1}\tilde{Z}_j \cos\big(\tilde{t} - \phi_j\big), \qquad \text{at } x = L_j, \forall e_j \in E_S, \tag{S2.3a}$$

$$\tilde{B}_j \int_{-\tilde{H}_j}^{\varepsilon\tilde{\eta}_{n,j}} \tilde{u}_{n,j} \mathrm{d}\tilde{z} = \delta_{n0}\tilde{Q}_{R,j}, \qquad \text{at } x = 0, \ \ \forall e_j \in E_R, \tag{S2.3b}$$

$$\tilde{\eta}_{n,j} + \frac{\varepsilon}{2}\overline{\tilde{u}^2_{n,j}} = \tilde{\eta}_{n,k} + \frac{\varepsilon}{2}\overline{\tilde{u}^2_{n,k}}, \qquad \forall v_i \in V_I, \forall j,k \text{ s.t. } v_i \in e_j, e_k, \tag{S2.3c}$$

$$\sum_{j\in I_i} \tilde{B}_j \int_{-\tilde{H}_j}^{\varepsilon\tilde{\eta}_{n,j}} \tilde{u}_{n,j} \mathrm{d}\tilde{z} = \sum_{j\in O_i} \tilde{B}_j \int_{-\tilde{H}_j}^{\varepsilon\tilde{\eta}_{n,j}} \tilde{u}_{n,j} \mathrm{d}\tilde{z}, \quad \text{for sets } \begin{cases} I_i = \{e \in E | e = (v_q, v_i)\} \\ O_i = \{e \in E | e = (v_i, v_q)\} \end{cases}. \tag{S2.3d}$$

Here, $\tilde{Z}_j = \frac{Z_j}{N_0}$ and $\tilde{Q}_{R,j} = \frac{Q_{R,j}}{B_0 H_0 U_0}$. Equation (S2.3c) is the continuity of total pressure, which describes the momentum conservation at a junction and is derived in Section S5. Typically, the strength of density-driven flow is one order of magnitude smaller than that of the tidal current. The river discharge can be important, e.g., during the wet season or upstream near the tidal limit. Therefore, the following typical magnitudes of the above dimensionless parameters are assumed,

$$\begin{aligned} &\varepsilon \ll 1, \qquad && \widetilde{A}_{vn} = \mathcal{O}(1), \qquad && \tilde{\tilde{s}}_{fn} = \mathcal{O}(1), \\ &\Gamma = \mathcal{O}(\varepsilon), \qquad && \tilde{Z}_j = \mathcal{O}(1), \qquad && \tilde{Q}_{R,j} = \mathcal{O}(1). \end{aligned}$$

The next step is to expand dimensionless variables $\tilde{\chi}_n \in \{\tilde{u}_n, \tilde{w}_n, \tilde{\eta}_n, \widetilde{A}_{vn}, \tilde{\tilde{s}}_{fn}\}$ in power series of the small parameter ε:

$$\tilde{\chi}_n = \tilde{\chi}^0_n + \varepsilon\tilde{\chi}^1_n + \mathcal{O}\big(\varepsilon^2\big), \tag{S2.4}$$

where the superscript denotes the order of ε. Note that in the turbulence model, eddy viscosity and slip parameter depend on the state variables and hence on ε. Therefore, the constant eddy viscosities and slip parameters are written in terms of power series to match the results from the turbulence model (see Section S3 for details).

Collecting terms at different orders of ε, a system of equations at each order of ε can be obtained. The leading order system is identical to that in Chapter 2. The first order system is contained in Chapter 3 (Eqs. (3.2.12)-(3.2.14)).

S3 Turbulence model

Eqs. (S2.1)-(S2.2) contains constant eddy viscosities $\widetilde{A_{vn}}$ and slip parameters $\widetilde{s}_{f,n}$ at both the leading order and the first order. Here, it will be shown that they are computed from the space- and time-dependent turbulence model, i.e., in the main text, Eq. (3.2.8) for eddy viscosities and Eq. (3.2.9) for slip parameters. They are repeated here for clarity. The space- and time-dependent eddy viscosity is

$$A_v(x,z,t) = l^2\left|\frac{\partial u}{\partial z}\right|\left(1+\left|\frac{\partial \rho}{\partial x}\right|\frac{|\hat{u}_1|}{\omega\Delta\rho}\cos(\omega t-\alpha)\right), \tag{S3.1}$$

and the space- and time-dependent slip parameter is

$$s_f = C_{100}|u_b|. \tag{S3.2}$$

Note that the turbulence model in Chapter 2 is the leading order approximation for that in Chapter 3.

S3.1 Scaling

Using the same ordering arguments from Section S2, the dimensional leading and first order eddy viscosities and slip parameters are

$$A_v{}^0 = l^2\left|\frac{\partial u^0}{\partial z}\right|, \qquad A_v{}^1 = l^2\mathrm{sgn}\left(\frac{\partial u^0}{\partial z}\right)\frac{\partial u^1}{\partial z} + l^2\left|\frac{\partial u^0}{\partial z}\right|\left|\frac{\partial \rho}{\partial x}\right|\frac{\left|\hat{u}_1^0\right|}{\omega\Delta\rho}\cos(\omega t-\alpha),$$
$$s_f^0 = C_{100}\left|u_b^0\right|, \qquad s_f^1 = C_{100}\,\mathrm{sgn}\left(u_b^0\right)u_b^1.$$

Next, ordering is applied to the local and bottom energy dissipation. In dimensional form up to the first order, they read

$$D = \int_{-H}^{\eta} A_v\left(\frac{\partial u}{\partial z}\right)^2 \mathrm{d}z = \int_{-H}^{\eta}\left(\tau^0+\tau^1\right)\left(\frac{\partial u^0}{\partial z}+\frac{\partial u^1}{\partial z}\right)\mathrm{d}z, \tag{S3.3}$$
$$D_b = s_f u_b^2 = \left(\tau_b^0+\tau_b^1\right)\left(u_b^0+u_b^1\right), \tag{S3.4}$$

where the leading order kinematic internal and bottom stresses in this turbulence model are

$$\tau^0 = A_v{}^0\frac{\partial u^0}{\partial z} = l^2\left|\frac{\partial u^0}{\partial z}\right|\frac{\partial u^0}{\partial z}, \tag{S3.5a}$$
$$\tau_b^0 = s_f^0 u_b^0 = C_{100}\left|u_b^0\right|u_b^0. \tag{S3.5b}$$

and the first order internal and bottom stresses are

$$\tau^1 = A_v{}^1\frac{\partial u^0}{\partial z} + A_v{}^0\frac{\partial u^1}{\partial z}, \tag{S3.6a}$$
$$\tau_b^1 = s_f^1 u_b^0 + s_f^0 u_b^1. \tag{S3.6b}$$

S3.2 Harmonic decomposition of leading order internal and bottom stresses

Both the leading order kinematic internal stress and bottom stress in Eq. (S3.5) are of the following form

$$f(\boldsymbol{x},t) = \alpha|g(\boldsymbol{x},t)|g(\boldsymbol{x},t), \tag{S3.7}$$

where $\boldsymbol{x}$ is the independent variable for space and the coefficient α is required to be time independent. In this subsection, only the leading order variables are involved and hence the superscript $(\cdot)^0$ is omitted. Using the harmonic truncation, the state variable $g \in \left\{\frac{\partial u}{\partial z}, u_b\right\}$ is written as

$$g = g_0(\boldsymbol{x}) + g_1(\boldsymbol{x},t) = g_0(\boldsymbol{x}) + \frac{1}{2}\big(\hat{g}_1(\boldsymbol{x})e^{-i\omega t} + \hat{g}_1(\boldsymbol{x})^* e^{i\omega t}\big), \tag{S3.8}$$

where the subscript denotes the harmonic component, a hat implies the complex amplitude and the superscript $(\cdot)^*$ denotes the complex conjugate. Here, g_0 and g_1 are the solutions obtained using constant eddy viscosities $\check{A}_{v0,1}$ and constant slip parameters $\check{s}_{0,1}$. Then the nonlinear function f can be approximated by spectral methods such as using Fourier transform (Dronkers, 1964, Parker, 1984) or Chebyshev polynomials (Godin, 1999). Note that in this thesis, both methods are essentially the same and give identical results, the application of Chebyshev polynomials is adopted because it converges faster in the computation for constant eddy viscosities and slip parameters. The procedure is similar to that of Alebregtse and de Swart (2016). Truncate the results after M_2 yields

$$\begin{aligned} f &= \alpha|g_0|g_0 \approx f_0(\boldsymbol{x}) + f_1(\boldsymbol{x},t) \\ &= \underbrace{\frac{16\alpha}{15\pi}G\left[1 + \frac{6}{G^2}\left(\frac{1}{3}g_0^2 + \frac{1}{2}|\hat{g}_1|^2\right)\right]g_0}_{f_0} + \underbrace{\frac{16\alpha}{15\pi}G\left[1 + \frac{6}{G^2}\left(g_0^2 + \frac{1}{4}|\hat{g}_1|^2\right)\right]\mathrm{Re}\{\hat{g}_1 e^{-i\omega t}\}}_{f_1}, \end{aligned}$$

where $G = |g_0| + |\hat{g}_1|$ is the scale of g. Therefore, the M_0 (residual) and M_2 components of the local internal stress are

$$\tau_0 = \frac{16l^2}{15\pi}G_I\left[1 + \frac{6}{G_I^2}\left(\frac{1}{3}\left(\frac{\partial u_0}{\partial z}\right)^2 + \frac{1}{2}\left|\frac{\partial \hat{u}_1}{\partial z}\right|^2\right)\right]\frac{\partial u_0}{\partial z}, \tag{S3.9}$$

$$\tau_1 = \mathrm{Re}\{\hat{\tau}_1 e^{-i\omega t}\} = \mathrm{Re}\left\{\frac{16l^2}{15\pi}G_I\left[1 + \frac{6}{G_I^2}\left(\left(\frac{\partial u_0}{\partial z}\right)^2 + \frac{1}{4}\left|\frac{\partial \hat{u}_1}{\partial z}\right|^2\right)\right]\frac{\partial \hat{u}_1}{\partial z}e^{-i\omega t}\right\}, \tag{S3.10}$$

where $G_I = \left|\frac{\partial u_0}{\partial z}\right| + \left|\frac{\partial \hat{u}_1}{\partial z}\right|$ is the magnitude of the local velocity shear. Similarly, the M_0 and M_2 components of the local bottom stress are

$$\tau_{b0} = \frac{16C_{100}}{15\pi} G_b \left[1 + \frac{6}{G_b^2}\left(\frac{1}{3}u_{b0}^2 + \frac{1}{2}|\hat{u}_{b1}|^2\right)\right] u_{b0},$$
$$\tau_{b1} = \mathrm{Re}\{\hat{\tau}_{b1} e^{-i\omega t}\} = \mathrm{Re}\left\{\frac{16C_{100}}{15\pi} G_b \left[1 + \frac{6}{G_b^2}\left(u_{b0}^2 + \frac{1}{4}|\hat{u}_{b1}|^2\right)\right] \hat{u}_{b1} e^{-i\omega t}\right\},$$

where $G_b = |u_{b0}| + |\hat{u}_{b1}|$ is the magnitude of the local bottom velocity.

Next, applying harmonic truncation Eq. (S3.8) to the subtidal energy dissipation and using the results of decomposed stresses yields

$$D = \underline{(\tau_0 + \tau_1)\left(\frac{\partial u_0}{\partial z} + \frac{\partial u_1}{\partial z}\right)} = \underbrace{\tau_0 \frac{\partial u_0}{\partial z}}_{D_0} + \underbrace{\tau_1 \frac{\partial u_1}{\partial z}}_{D_1}, \tag{S3.11}$$

$$D_b = \underline{(\tau_{b0} + \tau_{b1})(u_{b0} + u_{b1})} = \underbrace{\tau_{b0} u_{b0}}_{D_{b0}} + \underbrace{\tau_{b1} u_{b1}}_{D_{b1}}. \tag{S3.12}$$

Here, the cross terms vanish due to the averaging over one tidal cycle. The subtidal energy dissipation due to both internal stress and bottom stress contain two parts: the contribution of M_0 river flow (D_0 and D_{b0}) and M_2 tidal flow (D_1 and D_{b1}). These dissipation contributions are assumed to be the same as when using constant friction parameters $\check{A}_{v0,1}$ and $\check{s}_{0,1}$, i.e.,

$$D_n = \check{D}_n \quad \text{and} \quad D_{bn} = \check{D}_{bn}, \tag{S3.13}$$

where $\check{D}_n$ and $\check{D}_{bn}$ are given in Eq. (2.2.5) and Eq. (2.2.11). These criteria give the expressions for constant friction parameters at the leading order, the results are

$$\check{A}_{v0} = \frac{\underline{\tau_0 \frac{\partial u_0}{\partial z}}}{\underline{\left(\frac{\partial u_0}{\partial z}\right)^2}}, \qquad \check{A}_{v1} = \frac{\mathrm{Re}\left\{\underline{\hat{\tau}_1^* \frac{\partial \hat{u}_1}{\partial z}}\right\}}{\underline{\left|\frac{\partial \hat{u}_1}{\partial z}\right|^2}},$$

$$\check{s}_{f0} = \frac{\underline{\tau_{b0} u_{b0}}}{\underline{u_{b0}^2}}, \qquad \check{s}_{f1} = \frac{\mathrm{Re}\left\{\underline{\hat{\tau}_{b1}^* \hat{u}_{b1}}\right\}}{\underline{|\hat{u}_{b1}^2|}}.$$

S3.3 First order eddy viscosity and slip parameter

Applying ordering to the mean energy dissipation due to constant eddy viscosity and retaining terms up to the first order give

$$\begin{aligned}\check{D}_n &= \check{A}_{vn}\underline{\left(\frac{\partial u_n}{\partial z}\right)^2} = \left(\check{A}_{vn}^{\,0} + \check{A}_{vn}^{\,1}\right)\left[\underline{\left(\frac{\partial u_n^0}{\partial z}\right)^2} + 2\underline{\frac{\partial u_n^0}{\partial z}\frac{\partial u_n^1}{\partial z}}\right] \\ &= \underbrace{\check{A}_{vn}^{\,0}\underline{\left(\frac{\partial u_n^0}{\partial z}\right)^2}}_{\check{D}_n^0} + \underbrace{2\check{A}_{vn}^{\,0}\underline{\frac{\partial u_n^0}{\partial z}\frac{\partial u_n^1}{\partial z}} + \check{A}_{vn}^{\,1}\underline{\left(\frac{\partial u_n^0}{\partial z}\right)^2}}_{\check{D}_n^1}.\end{aligned} \tag{S3.14}$$

The mean energy dissipation at each order due to each harmonic component should be the same using either the constant eddy viscosity or the space- and time-dependent turbulence model.

Note that the actual constant eddy viscosity and slip parameter acting on the first order flow are the leading order constant eddy viscosity and slip parameter. The first order constant eddy viscosity and slip parameter act on the leading order flow and therefore they are regarded as forcing. The values for first order constant eddy viscosity and slip parameter are computed by equating the first order mean energy dissipation yielded from the turbulence model (Eq. (S3.3) and Eq. (S3.4)) with the mean dissipation yielded by the constant eddy viscosity and slip parameter. In the space- and time-dependent turbulence model, the mean energy dissipation at first order due to the subtidal component is

$$\underline{D_0^1} = \underline{\tau^0\frac{\partial u^1}{\partial z}} + \underline{\tau^1\frac{\partial u^0}{\partial z}},$$

which is required to be the same as $\check{D}_n^1$ (Eq. (S3.14)), i.e.,

$$\check{A}_{v0}^{\,1} = \frac{\underline{D_0^1} - 2\check{A}_{v0}^{\,0}\underline{\frac{\partial u_0^0}{\partial z}\frac{\partial u_0^1}{\partial z}}}{\underline{\left(\frac{\partial u_0^0}{\partial z}\right)^2}}. \tag{S3.15}$$

Similarly, the constant value for the first order slip parameter is

$$\check{s}_{f0}^1 = \frac{\underline{D_{b0}^1} - 2\check{s}_{f0}^0\underline{u_{b0}^0 u_{b0}^1}}{\underline{\left(u_{b0}^0\right)^2}}.$$

Here, u_0^1 contains all first order subtidal flows, including the one forced by $\check{A}_{v0}^{\,1}$ and $\check{s}_{f0}^1$. The focus of this study is the subtidal water transport up to the first order, and therefore only the subtidal component is considered at the first order dissipation. The value of $\check{A}_{v0}^{\,1}$ and $\check{s}_{f0}^1$ are computed iteratively. Starting with

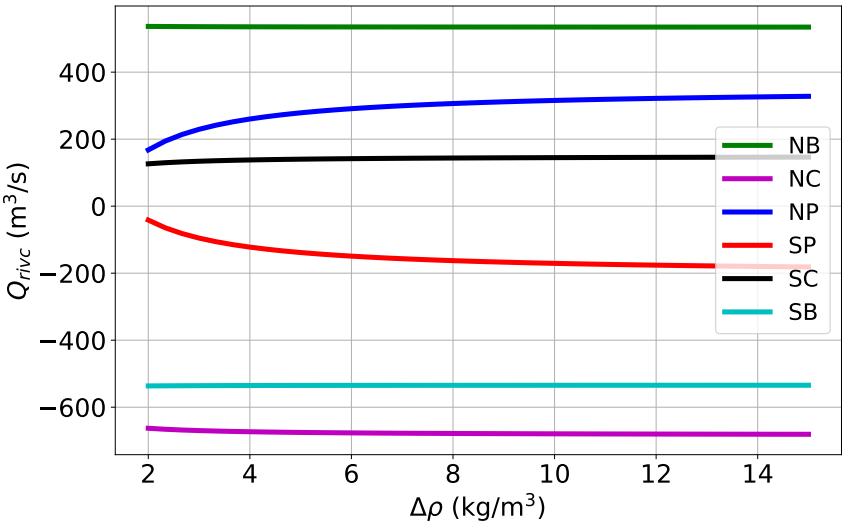

Figure S1: Sensitivity of the transport due to the first order correction to river flow to vertical density difference.

an initial guess for $\check{A}_{v0}^{\ 1}$ and $\check{s}_{f0}^{1}$, the solution forced by $\check{A}_{v0}^{\ 1}$ and $\check{s}_{f0}^{1}$ is computed and used to update $\check{A}_{v0}^{\ 1}$ and $\check{s}_{f0}^{1}$. This process is repeated until convergence (changes in $\check{A}_{v0}^{\ 1}$ and $\check{s}_{f0}^{1}$ are less than 10^{-5}).

Sensitivity of model results to the vertical density difference

From the first order subtidal momentum balance Eq. (3.2.12), it can be seen that the first order eddy viscosity only acts on the leading order river flow. This contribution is denoted by the first order correction to the river flow because it is driven by the leading order river flow. The vertical density stratification affects the value of the first order eddy viscosity. Therefore, the first order correction to the river flow is the only contribution that implicitly depends on the vertical density difference $\Delta\rho$, which might be different during the spring-neap cycle, under large channel deepening or sea level rise. It should be noted that the first order eddy viscosity is computed using the energy criterion (Eq. (S3.15)), meaning that its value is also affected by other first order subtidal flows.

Fig. S1 shows the sensitivity of the water transport due to this contribution to the vertical density difference for the reference case. The model results are therefore not sensitive to this parameter.

S4 Solutions to water motion

S4.1 Leading order water motion

Solutions for river flow

The river flow is governed by Eqs. (2.2.2), assuming $n = 0$. To obtain the solutions, integrate the momentum equation for river flow from some depth $z' = z$ to the linearised free surface $z' = 0$ and apply the boundary condition yielding

$$0 = gz\frac{\partial \eta_0}{\partial x} - \check{A}_{v0}\frac{\partial u_0}{\partial z}. \tag{S4.1}$$

Integrate again from the bottom $z' = -H$ to some depth z, which gives

$$u_0 = \frac{\left(z^2 - H^2\right)}{2\check{A}_{v0}} g\frac{\partial \eta_0}{\partial x} + u_0|_{z=-H}\,. \tag{S4.2}$$

The slip condition at the bottom implies

$$u_0|_{z=-H} = \frac{\check{A}_{v0}}{\check{s}_{f0}}\left.\frac{\partial u_0}{\partial z}\right|_{z=-H} = -\frac{gH}{\check{s}_{f0}}\frac{\partial \eta_0}{\partial x}. \tag{S4.3}$$

Hence,

$$u_0 = \frac{gH^2}{\check{A}_{v0}}\left[\frac{\left(\frac{z}{H}\right)^2 - 1}{2} - \frac{\check{A}_{v0}}{H\check{s}_{f0}}\right]\frac{\partial \eta_0}{\partial x}. \tag{S4.4}$$

Integration of the continuity equation and application of the boundary conditions at the bottom and surface gives Eq. (2.2.15) in the main text. Application of boundary condition at the river head implies

$$\frac{\partial \eta_0}{\partial x} = -\frac{Q\check{A}_{v0}}{gB(x)H^3}\frac{1}{\frac{1}{3} + \frac{\check{A}_{v0}}{H\check{s}_{f0}}}. \tag{S4.5}$$

Eqs. (S4.4)-(S4.5) are Eqs. (2.2.16) in the main text. Note that the vertical velocity is everywhere zero.

Solutions for tidal flow

Tidal flow can be solved by substituting non-transient periodic trial solutions

$$(u_1, w_1, \eta_1) = \mathrm{Re}\left\{(\hat{u}_1, \hat{w}_1, \hat{\eta}_1)\, e^{-i\omega t}\right\} \tag{S4.6}$$

into the governing equations and boundary conditions (Eqs. (2.2.2)-(2.2.4)) of the main text for $n = 1$:

$$-i\omega\hat{u}_1 = -g\frac{\mathrm{d}\hat{\eta}_1}{\mathrm{d}x} + \check{A}_{v1}\frac{\partial^2\hat{u}_1}{\partial z^2}, \tag{S4.7a}$$

$$0 = \frac{\partial\hat{u}_1}{\partial x} + \frac{\partial\hat{w}_1}{\partial z} + \frac{1}{L_b}\hat{u}_1, \tag{S4.7b}$$

$$\check{A}_{v1}\frac{\partial\hat{u}_1}{\partial z} = 0, \qquad \hat{w}_1 = -i\omega\hat{\eta}_1 \quad \text{at} \quad z = 0, \tag{S4.7c}$$

$$\check{A}_{v1}\frac{\partial\hat{u}_1}{\partial z} = \check{s}_{f1}\hat{u}_1, \quad \hat{w}_1 = 0 \qquad \text{at} \quad z = -H. \tag{S4.7d}$$

The general solution of Eq. (S4.7a) is

$$\hat{u}_1(x,z) = A_1(x)e^{\gamma z} + A_2(x)e^{-\gamma z} - \frac{ig}{\omega}\frac{\mathrm{d}\hat{\eta}_1}{\mathrm{d}x}, \tag{S4.8}$$

where $\gamma = \sqrt{-\frac{i\omega}{\check{A}_{v1}}}$. The first boundary condition in Eq. (S4.7c) gives

$$\hat{u}_1(x,z) = A(x)\cosh(\gamma z) - \frac{ig}{\omega}\frac{\mathrm{d}\hat{\eta}_1}{\mathrm{d}x}. \tag{S4.9}$$

Finally, apply the partial slip condition at the bottom $z = -H$ to obtain

$$\hat{u}_1(x,z) = \frac{ig}{\omega}\left[\beta\cosh(\gamma z) - 1\right]\frac{\mathrm{d}\hat{\eta}_1}{\mathrm{d}x}, \tag{S4.10}$$

where β is defined in the main text. Next, substitute of Eq. (S4.10) into the continuity (S4.7b), integrate over depth and use of the boundary condition $\hat{w}_1 = -i\omega\hat{\eta}_1$ at $z = 0$ yields

$$\hat{w}_1(x,z) = -\frac{ig}{\omega}\left[\frac{\beta}{\gamma}\sinh(\gamma z) - z\right]\left(\frac{\mathrm{d}^2\hat{\eta}_1}{\mathrm{d}x^2} + \frac{1}{L_b}\frac{\mathrm{d}\hat{\eta}_1}{\mathrm{d}x}\right) - i\omega\hat{\eta}_1. \tag{S4.11}$$

The boundary condition at the bottom ($w_1 = 0$ at $z = -H$) implies that the surface amplitude should obey the differential equation

$$\frac{g}{\omega}\left[\frac{\beta}{\gamma}\sinh(\gamma H) - H\right]\left(\frac{\mathrm{d}^2\hat{\eta}_1}{\mathrm{d}x^2} + \frac{1}{L_b}\frac{\mathrm{d}\hat{\eta}_1}{\mathrm{d}x}\right) - \omega\hat{\eta}_1 = 0. \tag{S4.12}$$

Its general solution is

$$\hat{\eta}_1 = C_1e^{k_1x} + C_2e^{k_2x}, \tag{S4.13}$$

where

$$k_{1,2} = -\frac{1}{2L_b} \pm \sqrt{\left(\frac{1}{2L_b}\right)^2 + \frac{\gamma\omega^2}{g[\beta\sinh(\gamma H) - \gamma H]}} \tag{S4.14}$$

are the two complex wave numbers. This expression is equivalent to Eq. (2.2.18c) by factoring out $-\frac{1}{2L_b}$ in the complex wave numbers, which describes the exponential decay of the tidal wave due to the variation of channel width.

S4.2 First order water motion

The solutions to the dimensional first order subtidal system (Eq. (3.2.12)-(3.2.15)) are constructed per forcing term and then added to obtain the total solution. The solutions for each forcing term consist of a particular solution in response to the forcing and a homogeneous solution. In single channels, the homogeneous solution is such that the net discharge of each term is zero (except for the river-discharge term, where the net discharge should equal the prescribed discharge). Such single-channel solutions can be found in Ianniello (1977, 1979) and the user-manual (semi-analytical package, section 4) of iFlow (SI of Dijkstra et al., 2017a). In a network, the homogeneous solution is such that the matching conditions are satisfied, which may lead to a net water transport contribution. The solutions below therefore consist of a term that scales with this net water transport (indicated Q_{forcing}) (blue terms, net water flow) plus a term that is identical to the single-channel solution (red terms, exchange flow).

Density-driven flow

$$u_{\text{baroc}} = f_h(z)\frac{\mathrm{d}}{\mathrm{d}x}\eta_{\text{baroc}} - \frac{gH^3\beta_s}{2\check{A}_{v0}^{\,0}}\left[\frac{1}{3}\left(\left(\frac{z}{H}\right)^3+1\right)+r^0\right]\frac{\mathrm{d}s}{\mathrm{d}x}, \tag{S4.15a}$$

$$\frac{\mathrm{d}}{\mathrm{d}x}\eta_{\text{baroc}} = -\frac{\check{A}_{v0}^{\,0}}{gH^3\left(\frac{1}{3}+r^0\right)}\left[\frac{Q_{\text{baroc}}}{B(x)}+\frac{gH^4\beta_s}{2\check{A}_{v0}^{\,0}}\left(\frac{1}{4}+r^0\right)\frac{\mathrm{d}s}{\mathrm{d}x}\right], \tag{S4.15b}$$

where

$$f_h(z) = \frac{gH^2}{\check{A}_{v0}^{\,0}}\left[\frac{1}{2}\left(\left(\frac{z}{H}\right)^2-1\right)-r^0\right], \tag{S4.16}$$

and

$$r^0 = \frac{\check{A}_{v0}}{H\check{s}_{f0}}.$$

Combining Eq. (S4.15a) and Eq. (S4.15b) yields

$$\begin{aligned} u_{\text{baroc}} = &\frac{Q_{\text{baroc}}}{B(x)H(3r^0+1)}\left(\frac{3}{2}+3r^0-\frac{3}{2}\left(\frac{z}{H}\right)^2\right) \\ &+\frac{gH^3\beta_s}{48\check{A}_{v0}^{\,0}(3r^0+1)}\left[1+6r^0-9(1+4r^0)\left(\frac{z}{H}\right)^2-8(1+3r^0)\left(\frac{z}{H}\right)^3\right]\frac{ds}{dx}. \end{aligned} \tag{S4.17}$$

In the limit of no-slip condition ($r^0 = 0$, see Eq. (3.4.2)), this solution is the same as that in Hansen and Rattray (1965), MacCready (2004).

Advection Solutions for the subtidal flow due to leading order advection are expressed in terms of the sum of the homogeneous and the particular solution

$$u_{\mathrm{adv}} = f_h(z)\frac{\mathrm{d}}{\mathrm{d}x}\eta_{\mathrm{adv}} + u_{p,\mathrm{adv}}, \tag{S4.18a}$$

$$\frac{\mathrm{d}}{\mathrm{d}x}\eta_{\mathrm{adv}} = -\frac{\check{A}_{v0}^{\,0}}{gH^3\left(\frac{1}{3}+r^0\right)}\left[\frac{Q_{\mathrm{adv}}}{B(x)} - \int_{-H}^{0} u_{p,\mathrm{adv}}\mathrm{d}z\right]. \tag{S4.18b}$$

The particular solution is given by

$$u_{p,\mathrm{adv}} = -\frac{H}{\check{A}_{v0}^{\,0}}\left(\frac{z}{H}+1+r^0\right)\int_{-H}^{0} F_{\mathrm{adv}}\mathrm{d}z + \frac{1}{\check{A}_{v0}^{\,0}}\left(z\int_{-H}^{z} F_{\mathrm{adv}}\mathrm{d}z' - \int_{-H}^{z} F_{\mathrm{adv}}z'\mathrm{d}z'\right). \tag{S4.19}$$

Stokes transport and its return flow

$$u_{\mathrm{Stokes}} = f_h(z)\frac{\mathrm{d}}{\mathrm{d}x}\eta_{\mathrm{Stokes}}, \tag{S4.20a}$$

$$\frac{\mathrm{d}}{\mathrm{d}x}\eta_{\mathrm{Stokes}} = -\frac{\check{A}_{v0}^{\,0}}{gH^3\left(\frac{1}{3}+r^0\right)}\left[\frac{Q_{\mathrm{Stokes}}}{B(x)} - \left\langle \eta_1^0 u_1^0\right\rangle|_{z=0}\right]. \tag{S4.20b}$$

Velocity-depth asymmetry

$$u_{\mathrm{vda}} = f_h(z)\frac{\mathrm{d}}{\mathrm{d}x}\eta_{\mathrm{vda}} - \left(\frac{z}{H}+1+r^0\right)HF_{\mathrm{vda}}, \tag{S4.21a}$$

$$\frac{\mathrm{d}}{\mathrm{d}x}\eta_{\mathrm{vda}} = -\frac{\check{A}_{v0}^{\,0}}{gH^3\left(\frac{1}{3}+r^0\right)}\left[\frac{Q_{\mathrm{vda}}}{B(x)} + \left(\frac{1}{2}+r\right)H^2F_{\mathrm{vda}}\right]. \tag{S4.21b}$$

Continuous dynamic pressure

$$u_{\mathrm{dp}} = f_h(z)\frac{\mathrm{d}}{\mathrm{d}x}\eta_{\mathrm{dp}}, \tag{S4.22a}$$

$$\frac{\mathrm{d}}{\mathrm{d}x}\eta_{\mathrm{dp}} = -\frac{\check{A}_{v0}^{\,0}}{gH^3\left(\frac{1}{3}+r^0\right)}\frac{Q_{\mathrm{dp}}}{B(x)}. \tag{S4.22b}$$

Note this component has no particular solution since this does not appear in a single channel and has a forcing at the junction only.

First order correction to the river flow (rivc)

$$u_{\mathrm{rivc}} = f_h(z)\frac{\mathrm{d}}{\mathrm{d}x}\eta_{\mathrm{rivc}} - \frac{\check{A}_{v0}^{\,1}}{\check{A}_{v0}^{\,0}}u_0^0 + \left(\frac{\check{A}_{v0}^{\,1}}{\check{A}_{v0}^{\,0}} - \frac{\check{s}_{f0}^1}{\check{s}_{f0}^0}\right)u_0^0|_{z=-H}, \tag{S4.23a}$$

$$\frac{\mathrm{d}}{\mathrm{d}x}\eta_{\mathrm{rivc}} = -\frac{\check{A}_{v0}^{\,0}}{gH^3\left(\frac{1}{3}+r^0\right)}\left[\frac{Q_{\mathrm{rivc}}}{B(x)} + \frac{\check{A}_{v0}^{\,1}}{\check{A}_{v0}^{\,0}}\frac{Q_0}{B(x)} + H\left(\frac{\check{A}_{v0}^{\,1}}{\check{A}_{v0}^{\,0}} - \frac{\check{s}_{f0}^1}{\check{s}_{f0}^0}\right)u_0^0|_{z=-H}\right] \tag{S4.23b}$$

Note that this contribution does not appear in Dijkstra et al. (2017a) due to the different turbulence models. This solution is obtained in the identical way as the solution procedure for the contributions by advection and velocity-depth asymmetry.

S5 Derivation of the continuity of dynamic pressure

In this thesis, channels are connected based on conservation laws. Requiring conservation of mass is generally valid. The focus here is mainly on the other channel matching condition, the continuity of dynamic pressure, which will be derived in this section.

At junctions, the horizontal length scale is much smaller than the tidal wavelength scale. A reasonable estimate for the horizontal length scale is the scale for the channel width (Bolla Pittaluga et al., 2015, Redolfi et al., 2016, Ragno et al., 2020), which is a few kilometres. Using the following representative scales at junctions

$$\begin{aligned}
&\omega = 10^{-4}\,\mathrm{s}^{-1}, && L_0 = 10^{3}\,\mathrm{m}, && H_0 = 10\,\mathrm{m}, && N_0 = 1\,\mathrm{m},\\
&U_0 = 1\,\mathrm{m\,s}^{-1}, && W_0 = 10^{-4}\,\mathrm{m\,s}^{-1}, && A_v = 10^{-2}\,\mathrm{m}^2\,\mathrm{s}^{-1}, && A_h = 10\,\mathrm{m}^2\,\mathrm{s}^{-1},\\
&S_x = 10^{-3}\,\mathrm{psu\,m}^{-1},
\end{aligned}$$

results in the scaled horizontal momentum equation

$$\begin{aligned}
\underbrace{\omega U_0 \frac{\partial \tilde{u}}{\partial \tilde{t}}}_{10^{-4}} + \underbrace{\frac{U_0^2}{L_0}\tilde{u}\frac{\partial \tilde{u}}{\partial \tilde{x}}}_{10^{-3}} + \underbrace{\frac{W_0 U_0}{H_0}\tilde{w}\frac{\partial \tilde{u}}{\partial \tilde{z}}}_{10^{-5}} &= \underbrace{-\frac{gN_0}{L_0}\frac{\partial \tilde{\eta}}{\partial \tilde{x}}}_{10^{-2}} + \underbrace{g\beta_s H_0 S_x \frac{\widetilde{\mathrm{d}s}}{\mathrm{d}x}\tilde{z}}_{10^{-5}}\\
&\quad + \underbrace{\frac{A_v U_0}{H_0^2}\frac{\partial^2 \tilde{u}}{\partial \tilde{z}^2}}_{10^{-4}} + \underbrace{\frac{A_h U_0}{L_0^2}\frac{\partial^2 \tilde{u}}{\partial \tilde{x}^2}}_{10^{-5}},
\end{aligned} \tag{S5.1}$$

where the values in the underbrace have the unit of acceleration and A_h is the horizontal eddy viscosity. Here, horizontal dispersion is retained as it can be important over a short length scale, while the Coriolis term is less important and therefore not shown here. The most important contribution to the momentum balance is the pressure gradient due to surface elevation. For this reason, many studies only require the consistency of water level at junctions (Bolla Pittaluga et al., 2015, Redolfi et al., 2016). The second most important term is the advective acceleration due to horizontal velocity. The momentum balance, with the two most important terms, reads

$$\frac{\partial}{\partial x}\left(g\eta + \frac{1}{2}u^2\right) = 0. \tag{S5.2}$$

This implies that the quantity in the parenthesis, the dynamic pressure[1], is constant for every depth. To obtain a matching condition, dynamics pressure

[1]In this thesis, the dynamics pressure may refer to the total pressure that contains a static pressure and a dynamic pressure. As the static pressure is continuous by construction, the continuous total pressure degenerates to the continuous dynamic pressure.

needs to be averaged over the total water depth $H + \eta$. Since the magnitude of the free surface elevation η is one order smaller than that of the mean water depth H, it is neglected when performing the depth-integration. Therefore, the matching condition can be obtained by averaging the depth-dependent dynamics pressure over the mean water depth. Consequently, the depth-averaged dynamic pressure

$$g\eta + \frac{1}{2}\overline{u^2}$$

is continuous at junctions.

One may already recognise that the continuity of dynamic pressure resembles the Bernoulli's equation, the applicability of which, is in general limited. Up to the order under consideration, the flow at one junction can be regarded as barotropic, steady, and inviscid. The application of the Bernoulli's equation is therefore valid. However, continuous dynamic pressure should not be interpreted exactly as the Bernoulli's equation because the Bernoulli's equation is constant along any streamline, which is not properly defined at junctions in this study. Nevertheless, it can be seen as energy conservation assuming no frictional energy losses at the small scale of the junction. The head loss due to kinetic energy dissipation can be accounted for using the parameter μ as in Eq. 7a, which is derived in the Appendix of van de Kreeke (1988).

Generally, the sharpest along-channel salinity gradient may occur near a junction, which causes the baroclinic pressure gradient force larger than estimated in Eq. (S5.1). With this additional term, depth-averaged Eq. (S5.2) reads

$$\frac{\partial}{\partial x}\left(g\eta + \frac{1}{2}\overline{u^2} - g\beta_s s\right) = 0 \implies g\eta + \frac{1}{2}\overline{u^2} - g\beta_s s = \text{constant}.$$

Since it has been already assumed that the vertically well-mixed salinity s is the same for all channels at one junction, $g\beta_s s$ is already constant at a junction and the same matching condition applies.

S6 Solution procedure

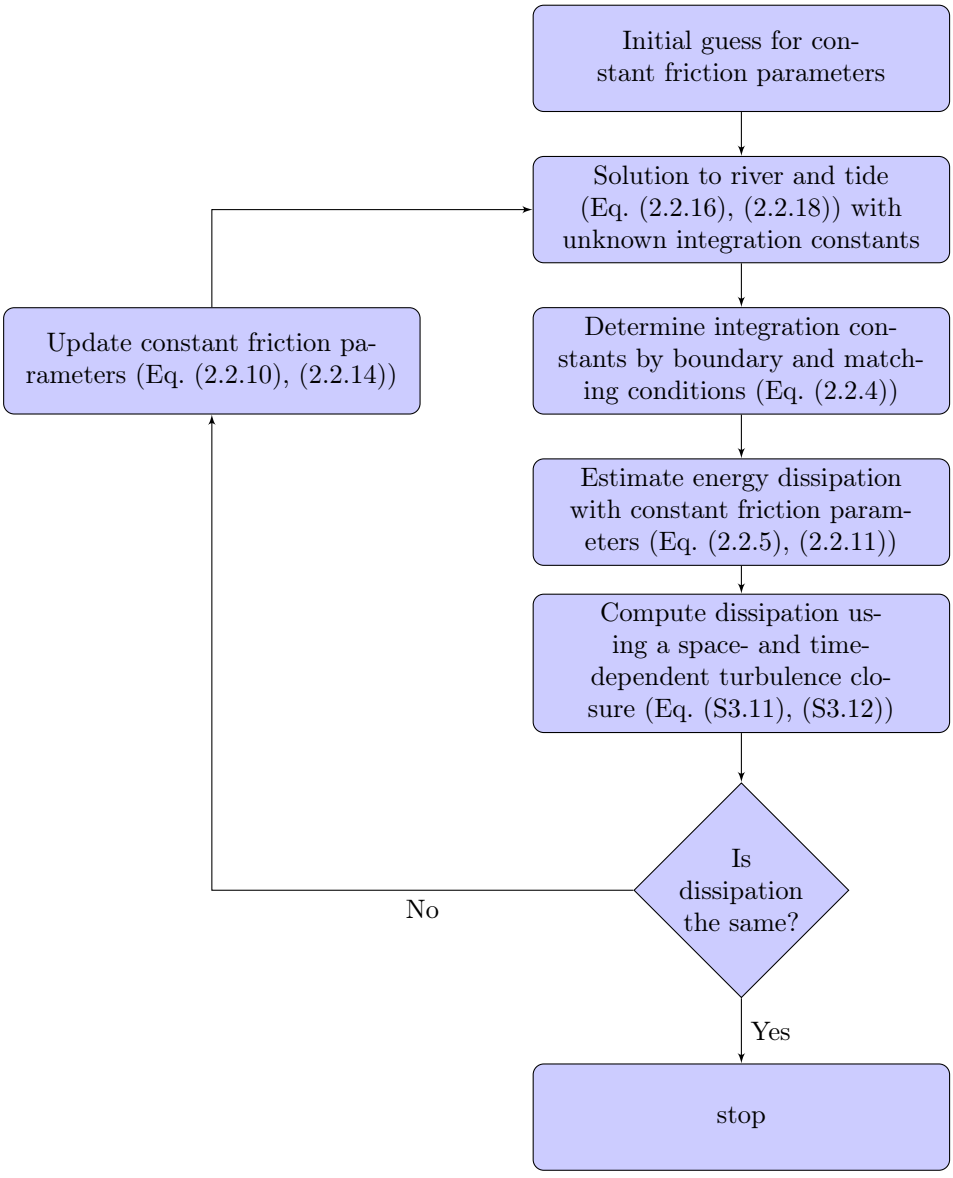

S7 A network perspective decomposition of net sediment transport

Here, it will be shown that for every junction, the net sediment transport in any channel downstream of a junction can be attributed to two processes at the junction: the division of the sediment flux from the upstream channel and the local exchange of sediment among the downstream channels. The starting point is the sediment matching condition (Eqs. (4.2.4)), i.e., the expression for $\bar{c}$ in channel 1 and channel 2, applied at the junction. Applying Eq. (4.3.3) to channel 1 and channel 2, with seaward boundary condition $f(L_j) = f_{j,\mathrm{sea}}$ (here and below, $j = 1, 2$), the value of the availability at the junction $x = 0$ is

$$f(0) = \underbrace{\exp\left(-\int_L^0 \frac{T}{F}\,\mathrm{d}x'\right)}_{\chi_A}\left(f_{\mathrm{sea}} + \mathcal{F}\underbrace{\int_L^0 \frac{1}{BF}\exp\left(\int_L^{x'}\frac{T}{F}\,\mathrm{d}x''\right)\mathrm{d}x'}_{\chi_B}\right), \tag{S7.1}$$

with constant χ_A and χ_B. Using Eq. (S7.1), the matching conditions for a three-channel system as in Fig. 4.1 read

$$\mathcal{F}_{\mathrm{river}} = \underbrace{\frac{f_1(0) - \chi_{A_1} f_{1,\mathrm{sea}}}{\chi_{A_1}\chi_{B_1}}}_{\mathcal{F}_1} + \underbrace{\frac{f_2(0) - \chi_{A_2} f_{2,\mathrm{sea}}}{\chi_{A_2}\chi_{B_2}}}_{\mathcal{F}_2}, \tag{S7.2}$$

$$\frac{\hat{C}_1(0)\, f_1(0)}{H_1} = \frac{\hat{C}_2(0)\, f_2(0)}{H_2}. \tag{S7.3}$$

The matching conditions therefore determine the values of $f_1(0)$ and $f_2(0)$ at the junction, provided that the water motion is fully determined, i.e., integrating factors $\chi_{A_{1,2}}$, integration constants $\chi_{B_{1,2}}$, and the carrying capacity $\hat{C}_{1,2}(0)$ are all known. With the solutions for $f_1(0)$ and $f_2(0)$ in terms of these constants, the net sediment transport in channel 1 and channel 2 can be written in the form of

$$\mathcal{F}_{1,2} = k_{1,2}\,\mathcal{F}_{\mathrm{river}} + m_{1,2},$$

where

$$k_1 = \frac{1}{1+\frac{\kappa_1}{\kappa_2}}, \quad k_2 = \frac{1}{1+\frac{\kappa_2}{\kappa_1}}, \quad m_1 = \frac{\frac{\mu_2 f_{2,\mathrm{sea}}}{\kappa_2} - \frac{\mu_1 f_{1,\mathrm{sea}}}{\kappa_2}}{1+\frac{\kappa_1}{\kappa_2}}, \quad m_2 = \frac{\frac{\mu_1 f_{1,\mathrm{sea}}}{\kappa_1} - \frac{\mu_2 f_{2,\mathrm{sea}}}{\kappa_1}}{1+\frac{\kappa_2}{\kappa_1}},$$

with

$$\mu = \frac{\hat{C}(0)}{H}\chi_A \quad \text{and} \quad \kappa = \mu\,\chi_B,$$

such that

$$k_1 + k_2 = 1 \quad \text{and} \quad m_1 + m_2 = 0.$$

Here, k_1 and k_2 are the ratios describing the fraction of upstream sediment flux allocated into channel 1 and channel 2 (division) and $|m_{1,2}|$ is the sediment mass exchange at the junction. These two processes do not explicitly depend on each other but on the transport capacities T and F of all the downstream channels and the depth and carrying capacity locally at the junction. The exchange of sediment additionally depends on all the prescribed concentrations at the sea. Therefore, the net sediment transport and its distribution are determined by the entire system. In addition, these two processes are independent of the upstream sediment flux $\mathcal{F}_{\text{river}}$ and hence they are the properties of the network system. The sediment concentration at the sea affects only the sediment exchange and has no influence on the division of upstream sediment flux. Hence, the separation of net sediment transport into the division and exchange processes might be a better representation for describing the sediment division than using the ratio $\mathcal{F}_1/\mathcal{F}_2$ or asymmetry index $(\mathcal{F}_1 - \mathcal{F}_2)/(\mathcal{F}_1 + \mathcal{F}_2)$. Subsequently, whether sediment overspill can be observed or not is determined by the balance between the division of upstream flux and sediment exchange at the junction.

S8 Figures

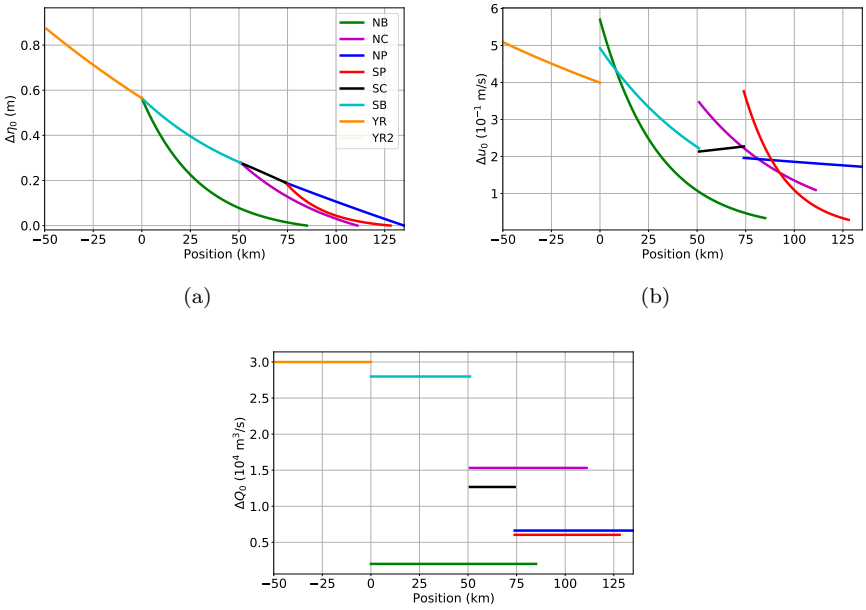

(a) (b)

(c)

Figure S2: a. Difference between elevation due to river flow during the wet and the dry season versus position in the network. b. As a, but for depth-averaged river velocity. c. As a, but for river water transport.

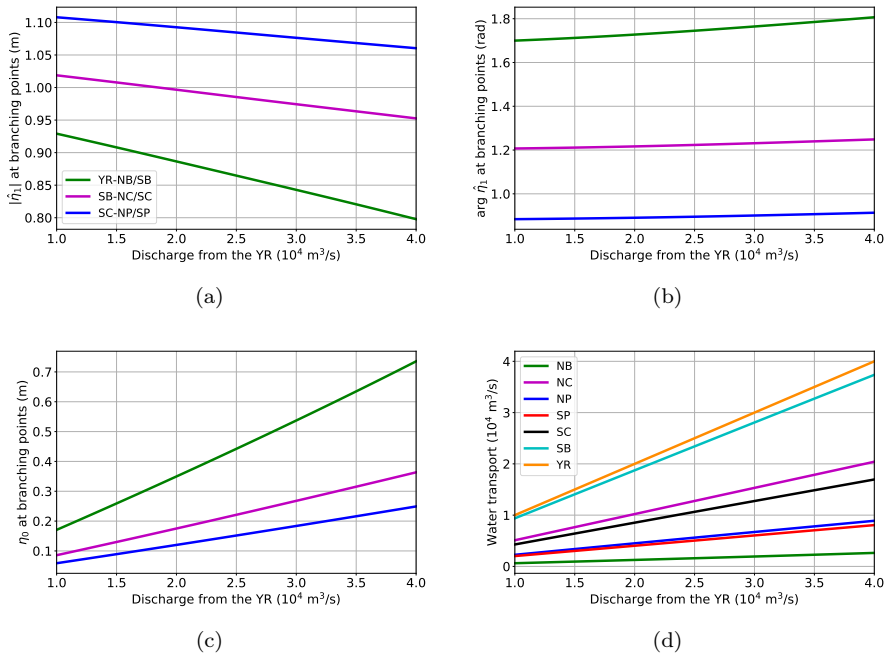

Figure S3: a. Sensitivity of tidal elevation amplitudes at the three branching points to the prescribed river discharge from the Yangtze River (YR). b. As a, but for the tidal elevation phases. c. As a, but for the elevation due to river. d. As a, but for the river water transport in each channel.

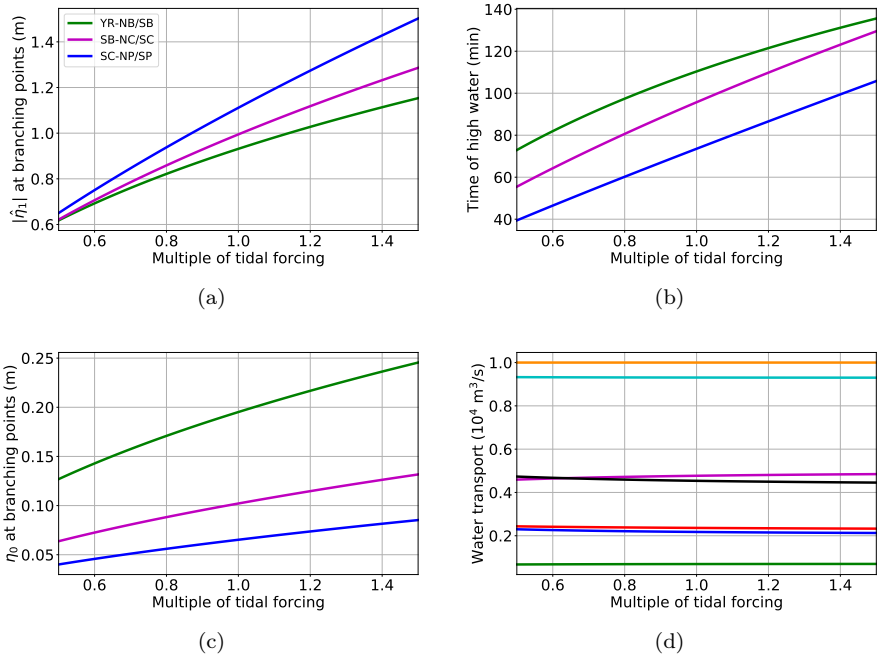

Figure S4: As Fig. S3 in this document, but for the sensitivity of these variables to tidal forcing.

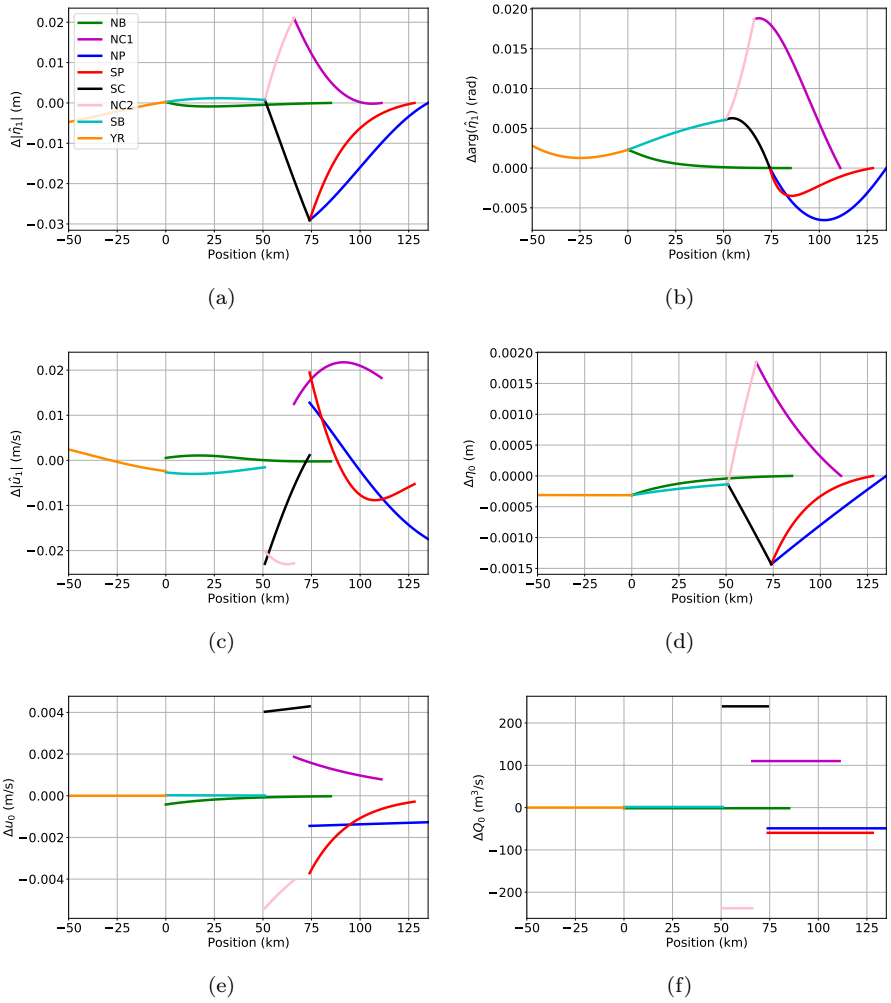

Figure S5: a-c. As Fig. 2.7 a-c in the main text, but for the difference between with and without the shortcut channel. d. As a, but for the surface elevation due to the river flow. e. As a, but for the river flow velocity. f. As a, but for the river water transport.

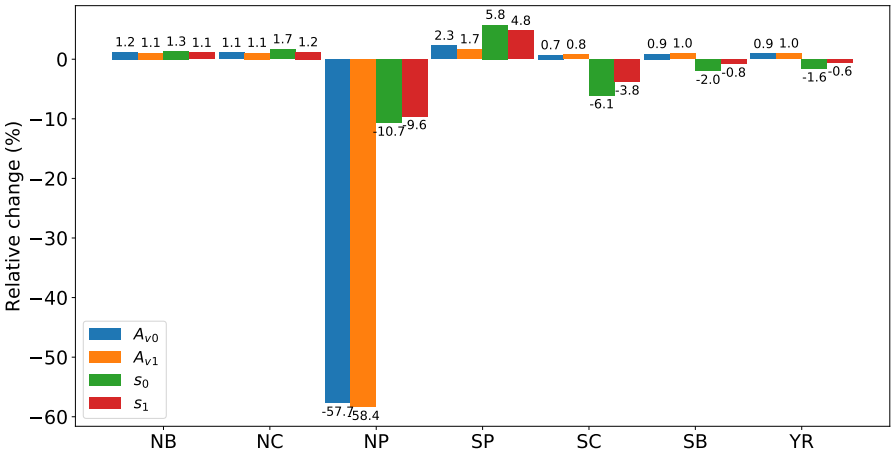

Figure S6: As Fig. 2.6 in the main text, but for the relative changes in friction parameters before the DWP with respect to the reference case.

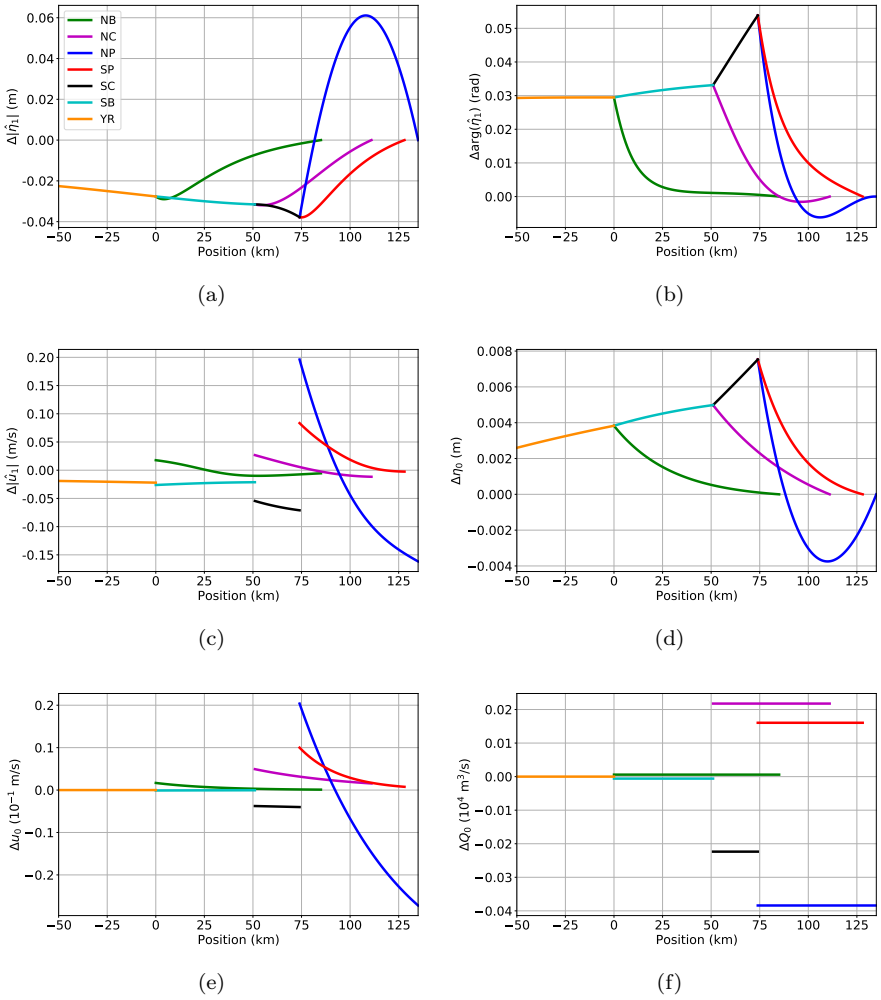

Figure S7: As Fig. S5, but for the difference between variables after and prior to the DWP.

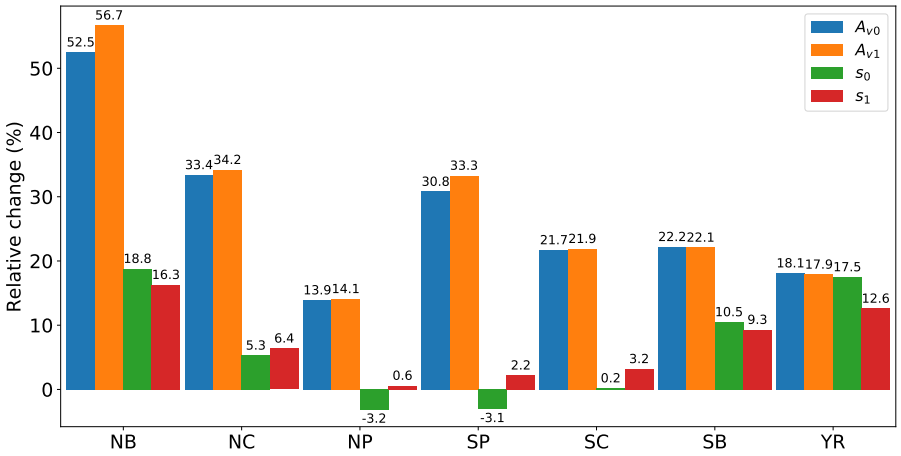

Figure S8: As Fig. S6 in this document, but for the relative changes in friction parameters after 2 m sea level rise with respect to the reference case.

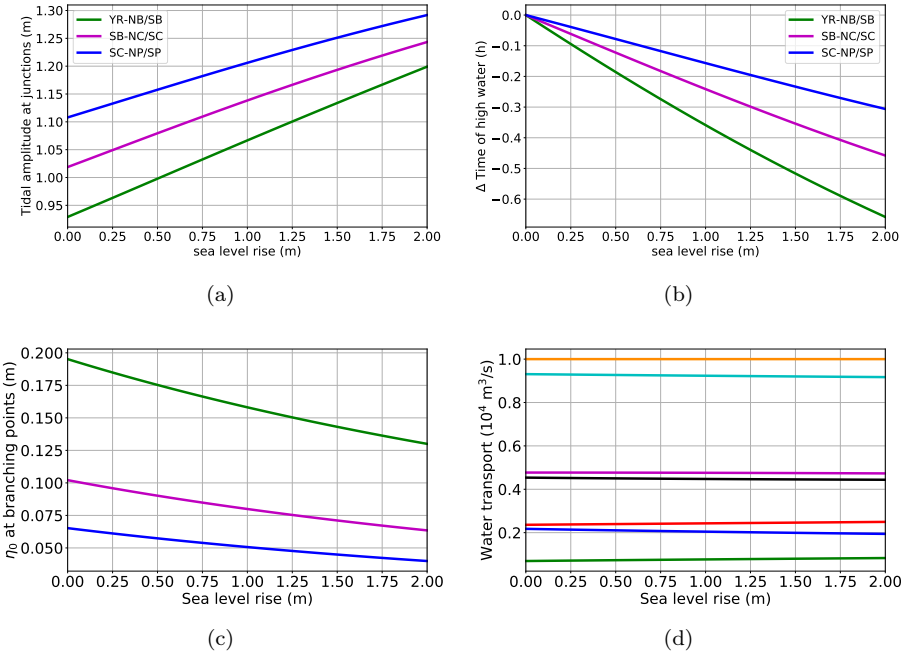

Figure S9: As Fig. S3 in this document, but for the sensitivity of these variables to sea level rise.

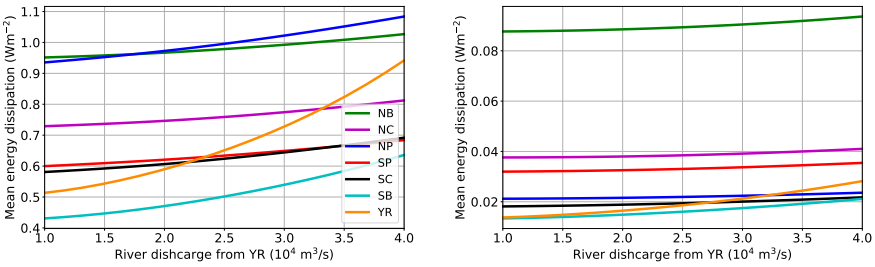

(a) bottom stress (b) internal stress

Figure S10: Sensitivity of mean energy dissipation due to (a) bottom stress and (b) internal stress in each channel to river discharge.

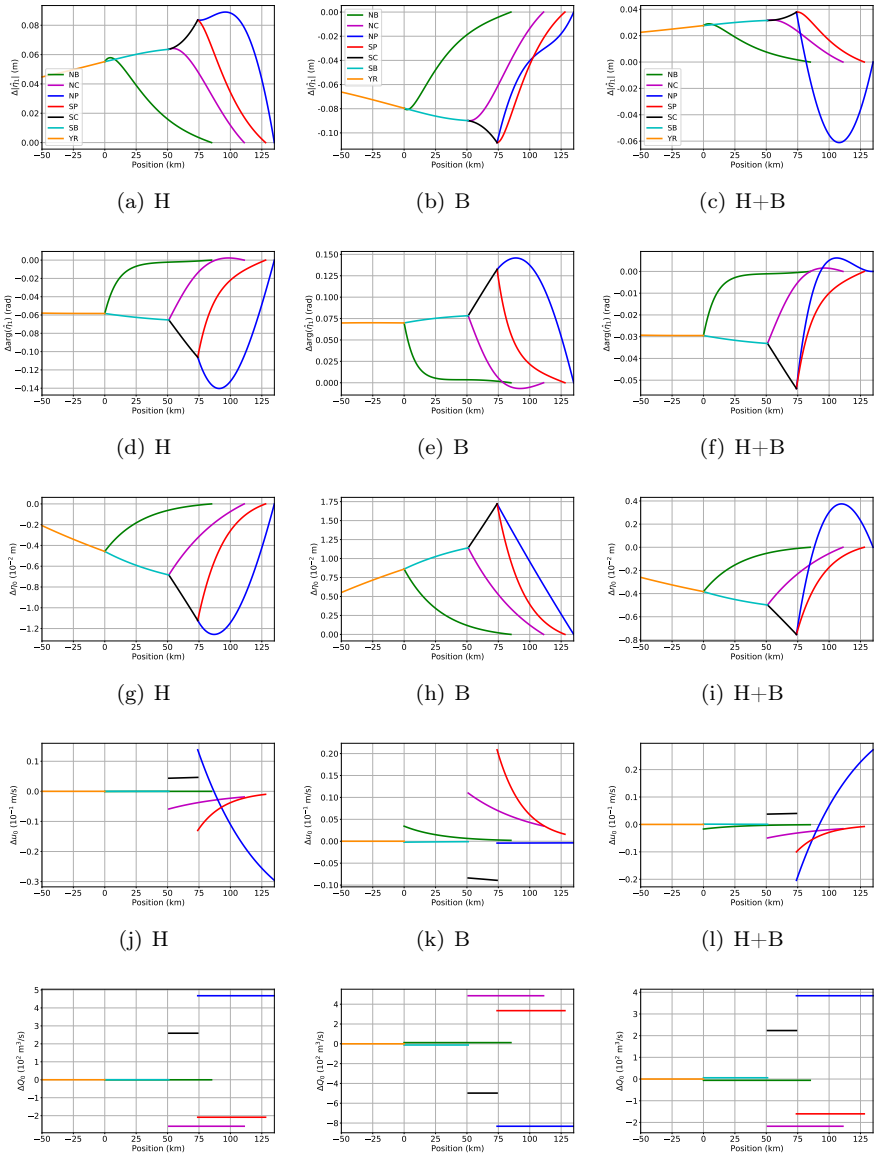

(a) H (b) B (c) H+B

(d) H (e) B (f) H+B

(g) H (h) B (i) H+B

(j) H (k) B (l) H+B

(m) H (n) B (o) H+B

Figure S11: Effects of the DWP in two-folds: larger depth of the NP and smaller width of the NP. First column: only increase depth from 7 to 11m. Second column: only width reduction. Third column: After the DWP, combining the first and the second columns.

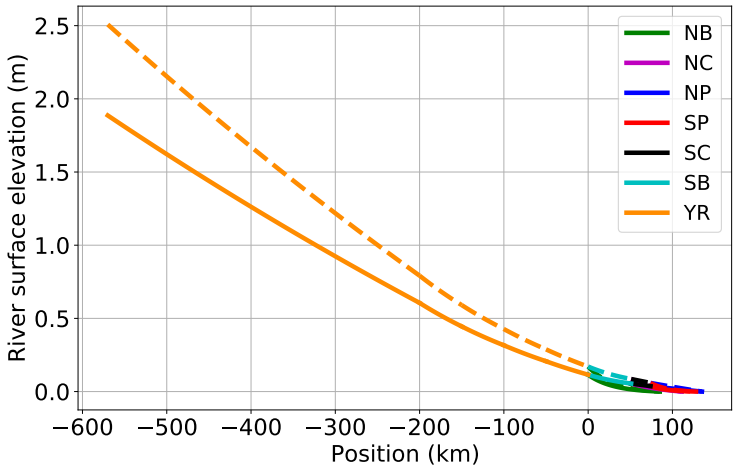

(a)

Figure S12: River set-up for the reference case (dashed line) and under 2 m sea level rise (solid line).

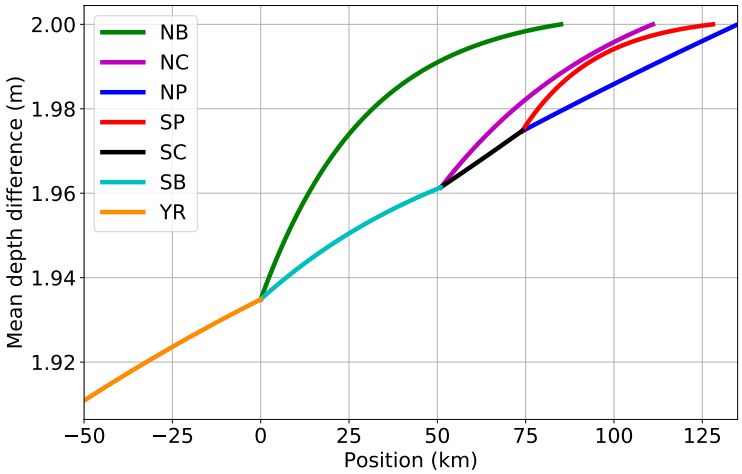

Figure S13: Difference between the mean depth in the situation of 2 m sea level rise and that in the reference case (no sea level rise).

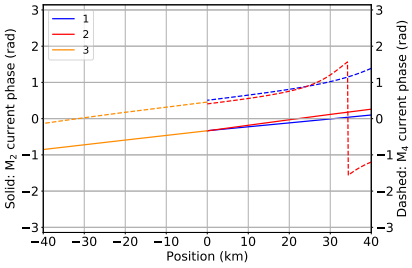

Figure S14: Phases of the depth-averaged M_2 (solid) and M_4 (dashed) tidal currents for the reference case.

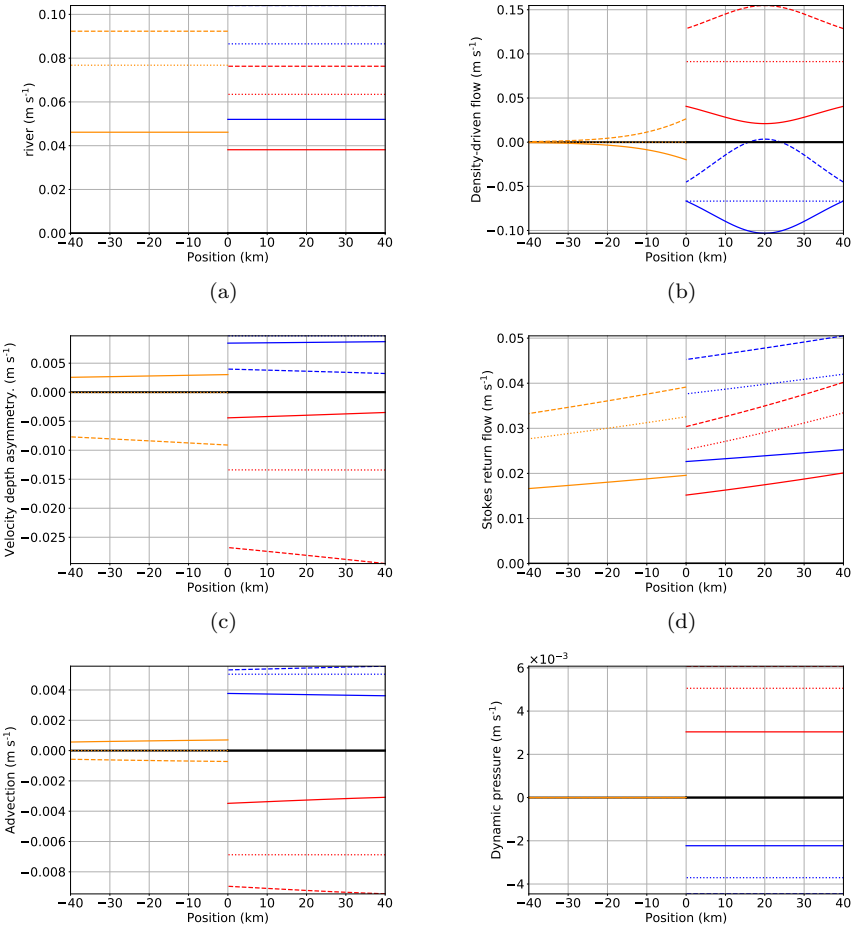

Figure S15: All components in the subtidal flow velocity for the reference case. Solid: velocity on the bottom. Dashed line: velocity near the surface. Dotted line: depth-averaged velocity. Blue: channel 1. Red: channel 2. Dark orange: channel 3.

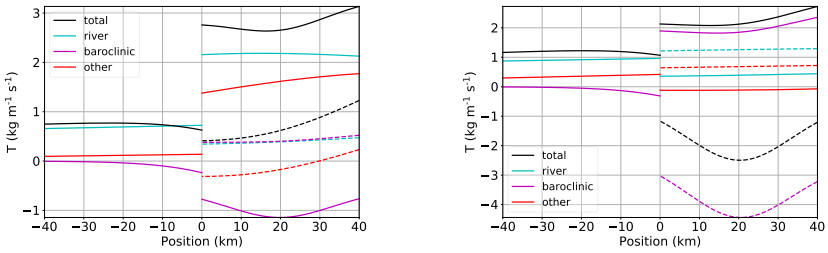

(a) (b)

Figure S16: Components in the advective transport capacity p.u. width T for the mean water depth of channel 1 of 5 m (a) and 20 m (b). Solid: channel 2 and channel 3. Dashed: channel 1.

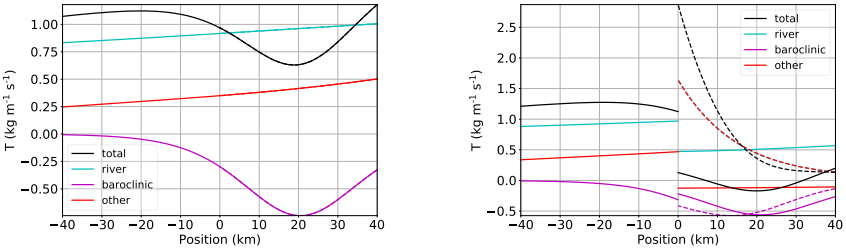

(a) (b)

Figure S17: Components in the advective transport capacity p.u. width T for the width of channel 1 at sea of 500 m (a) and 2000 m (b). Solid lines: channel 2 and channel 3. Dashed lines: channel 1.

Bibliography

Achete, F. M., van der Wegen, M., Roelvink, D., and Jaffe, B. (2016). Suspended sediment dynamics in a tidal channel network under peak river flow. *Ocean Dynamics*, 66(5):703–718, doi:10.1007/s10236-016-0944-0.

Alebregtse, N. C. and de Swart, H. E. (2016). Effect of river discharge and geometry on tides and net water transport in an estuarine network, an idealized model applied to the Yangtze Estuary. *Continental Shelf Research*, 123:29–49, doi:10.1016/j.csr.2016.03.028.

Allen, G., Salomon, J., Bassoullet, P., Du Penhoat, Y., and de Grandpré, C. (1980). Effects of tides on mixing and suspended sediment transport in macrotidal estuaries. *Sedimentary Geology*, 26(1):69–90, doi:10.1016/0037-0738(80)90006-8.

Anderson, D. M., Glibert, P. M., and Burkholder, J. M. (2002). Harmful algal blooms and eutrophication: Nutrient sources, composition, and consequences. *Estuaries*, 25(4):704–726, doi:10.1007/BF02804901.

Bain, R. L., Hale, R. P., and Goodbred, S. L. (2019). Flow reorganization in an anthropogenically modified tidal channel network: An example from the southwestern Ganges-Brahmaputra-Meghna Delta. *Journal of Geophysical Research: Earth Surface*, 124(8):2141–2159, doi:10.1029/2018JF004996.

Bolla Pittaluga, M., Coco, G., and Kleinhans, M. G. (2015). A unified framework for stability of channel bifurcations in gravel and sand fluvial systems. *Geophysical Research Letters*, 42(18):7521–7536, doi:10.1002/2015GL065175.

Bolla Pittaluga, M., Repetto, R., and Tubino, M. (2003). Channel bifurcation in braided rivers: Equilibrium configurations and stability. *Water Resources Research*, 39(3), doi:10.1029/2001WR001112.

Bradshaw, P. (1974). Possible origin of Prandtl's mixing-length theory. *Nature*, 249(5453):135–136, doi:10.1038/249135b0.

van den Bremer, T. S. and Breivik, Ø. (2018). Stokes drift. *Philosophical Transactions of the Royal Society A: Mathematical, Physical and Engineering Sciences*, 376(2111):20170104, doi:10.1098/rsta.2017.0104.

Brouwer, R. L., Schramkowski, G. P., Dijkstra, Y. M., and Schuttelaars, H. M. (2018). Time evolution of estuarine turbidity maxima in well-mixed, tidally dominated estuaries: The role of availability- and erosion-limited conditions. *Journal of Physical Oceanography*, 48(8):1629–1650, doi:10.1175/JPO-D-17-0183.1.

Burchard, H. (2002). *Applied Turbulence Modelling in Marine Waters*. Springer-Verlag Berlin Heidelberg, doi:10.1007/3-540-45419-5.

Burchard, H., Schuttelaars, H. M., and Ralston, D. K. (2018). Sediment trapping in estuaries. *Annual Review of Marine Science*, 10(1):371–395, doi:10.1146/annurev-marine-010816-060535.

Buschman, F. A., Hoitink, A. J. F., van der Vegt, M., and Hoekstra, P. (2010). Subtidal flow division at a shallow tidal junction. *Water Resources Research*, 46(12), doi:10.1029/2010WR009266.

Buschman, F. A., van der Vegt, M., Hoitink, A. J. F., and Hoekstra, P. (2013). Water and suspended sediment division at a stratified tidal junction. *Journal of Geophysical Research: Oceans*, 118(3):1459–1472, doi:10.1002/jgrc.20124.

Cai, H., Savenije, H. H. G., Garel, E., Zhang, X., Guo, L., Zhang, M., Liu, F., and Yang, Q. (2019). Seasonal behaviour of tidal damping and residual water level slope in the Yangtze River estuary: identifying the critical position and river discharge for maximum tidal damping. *Hydrology and Earth System Sciences*, 23(6):2779–2794, doi:10.5194/hess-23-2779-2019.

Cameron, W. and Pritchard, D. (1963). Estuaries. *The Sea*, 2:306–324.

Castaing, P. and Allen, G. P. (1981). Mechanisms controlling seaward escape of suspended sediment from the Gironde: A macrotidal estuary in France. *Marine Geology*, 40(1):101–118, doi:10.1016/0025-3227(81)90045-1.

Chen, W. and de Swart, H. E. (2016). Dynamic links between shape of the eddy viscosity profile and the vertical structure of tidal current amplitude in bays and estuaries. *Ocean Dynamics*, 66(3):299–312, doi:10.1007/s10236-015-0919-6.

Cheng, H., Chen, J., Chen, Z., Ruan, R., Xu, G., Zeng, G., Zhu, J., Dai, Z., Chen, X., Gu, S., Zhang, X., and Wang, H. (2018). Mapping sea level rise behavior in an estuarine delta system: A case study along the Shanghai coast. *Engineering*, 4(1):156–163, doi:10.1016/j.eng.2018.02.002.

Cheng, P., Mao, J., Yu, F., Chen, N., Wang, A., and Xu, F. (2019). A numerical study of residual flow induced by eddy viscosity-shear covariance in a tidally energetic estuary. *Estuarine, Coastal and Shelf Science*, 230:106446, doi:10.1016/j.ecss.2019.106446.

Cheng, P., Valle-Levinson, A., and de Swart, H. E. (2010). Residual currents induced by asymmetric tidal mixing in weakly stratified narrow estuaries. *Journal of Physical Oceanography*, 40(9):2135–2147, doi:10.1175/2010JPO4314.1.

Chernetsky, A., Schuttelaars, H., and Talke, S. (2010). The effect of tidal asymmetry and temporal settling lag on sediment trapping in tidal estuaries. *Ocean Dynamics*, 60:1219–1241, doi:10.1007/s10236-010-0329-8.

Cloern, J. E., Abreu, P. C., Carstensen, J., Chauvaud, L., Elmgren, R., Grall, J., Greening, H., Johansson, J. O. R., Kahru, M., Sherwood, E. T., Xu, J., and Yin, K. (2016). Human activities and climate variability drive fast-paced change across the world's estuarine–coastal ecosystems. *Global Change Biology*, 22(2):513–529, doi:10.1111/gcb.13059.

Cowan Jr., J. H., Yáñez-Arancibia, A., Sánchez-Gil, P., and Deegan, L. A. (2012). *Estuarine Nekton*, chapter 13, pages 327–355. John Wiley & Sons, Ltd, doi:10.1002/9781118412787.ch13.

Cox, T., Maris, T., De Vleeschauwer, P., De Mulder, T., Soetaert, K., and Meire, P. (2006). Flood control areas as an opportunity to restore estuarine habitat. *Ecological Engineering*, 28(1):55–63, doi:10.1016/j.ecoleng.2006.04.001.

Defant, A. (1961). *Physical Oceanography*. Pergamon Press.

Dijkstra, Y. M., Brouwer, R. L., Schuttelaars, H. M., and Schramkowski, G. P. (2017a). The iFlow modelling framework v2.4: a modular idealized process-based model for flow and transport in estuaries. *Geoscientific Model Development*, 10(7):2691–2713, doi:10.5194/gmd-10-2691-2017.

Dijkstra, Y. M., Schuttelaars, H. M., and Burchard, H. (2017b). Generation of exchange flows in estuaries by tidal and gravitational eddy viscosity-shear covariance (esco). *Journal of Geophysical Research: Oceans*, 122(5):4217–4237, doi:10.1002/2016JC012379.

Dijkstra, Y. M., Schuttelaars, H. M., Schramkowski, G. P., and Brouwer, R. L. (2019). Modeling the transition to high sediment concentrations as a response to channel deepening in the Ems river estuary. *Journal of Geophysical Research: Oceans*, 124(3):1578–1594, doi:10.1029/2018JC014367.

Dijkstra, Y. M., Schuttelaars, H. M., and Winterwerp, J. C. (2018). The hyperturbid state of the water column in estuaries and rivers: the importance

of hindered settling. *Ocean Dynamics*, 68(3):377–389, doi:10.1007/s10236-018-1132-1.

Dronkers, J. J. (1964). *Tidal Computations in Rivers and Coastal Waters.* Amsterdam, North-Holland Pub. Co.; New York, Interscience Publishers.

Eloot, K. and Vantorre, M. (2011). *Ship behaviour in shallow and confined water: an overview of hydrodynamic effects through EFD.* NATO Research and Technology Organisation (RTO).

Engelund, F. (1970). Instability of erodible beds. *Journal of Fluid Mechanics*, 42(2):225–244, doi:10.1017/S0022112070001210.

Festa, J. F. and Hansen, D. V. (1978). Turbidity maxima in partially mixed estuaries: A two-dimensional numerical model. *Estuarine and Coastal Marine Science*, 7(4):347–359, doi:10.1016/0302-3524(78)90087-7.

Friedrichs, C. T. (2010). Barotropic tides in channelized estuaries. In Valle-Levinson, A., editor, *Contemporary Issues in Estuarine Physics*, pages 27–61. Cambridge University Press.

Friedrichs, C. T., Armbrust, B. A., and de Swart, H. E. (1998). Hydrodynamics and equilibrium sediment dynamics of shallow, funnel-shaped tidal estuaries. In Dronkers, J. and Scheffers, M., editors, *Physics of Estuaries and Coastal Seas*. Balkema Press.

Friedrichs, C. T. and Aubrey, D. G. (1988). Non-linear tidal distortion in shallow well-mixed estuaries: a synthesis. *Estuarine, Coastal and Shelf Science*, 27(5):521–545, doi:10.1016/0272-7714(88)90082-0.

Friedrichs, C. T. and Aubrey, D. G. (1994). Tidal propagation in strongly convergent channels. *Journal of Geophysical Research: Oceans*, 99(C2):3321–3336, doi:10.1029/93JC03219.

García-García, L. M., Campos, C. J., Kershaw, S., Younger, A., and Bacon, J. (2021). Scenarios of intermittent E. coli contamination from sewer overflows to shellfish growing waters: The Dart Estuary case study. *Marine Pollution Bulletin*, 167:112332, doi:10.1016/j.marpolbul.2021.112332.

Gerkema, T. (2019). *An Introduction to Tides.* Cambridge University Press, doi:10.1017/9781316998793.

Geyer, W. R. (1993). The importance of suppression of turbulence by stratification on the estuarine turbidity maximum. *Estuaries*, 16(1):113–125, doi:10.2307/1352769.

Geyer, W. R. and MacCready, P. (2014). The estuarine circulation. *Annual Review of Fluid Mechanics*, 46(1):175–197, doi:10.1146/annurev-fluid-010313-141302.

Godin, G. (1991). Compact approximations to the bottom friction term, for the study of tides propagating in channels. *Continental Shelf Research*, 11(7):579–589, doi:10.1016/0278-4343(91)90013-V.

Godin, G. (1999). The propagation of tides up rivers with special considerations on the upper Saint Lawrence River. *Estuarine, Coastal and Shelf Science*, 48(3):307–324, doi:10.1006/ecss.1998.0422.

Guo, L., van der Wegen, M., Jay, D. A., Matte, P., Wang, Z. B., Roelvink, D., and He, Q. (2015). River-tide dynamics: Exploration of nonstationary and nonlinear tidal behavior in the Yangtze River estuary. *Journal of Geophysical Research: Oceans*, 120(5):3499–3521, doi:10.1002/2014JC010491.

Hansen, D. V. and Rattray, Jr., M. (1965). Gravitational circulation in straits and estuaries. *Journal of Marine Research*, 23(104-122).

Hepkema, T. M., de Swart, H. E., Zagaris, A., and Duran-Matute, M. (2018). Sensitivity of tidal characteristics in double inlet systems to momentum dissipation on tidal flats: a perturbation analysis. *Ocean Dynamics*, 68(4):439–455, doi:10.1007/s10236-018-1142-z.

Hill, A. E. and Souza, A. J. (2006). Tidal dynamics in channels: 2. Complex channel networks. *Journal of Geophysical Research: Oceans*, 111(C11), doi:10.1029/2006JC003670.

Hoitink, A. and Jay, D. (2016). Tidal river dynamics: Implications for deltas. *Reviews of Geophysics*, doi:10.1002/2015RG000507.

Hudson, A. S., Talke, S. A., and Jay, D. A. (2017). Using satellite observations to characterize the response of estuarine turbidity maxima to external forcing. *Estuaries and Coasts*, 40(2):343–358, doi:10.1007/s12237-016-0164-3.

Ianniello, J. P. (1977). Tidally induced residual currents in estuaries of constant breadth and depth. *Journal of Marine Research*, 35:755–786.

Ianniello, J. P. (1979). Tidally induced residual currents in estuaries of variable breadth and depth. *Journal of Physical Oceanography*, 9(5):962–974, doi:10.1175/1520-0485(1979)009<0962:TIRCIE>2.0.CO;2.

IPCC (2019). Special report on the ocean and cryoshpere in a changing climate. `https://www.ipcc.ch/srocc/`.

IPCC (2022). Climate change 2022: Mitigation of climate change working group III contribution to the ipcc sixth assessment report. `https://www.ipcc.ch/report/sixth-assessment-report-working-group-3/`.

Iwantoro, A. P., van der Vegt, M., and Kleinhans, M. G. (2022). Stability and asymmetry of tide-influenced river bifurcations. *Journal of Geophysical Research: Earth Surface*, 127(6):e2021JF006282, doi:10.1029/2021JF006282.

Jiang, C., Li, J., and de Swart, H. E. (2012). Effects of navigational works on morphological changes in the bar area of the Yangtze Estuary. *Geomorphology*, 139-140:205–219, doi:10.1016/j.geomorph.2011.10.020.

Jiang, C., de Swart, H., Li, J., and Liu, G. (2013a). Mechanisms of along-channel sediment transport in the North Passage of the Yangtze Estuary and their response to large-scale interventions. *Ocean Dynamics*, 63, doi:10.1007/s10236-013-0594-4.

Jiang, X., Lu, B., and He, Y. (2013b). Response of the turbidity maximum zone to fluctuations in sediment discharge from river to estuary in the Changjiang Estuary (China). *Estuarine, Coastal and Shelf Science*, 131:24–30, doi:10.1016/j.ecss.2013.07.003.

Kennish, M. (1990). *Ecology of Estuaries*. CRC Press, doi:10.1201/9781351071598.

Kessarkar, P. M., Purnachandra Rao, V., Shynu, R., Ahmad, I. M., Mehra, P., Michael, G. S., and Sundar, D. (2009). Wind-driven estuarine turbidity maxima in Mandovi Estuary, central west coast of India. *Journal of Earth System Science*, 118(4):369, doi:10.1007/s12040-009-0026-5.

Kleinhans, M. G., Ferguson, R. I., Lane, S. N., and Hardy, R. J. (2013). Splitting rivers at their seams: bifurcations and avulsion. *Earth Surface Processes and Landforms*, 38(1):47–61, doi:10.1002/esp.3268.

Kleinhans, M. G., Jagers, H. R. A., Mosselman, E., and Sloff, C. J. (2008). Bifurcation dynamics and avulsion duration in meandering rivers by one-dimensional and three-dimensional models. *Water Resources Research*, 44(8), doi:10.1029/2007WR005912.

van de Kreeke, J. (1988). Hydrodynamics of tidal inlets. In Aubrey, D. G. and Weishar, L., editors, *Hydrodynamics and Sediment Dynamics of Tidal Inlets Hydrodynamics and sediment dynamics of tidal inlets*, volume 29 of *Coastal and Estuarine Studies*, pages 1–23. Springer-Verlag New York.

Kuang, C., Chen, W., Gu, J., and He, L. (2014a). Comprehensive analysis on the sediment siltation in the upper reach of the deepwater navigation channel in the Yangtze Estuary. *Journal of Hydrodynamics*, 26(2):299–308, doi:10.1016/S1001-6058(14)60033-0.

Kuang, C., Chen, W., Gu, J., Zhu, D. Z., He, L., and Huang, H. (2014b). Numerical assessment of the impacts of potential future sea level rise on hydrodynamics of the Yangtze River Estuary, China. *Journal of Coastal Research*, 30(3):586–597, doi:10.2112/JCOASTRES-D-13-00149.1.

Kuang, C., Liang, H., Mao, X., Karney, B., Gu, J., Huang, H., Chen, W., and Song, H. (2017). Influence of potential future sea-level rise on tides in the China Sea. *Journal of Coastal Research*, 33(1):105–117, doi:10.2112/JCOASTRES-D-16-00057.1.

Kundu, P. K., Cohen, I. M., and Dowling, D. R. (2016). *Fluid Mechanics*. Academic Press, Boston, 6 edition.

Lange, X. and Burchard, H. (2019). The relative importance of wind straining and gravitational forcing in driving exchange flows in tidally energetic estuaries. *Journal of Physical Oceanography*, 49(3):723–736, doi:10.1175/JPO-D-18-0014.1.

Lanzoni, S. and Seminara, G. (1998). On tide propagation in convergent estuaries. *Journal of Geophysical Research: Oceans*, 103(C13):30793–30812, doi:10.1029/1998JC900015.

Li, L., He, Z., Xia, Y., and Dou, X. (2018). Dynamics of sediment transport and stratification in Changjiang River Estuary, China. *Estuarine, Coastal and Shelf Science*, 213:1–17, doi:10.1016/j.ecss.2018.08.002.

Li, L., Zhu, J., Wu, H., and Wang, B. (2010). A numerical study on water diversion ratio of the Changjiang (Yangtze) estuary in dry season. *Chinese Journal of Oceanology and Limnology*, 28(3):700–712, doi:10.1007/s00343-010-9114-2.

Li, Z., Jia, J., Wang, Y. P., and Zhang, G. (2022). Net suspended sediment transport modulated by multiple flood-ebb asymmetries in the progressive tidal wave dominated and partially stratified Changjiang Estuary. *Marine Geology*, 443:106702, doi:10.1016/j.margeo.2021.106702.

Li, Z., Jia, J., Wu, Y., Zong, H., Zhang, G., Wang, Y. P., Yang, Y., Zhou, L., and Gao, S. (2019). Vertical distributions of suspended sediment concentrations in the turbidity maximum zone of the periodically and partially stratified Changjiang Estuary. *Estuaries and Coasts*, 42(6):1475–1490, doi:10.1007/s12237-019-00605-2.

Lorentz, H. A. (1926). Verslag van de Staatscommissie Zuiderzee. *'s Gravenhage: Algemeene Landsdrukkerij, (in Dutch)*.

Lu, S., Tong, C., Lee, D.-Y., Zheng, J., Shen, J., Zhang, W., and Yan, Y. (2015). Propagation of tidal waves up in Yangtze Estuary during the dry season. *Journal of Geophysical Research: Oceans*, 120(9):6445–6473, doi:10.1002/2014JC010414.

Luo, W., Shen, F., He, Q., Cao, F., Zhao, H., and Li, M. (2022). Changes in suspended sediments in the Yangtze River Estuary from 1984 to 2020:

Responses to basin and estuarine engineering constructions. *Science of The Total Environment*, 805:150381, doi:10.1016/j.scitotenv.2021.150381.

Maas, L. and van Haren, J. (1987). Observations on the vertical structure of tidal and inertial currents in the central North Sea. *Journal of Marine Research*, 45:293–318, doi:10.1357/002224087788401106.

MacCready, P. (2004). Toward a unified theory of tidally-averaged estuarine salinity structure. *Estuaries and Coasts*, 27:561–570, doi:10.1007/BF02907644.

McLachlan, R., Ogston, A., Asp, N., Fricke, A., Nittrouer, C., and Gomes, V. (2020). Impacts of tidal-channel connectivity on transport asymmetry and sediment exchange with mangrove forests. *Estuarine, Coastal and Shelf Science*, 233:106524, doi:10.1016/j.ecss.2019.106524.

McSweeney, J. M., Chant, R. J., Wilkin, J. L., and Sommerfield, C. K. (2017). Suspended sediment impacts on light-limited productivity in the Delaware Estuary. *Estuaries and Coasts*, 40(4):977–993, doi:10.1007/s12237-016-0200-3.

Murray, A. B. (2003). *Contrasting the Goals, Strategies, and Predictions Associated with Simplified Numerical Models and Detailed Simulations*, pages 151–165. American Geophysical Union, doi:10.1029/135GM11.

Nassehi, V. and Bikangaga, J. (1993). A mathematical model for the hydrodynamics and pollutants transport in long and narrow tidal rivers. *Applied Mathematical Modelling*, 17(8):415–422, doi:10.1016/0307-904X(93)90116-X.

National Marine Data and Information Service (2013). *Tide Tables 2014*, volume 2. China Ocean Press (in Chinese).

Nezu, I. and Nakagawa, H. (1993). *Turbulence in Open-Channel Flows*. Taylor & Francis, doi:10.1201/9780203734902.

Nicholls, R. J., Marinova, N., Lowe, J. A., Brown, S., Vellinga, P., de Gusmão, D., Hinkel, J., and Tol, R. S. J. (2011). Sea-level rise and its possible impacts given a "beyond 4 °C world" in the twenty-first century. *Philosophical Transactions of the Royal Society A: Mathematical, Physical and Engineering Sciences*, 369(1934):161–181, doi:10.1098/rsta.2010.0291.

Nieuwstadt, F. T. M., Boersma, B. J., and Westerweel, J. (2016). *Turbulence: Introduction to Theory and Applications of Turbulent Flows*. Springer, Cham, doi:10.1007/978-3-319-31599-7.

Parker, B. (1984). *Frictional effects on the tidal dynamics of a shallow estuary*. PhD thesis, The Johns Hopkins University.

Pritchard, D. W. (1954). A study of the salt balance in a coastal plain estuary. *Journal of Marine Research*.

Pu, X., Shi, J. Z., and Hu, G.-D. (2016). Analyses of intermittent mixing and stratification within the North Passage of the Changjiang (Yangtze) River estuary, China: A three-dimensional model study. *Journal of Marine Systems*, 158:140–164, doi:10.1016/j.jmarsys.2016.02.004.

Ragno, N., Tambroni, N., and Bolla Pittaluga, M. (2020). Effect of small tidal fluctuations on the stability and equilibrium configurations of bifurcations. *Journal of Geophysical Research: Earth Surface*, 125(8), doi:10.1029/2020JF005584.

Redolfi, M., Zolezzi, G., and Tubino, M. (2016). Free instability of channel bifurcations and morphodynamic influence. *Journal of Fluid Mechanics*, 799:476–504, doi:10.1017/jfm.2016.389.

Ridderinkhof, H. (1988). Tidal and residual flows in the western Dutch Wadden sea II: An analytical model to study the constant flow between connected tidal basins. *Netherlands Journal of Sea Research*, 22(3):185–198, doi:10.1016/0077-7579(88)90022-1.

Ridderinkhof, W., de Swart, H. E., van der Vegt, M., Alebregtse, N. C., and Hoekstra, P. (2014). Geometry of tidal inlet systems: A key factor for the net sediment transport in tidal inlets. *Journal of Geophysical Research: Oceans*, 119(10):6988–7006, doi:10.1002/2014JC010226.

Salahuddin and Lambiase, J. J. (2013). Sediment dynamics and depositional systems of the Mahakam Delta, Indonesia: Ongoing delta abandonment on a tide-dominated coast. *Journal of Sedimentary Research*, 83(7):503–521, doi:10.2110/jsr.2013.42.

Sassi, M. G., Hoitink, A. J. F., de Brye, B., Vermeulen, B., and Deleersnijder, E. (2011). Tidal impact on the division of river discharge over distributary channels in the Mahakam Delta. *Ocean Dynamics*, 61(12):2211–2228, doi:10.1007/s10236-011-0473-9.

Sassi, M. G., Hoitink, A. J. F., Vermeulen, B., and Hidayat, H. (2013). Sediment discharge division at two tidally influenced river bifurcations. *Water Resources Research*, 49(4):2119–2134, doi:10.1002/wrcr.20216.

Savenije, H., Toffolon, M., Haas, J., and Veling, E. (2008). Analytical description of tidal dynamics in convergent estuaries. *Journal of Geophysical Research*, 113.

Schoellhamer, D. H. (2011). Sudden clearing of estuarine waters upon crossing the threshold from transport to supply regulation of sediment transport as

an erodible sediment pool is depleted: San Francisco Bay, 1999. *Estuaries and Coasts*, 34(5):885–899, doi:10.1007/s12237-011-9382-x.

Schramkowski, G. and de Swart, H. (2002). Morphodynamic equilibrium in straight tidal channels: Combined effects of the Coriolis force and external overtides. *Journal of Geophysical Research: Oceans*, 107(C12):20–1–20–17, doi:10.1029/2000JC000693.

Scully, M. E., Geyer, W. R., and Lerczak, J. A. (2009). The influence of lateral advection on the residual estuarine circulation: A numerical modeling study of the Hudson River Estuary. *Journal of Physical Oceanography*, 39(1):107–124, doi:10.1175/2008JPO3952.1.

Shan, S., Hannah, C. G., and Wu, Y. (2019). Coupling of estuarine circulations in a network of fjords. *Journal of Geophysical Research: Oceans*, 124(10):6809–6830, doi:10.1029/2018JC014924.

Shao, Y., Shen, X., Maa, J. P.-Y., and Shen, J. (2017). Simulating high ebb currents in the North Passage of the Yangtze Estuary using a vertical 1-D model. *Estuarine, Coastal and Shelf Science*, 196:399–410, doi:10.1016/j.ecss.2017.08.001.

Simpson, J. H., Brown, J., Matthews, J., and Allen, G. (1990). Tidal straining, density currents, and stirring in the control of estuarine stratification. *Estuaries*, 13(2):125–132, doi:10.2307/1351581.

Smith, J. D. and McLean, S. R. (1977). Spatially averaged flow over a wavy surface. *Journal of Geophysical Research (1896-1977)*, 82(12):1735–1746, doi:10.1029/JC082i012p01735.

Soulsby, R. (1997). *Dynamics of marine sands. A manual for practical applications*. Thomas Telford, London.

Souza, A. J. (2013). On the use of the Stokes number to explain frictional tidal dynamics and water column structure in shelf seas. *Ocean Science*, 9(2):391–398, doi:10.5194/os-9-391-2013.

Stacey, M. T. and Ralston, D. K. (2005). The scaling and structure of the estuarine bottom boundary layer. *Journal of Physical Oceanography*, 35(1):55–71, doi:10.1175/JPO-2672.1.

Stein, U. and Alpert, P. (1993). Factor separation in numerical simulations. *Journal of Atmospheric Sciences*, 50(14):2107–2115, doi:10.1175/1520-0469(1993)050<2107:FSINS>2.0.CO;2.

Stokes, G. G. (1847). On the theory of oscillatory waves. *Transactions of the Cambridge Philosophical Society*, doi:10.1017/CBO9780511702242.013.

de Swart, H. and Zimmerman, J. (2009). Morphodynamics of tidal inlet systems. *Annual Review of Fluid Mechanics*, 41(1):203–229, doi:10.1146/annurev.fluid.010908.165159.

Talke, S. A. and Jay, D. A. (2020). Changing tides: The role of natural and anthropogenic factors. *Annual Review of Marine Science*, 12(1):121–151, doi:10.1146/annurev-marine-010419-010727.

Talke, S. A., de Swart, H. E., and de Jonge, V. N. (2009). An idealized model and systematic process study of oxygen depletion in highly turbid estuaries. *Estuaries and Coasts*, 32(4):602–620, doi:10.1007/s12237-009-9171-y.

Teng, L., Cheng, H., de Swart, H., Dong, P., Li, Z., Li, J., and Wang, Y. (2021). On the mechanism behind the shift of the turbidity maximum zone in response to reclamations in the Yangtze (Changjiang) Estuary, China. *Marine Geology*, 440:106569, doi:10.1016/j.margeo.2021.106569.

Valle-Levinson, A. (2010). *Definition and classification of estuaries*, chapter 1, pages 1–11. Cambridge University Press, Cambridge, doi:10.1017/CBO9780511676567.

van Maren, D., van Kessel, T., Cronin, K., and Sittoni, L. (2015). The impact of channel deepening and dredging on estuarine sediment concentration. *Continental Shelf Research*, 95:1–14, doi:10.1016/j.csr.2014.12.010.

Wan, Y. and Zhao, D. (2017). Observation of saltwater intrusion and ETM dynamics in a stably stratified estuary: the Yangtze Estuary, China. *Environmental Monitoring and Assessment*, 189(2):89, doi:10.1007/s10661-017-5797-6.

Wang, Z., Vries, M. D., Fokkink, R., and Langerak, A. (1995). Stability of river bifurcations in id morphodynamic models. *Journal of Hydraulic Research*, 33(6):739–750, doi:10.1080/00221689509498549.

Winterwerp, J. C., Erftemeijer, P. L. A., Suryadiputra, N., van Eijk, P., and Zhang, L. (2013). Defining eco-morphodynamic requirements for rehabilitating eroding mangrove-mud coasts. *Wetlands*, 33(3):515–526, doi:10.1007/s13157-013-0409-x.

Winterwerp, J. C. and van Kesteren, W. G. (2004). *Introduction to the Physics of Cohesive Sediment Dynamics in the Marine Environment*. Elsevier.

Wu, H., Zhu, J., Chen, B., and Chen, Y. (2006). Quantitative relationship of runoff and tide to saltwater spilling over from the North Branch in the Changjiang Estuary: A numerical study. *Estuarine, Coastal and Shelf Science*, 69(1):125–132, doi:10.1016/j.ecss.2006.04.009.

Yang, Z., Cheng, H., and Li, J. (2015). Nonlinear advection, Coriolis force, and frictional influence in the South Channel of the Yangtze Estuary, China. *Science China Earth Sciences*, 58(3):429–435, doi:10.1007/s11430-014-4946-9.

Zaikowski, L., McDonnell, K. T., Rockwell, R. F., and Rispoli, F. (2008). Temporal and spatial variations in water quality on New York south shore estuary tributaries: Carmans, Patchogue, and Swan Rivers. *Estuaries and Coasts*, 31(1):85–100, doi:10.1007/s12237-007-9010-y.

Zhan, W., Wu, J., Wei, X., Tang, S., and Zhan, H. (2019). Spatio-temporal variation of the suspended sediment concentration in the Pearl River Estuary observed by MODIS during 2003–2015. *Continental Shelf Research*, 172:22–32, doi:10.1016/j.csr.2018.11.007.

Zhang, E., Savenije, H. H., Wu, H., Kong, Y., and Zhu, J. (2011). Analytical solution for salt intrusion in the Yangtze Estuary, China. *Estuarine, Coastal and Shelf Science*, 91(4):492–501, doi:10.1016/j.ecss.2010.11.008.

Zhang, E., Savenije, H. H. G., Chen, S., and Mao, X. (2012). An analytical solution for tidal propagation in the Yangtze Estuary, China. *Hydrology and Earth System Sciences*, 16(9):3327–3339, doi:10.5194/hess-16-3327-2012.

Zhang, M., Townend, I., Zhou, Y., and Cai, H. (2016). Seasonal variation of river and tide energy in the Yangtze Estuary, China. *Earth Surface Processes and Landforms*, 41(1):98–116, doi:10.1002/esp.3790.

Zhang, W., Feng, H., Hoitink, A., Zhu, Y., Gong, F., and Zheng, J. (2017). Tidal impacts on the subtidal flow division at the main bifurcation in the Yangtze River Delta. *Estuarine, Coastal and Shelf Science*, 196:301–314, doi:10.1016/j.ecss.2017.07.008.

Zhu, C., van Maren, D. S., Guo, L., Lin, J., He, Q., and Wang, Z. B. (2021). Effects of sediment-induced density gradients on the estuarine turbidity maximum in the Yangtze Estuary. *Journal of Geophysical Research: Oceans*, 126(5):e2020JC016927, doi:10.1029/2020JC016927.

Zhu, J., Wu, H., Li, L., and Qiu, C. (2018). Saltwater intrusion in the Changjiang Estuary. In Liang, X. S. and Zhang, Y., editors, *Coastal Environment, Disaster, and Infrastructure*, chapter 3, pages 49–73. IntechOpen.

Zhu, L., He, Q., Shen, J., and Wang, Y. (2016). The influence of human activities on morphodynamics and alteration of sediment source and sink in the Changjiang Estuary. *Geomorphology*, 273:52–62, doi:10.1016/j.geomorph.2016.07.025.

Zimmerman, J. (1982). On the Lorentz linearization of a quadratically damped forced oscillator. *Physics Letters A*, 89(3):123–124, doi:10.1016/0375-9601(82)90871-4.

Summary

Estuaries are bodies of water that connect rivers to seas. Many of them are composed of multiple interconnected channels and thus constitute a so-called estuarine channel network. They are important for both ecology and the economy. Freshwater and fluvial sediments are continuously discharged into the system by the river flow. Additionally, the tidal flow causes water and sediments being periodically imported from and exported into the open sea. Water and sediments are exchanged at the junctions of the channels. Therefore, estuarine channel networks feature complex hydrodynamics and sediment dynamics. The latter gives rise to the estuarine turbidity maximum (ETM), where the suspended sediment concentration attains a local maximum. The aim of this thesis is to understand more about the response of the hydrodynamics and the ETM dynamics in estuarine channel networks to natural environmental conditions, as well as due to changes in these conditions due to e.g., climate change or anthropogenic measures.

Chapter 2 describes how tidal propagation and the distribution of river water transport in estuarine channel networks depend on the freshwater discharge, external tidal forcing, local changes in the geometry, and sea level rise. This is achieved by the development of a semi-analytical model that simulates the interacting river and tidal flow in the estuarine channel network. The water motion is forced by a semi-diurnal tide (M_2 tide) at the end of every channel that is connected to the open sea and a constant river discharge at each tidal limit. Mass conservation and continuous water level are assumed at all the junctions. The model is applied to a prototype system, viz. the Yangtze Estuary. Results are in good agreement with field data and show that an increase in either the river flow or tidal flow enhances the friction experienced by both the river flow and tidal flow through the intensified river-tide interactions, which are characterised by both the bottom stress and turbulent shear stress. Therefore, a larger river discharge reduces the tidal current and phase speed of the tidal wave. The river water transport in every channel is proportional

to the river discharge and hence the distribution of river water transport over channels is unaffected by the river discharge. A positive correlation between the tidal current amplitude throughout the estuarine channel network and the prescribed tidal range is found. Hence, the prescribed tidal range hardly has any impact on the distribution of river water transport. Adding a shortcut channel reduces the water level difference between the channels that it connects. The local deepening and narrowing of one channel have opposite effects on both tidal propagation and river water transport because of their opposing effects on the channel cross-sectional area. Sea level rise increases the cross-sectional area in every channel, causing the river current to decrease and hence less mean water level set-up is required to drive the river flow. As depth varies over channels, the relative change in mean water depth is the largest in the shallowest channel. Therefore, more river water transport is distributed to shallower channels from the deeper channels.

Net (i.e., tidally averaged) water transport in the channels of an estuarine network is not only caused by river flow, but also by, e.g., the horizontal density gradients and tides. The latter may generate net water transport through tidal rectification processes induced by nonlinear terms in the hydrodynamic equations, such as advection of momentum, excess volume transport due to varying sea surface height (resulting in Stokes transport), and the asymmetry in the velocity vertical profile over a tidal cycle (resulting in velocity-depth asymmetry). The net water transport and its components are studied in Chapter 3 by extending the model used in Chapter 2. Model results from applying the model to the Yangtze Estuary agree fairly well with those reported in the literature. In an estuarine channel network with the maximum river flow velocity comparable to the maximum tidal flow velocity, the distribution of net water transport is weakly sensitive to the river discharge. This is because the net water transport is dominated by the river water transport, the distribution of which is insensitive to the river discharge. The net water transport due to tides in every channel scales almost linearly with the prescribed tidal elevation amplitudes. For a well-mixed estuarine channel network, the changes in the contribution of horizontal density gradients to the net water transport are negligible. Model results further show that the deepening of the North Passage results in more seaward net water transport due to river and tides, while less seaward due to the horizontal density gradient. The narrowing due to a reduction in the width convergence caused the channel to receive less river water transport from the upstream channel. Sea level rise up to 2 m results in a more even partition of the river water transport at every junction. However, the distribution of net water transport in the Yangtze Estuary is less sensitive to sea level rise, because the change in every component in the net water transport compensates as the sea level rises. This finding applies particularly to the Yangtze Estuary and has been reported in other studies.

Several field observations in estuarine channel networks have revealed the existence of ETM in multiple channels at the same time. In addition, ETMs

may travel from one channel to another over the course of a season. Moreover, they may vanish after construction of navigational channels or upstream dams, which reduce the fluvial sediment input. To better understand the dependence of ETMs in an estuarine network on fluvial sediment discharge and on changes in depth and width convergence in one channel of the network, the model used in Chapter 3 is further extended by coupling the suspended sediment dynamics to water motion. In every channel, the sediment is resuspended from the bed by the tidal current and the morphodynamic equilibrium condition is assumed, i.e., over one tidal cycle, deposition and erosion of sediment balance. At every junction, the suspended sediment satisfies the mass conservation and the subtidal depth-averaged concentration is assumed to be continuous. To acquire more fundamental knowledge about the complex sediment dynamics in an estuary, the model is applied to an idealised three-channel network system, in which the horizontal net transport of sediment is mainly due to the river flow and density-driven flow. The location of an ETM is close to the location of sediment trapping, where the net sediment transport equals the sediment transport capacity. By continuously varying the fluvial sediment discharge, with the same river discharge and the same horizontal density gradients, an enhanced fluvial sediment discharge increases the global sediment concentration and causes the upstream shift of the ETM locations. Depending on the relative strength of the sediment transport due to river flow and density-driven flow, the deepening of a seaward channel may cause the ETM in the seaward channels to shift in either direction. If the net sediment transport caused by the river flow dominates over that caused by the density-driven flow, the ETM shifts downstream in the deepened channel and upstream in the other seaward channel. Conversely, if the net sediment transport caused by the density-driven flow dominates over that caused by the river flow, the ETM shifts upstream in the deepened channel and downstream in the other seaward channel. Keeping the width of a seaward channel at the junction fixed, the reduction in the landward width convergence causes the ETM in the narrowed channel to shift upstream, while the ETM in the other (seaward) channel to shift downstream. These findings are qualitatively consistent with field observations in the Yangtze Estuary or the Pearl Estuary. Sensitivity results are explained by linking sediment transport to water transport and subsequently analysing the changes in net water transport.

Nederlandse samenvatting

Estuaria zijn vormen de overgangsgebieden tussen rivier en zee, alwaar menging van zoet en zout water plaatsvindt. Veel estuaria bestaan uit meerdere met elkaar verbonden kanalen en vormen zo een zogenaamd estuarien kanalennetwerk. Ze zijn belangrijk voor zowel de ecologie als de economie. Zoet water en fluviatiele sedimenten worden voortdurend in het systeem afgevoerd door de stroming van de rivieren. Daarnaast zorgt de getijdenstroming ervoor dat er periodieke uitwisseling van water en sedimenten is met de open zee. Water en sedimenten worden ook uitgewisseld op de knooppunten van de kanalen. Daarom worden estuariene kanaalnetwerken gekenmerkt door complexe hydrodynamica en sedimentdynamica. Dit leidt o.a. tot het bestaan van estuariene troebelingsmaxima (ETM), waar de concentratie van gesuspendeerd sediment een lokaal maximum bereikt. Het doel van dit proefschrift is om meer inzicht te krijgen in de hydrodynamica en de dynamica van het ETM in estuariene kanaalnetwerken onder natuurlijke omstandigheden, maar ook op hun respons op veranderingen in deze omstandigheden door bijvoorbeeld klimaatverandering of menselijke ingrepen.

Hoofdstuk 2 beschrijft hoe de getijvoortplanting en de verdeling van het rivierwatertransport in estuariene kanaalnetwerken afhangt van de zoetwaterafvoer, externe getijforcering, lokale veranderingen in de geometrie, en zeespiegelstijging. Hiertoe is een semi-analytisch model ontwikkeld, dat de interacterende rivier- en getijdenstroming in het estuariene kanaalnetwerk simuleert. De waterbeweging wordt geforceerd door een dubbeldaags getij (M_2 getij) aan het einde van elk kanaal dat in verbinding staat met de open zee en een constante rivierafvoer op de bovenstroomse randen. Er wordt uitgegaan van behoud van massa en continuïteit van waterhoogte bij alle knooppunten. Het model wordt toegepast op een prototype systeem, namelijk het estuarium van de Yangtze. De resultaten komen goed overeen met veldgegevens en laten zien dat een toename van de rivierafvoer of van de getijdenstroming de wrijving van zowel de rivierafvoer als de getijdenstroming verhoogt door de intensievere rivier-getij

interacties, die worden gekenmerkt door zowel de bodemschuifspanning als de interne schuifspanning. Daarom vermindert een grotere rivierafvoer de getijdenstroming en de fasesnelheid van de getijdengolf. Het rivierwatertransport in elke kanaal is evenredig met de rivierafvoer en de verdeling van het rivierwatertransport over de kanalen wordt dus niet beïnvloed door de rivierafvoer. Er is een positieve correlatie gevonden tussen de gemiddelde amplitude van de getijdenstroming in het hele estuariene kanalennetwerk en het voorgeschreven getijdenverschil. Laatstgenoemde heeft nauwelijks invloed op de verdeling van het rivierwatertransport. Toevoeging van een shortcut-kanaal vermindert het waterstandsverschil tussen de kanalen die ermee verbonden zijn. Het plaatselijk verdiepen en versmallen van een kanaal heeft tegengestelde effecten op zowel de getijvoortplanting als het rivierwatertransport, vanwege hun tegengestelde effecten op de kanaaldoorsnede. In geval van zeespiegelstijging neemt de dwarsdoorsnede in elk kanaal toe, waardoor de rivierstroming afneemt en er dus minder gemiddelde waterstandsverhoging nodig is om de rivierstroming aan te drijven. Aangezien de diepte varieert over de kanalen, is de relatieve verandering in gemiddelde waterdiepte het grootst in de ondiepste kanaal. Daarom wordt meer rivierwatertransport vanuit de diepere kanalen naar de ondiepere kanalen verdeeld.

Netto (d.w.z. getijgemiddeld) watertransport in de kanalen van een estuarien netwerk wordt niet alleen veroorzaakt door rivierstroming, maar ook door bijvoorbeeld de horizontale dichtheidsgradiënten en getijden. Deze laatste kunnen een netto watertransport genereren via gelijkschakeling van het getij, die worden geïnduceerd door niet-lineaire termen in de hydrodynamische vergelijkingen, zoals advectie van momentum, surplus volumetransport ten gevolge van variërende hoogte van het zeeoppervlak (resulterend in Stokes transport), en de asymmetrie in het verticale snelheidsprofiel gedurende een getijcyclus (resulterend in snelheids-diepte asymmetrie). Het netto watertransport, de componenten daarvan alsmede de verdeling van deze transporten over de kanalen worden bestudeerd in hoofdstuk 3 door het in hoofdstuk 2 gebruikte model uit te breiden. De resultaten van de toepassing van het model op het estuarium van de Yangtze komen vrij goed overeen met die uit de literatuur. In een estuarien kanalennetwerk waarbij de maximale stroomsnelheid van de rivier vergelijkbaar met die van het getij, is de verdeling van het netto watertransport licht gevoelig voor de rivierafvoer. Dit komt omdat het netto watertransport gedomineerd wordt door het rivierwatertransport, waarvan de verdeling ongevoelig is voor de rivierafvoer. Het netto watertransport door getijden in elk kanaal schaalt bijna lineair met de voorgeschreven getijdehoogte-amplituden. Voor een goed gemengd estuarien kanalennetwerk is in de bijdrage van horizontale dichtheidsgradiënten aan het netto watertransport verwaarloosbaar. Uit de modelresultaten blijkt verder dat de verdieping van één van de kanalen resulteert in meer zeewaarts netto watertransport als gevolg van rivier en getijden, terwijl er minder zeewaarts wordt getransporteerd als gevolg van de horizontale dichtheidsgradiënt. Vernauwing daarentegen zorgt ervoor dat de

vaargeul minder rivierwatertransport vanuit de bovenstroomse vaargeul ontvangt. Zeespiegelstijging tot 2 m leidt tot een gelijkmatigere verdeling van het rivierwatertransport bij elk knooppunt. De verdeling van het netto watertransport in het estuarium van de Yangtze is weinig gevoelig voor zeespiegelstijging, omdat de verandering van elke component in het netto watertransport wordt gecompenseerd naarmate de zeespiegel stijgt. Deze bevinding geldt met name voor het estuarium van de Yangtze en is ook in andere studies gerapporteerd.

Verscheidene veldwaarnemingen in estuariene kanaalnetwerken hebben het bestaan van ETM in meerdere kanalen tegelijk aan het licht gebracht. Bovendien kunnen ETM's zich in de loop van een seizoen van de ene kanaal naar de andere verplaatsen. Daarnaast kunnen ze verdwijnen na de aanleg van vaarkanalen of stroomopwaarts gelegen dammen, die de fluviatiele sedimenttoevoer verminderen. Om de afhankelijkheid van ETMs in een estuarien netwerk van fluviatiele sedimentafvoer en van veranderingen in diepte en breedteconvergentie in één kanaal van het netwerk beter te begrijpen, wordt het in hoofdstuk 3 gebruikte model verder uitgebreid door de dynamica van gesuspendeerde sedimenten te koppelen aan waterbeweging. In elk kanaal wordt het sediment van de bedding gesuspendeerd door de getijdenstroom en wordt de morfodynamische evenwichtstoestand verondersteld, d.w.z. gedurende één getijdecyclus houden afzetting en erosie van sediment elkaar in evenwicht. Bij elk knooppunt voldoet het sediment in suspensie aan de massabehoud en wordt verondersteld dat de over getij en diepte gemiddelde sedimentconcentratie concentratie continu is. Om meer fundamentele kennis te verkrijgen over de complexe sedimentdynamica in een estuarium, wordt het model toegepast op een geïdealiseerd netwerksysteem met drie kanalen, waarin het horizontale nettotransport van sediment voornamelijk te wijten is aan de rivierstroming en dichtheidsgedreven stroming. De locatie van een ETM bevindt zich dicht bij de plaats waar het netto sedimenttransport gelijk is aan de sedimenttransportcapaciteit. Het blijkt dat verhoging van de fluviatiele sedimentafvoer, bij dezelfde rivierafvoer en dezelfde horizontale dichtheidsgradiënten, zorgt voor een stroomopwaartse verschuiving van de ETM-locaties. In geval van verdieping van een zeewaartse kanaal is de respons afhankelijk van de omstandigheden. Als het netto sedimenttransport veroorzaakt door de rivierstroming domineert boven dat veroorzaakt door de dichtheidsgedreven stroming, verschuift de ETM stroomafwaarts in het verdiepte kanaal en stroomopwaarts in het andere zeewaartse kanaal. Omgekeerd, als het netto sedimenttransport veroorzaakt door de dichtheidsgedreven stroming domineert boven dat veroorzaakt door de rivierstroming, verschuift de ETM stroomopwaarts in het verdiepte kanaal en stroomafwaarts in het andere zeewaartse kanaal. Vernauwing van een zeewaarts kanaal leidt er toe dat de ETM in het verdiepte kanaal stroomopwaarts verschuift, terwijl de ETM in het andere (zeewaartse) kanaal stroomafwaarts verschuift. Deze bevindingen zijn kwalitatief in overeenstemming met veldwaarnemingen in zowel het Yangtze estuarium als het Pearl estuarium. De gevoeligheidsresultaten worden verklaard door het sedimenttransport te koppelen aan het watertransport en

vervolgens de veranderingen in het netto watertransport te analyseren.

Acknowledgements

As the embodiment of my four-year journey in the world of academia, this thesis would not have been possible without the help and support of many people. I thank all of you whose life path intersects with mine.

I would like to thank my supervisor Huib de Swart. Thank you for taking care of the progress and benefit of my PhD, passing your knowledge, experience, and insights to me, forgiving numerous errors I made, tolerating my randomness, and the conversation about classical music. Over the course of my life, I may have forgotten most of the theories about tides, but I will remember how precious our moon is and tides are the manifestation of the Earth's rotation, taught by the most precise person I know (probably your head is shaking while reading). More importantly, thank you for showing me the way of science that leads me to the awareness of the following, as written by Heisenberg: "What we observe is not nature itself, but nature exposed to our method of questioning."

A special thank-you goes to Yoeri Dijkstra. You were the mediator between Huib and me, both of whom can be stubborn sometimes. Thank you for initiating the collaboration and very patiently witnessing every single step I made. My happiest working days were the days we coded together at TUD. Thank you for teaching me the principle of sufficient reason, "Everything must have an explanation", which is reflected in every piece of your thoughts. You have the superpower of unifying different theories, as well as the unorganised fragmented information coming out of me.

I would like to thank three members of SKLEC at East China Normal University. You are the best Chinese researchers and scientists. Heqin Cheng and Chenjuan Jiang, thank you for your assistance in my research with your expertise in the Yangtze Estuary. Zhanhai Li, thank you for the discussion on sediments over the timescale of three years.

I would like to thank all members of the coastal group. Tjebbe, you are definitely the person who has taught me the most hard-knowledge and skills in this country–physics, maths, Python, Julia, VS Code, Dutch, ice-skating, sail-

ing Gudsekop, theories about coffee and its machine, and NS train technologies to name a few. You are the best non-Chinese ping-pong player. I should have stored the largest gember in formaldehyde. Janneke, I am grateful for our conversation about marriage and life. After summer school at Granada, one of my favourite musical pieces "Recuerdos de la Alhambra" has new meanings. I am hoping to climb some rocks! Abdel, thank you for the food and tea containing the proper amount of sugar, the fish dish in Texas, and the interesting stories coming from different continents, some of which I would share with my wife and other friends immediately. Bouke, I greatly enjoyed our scientific discussion and your laughter.

I would also like to thank a few other people at IMAU. Thank you, Eric, Daniele, André, David, Getachew, Juhi, Arthur, Peter, Philippe, Maurice, and Mikael, for making my stay at IMAU joyful. Kris, thank you for all talks and for helping with my Dutch.

I would like to thank my Chinese friends. Shuyang, thank you for helping with finding the lost phone, after which I met my wife and many other great Chinese friends. Concretely, thank you for mediating my family conflicts. Your stay at our home taught me things about life that I wish I could have known earlier. Jieqiong, thank you for showing us how physically fast an emotionally not-so-fast person can be through mopping and cooking. Puqiao, thank you for your professional medical knowledge. I feel our lives are secured from, e.g., accidentally eating food that we hesitate to eat. Zhongyang, although you work at IMAU, I want to thank you here because the day we met was the last day of my contract. Thank you for understanding and sharing your experience with Voldemort. Xiao, thank you for all our scientific conversations. We have the same but different backgrounds. You are the only friend with whom I can discuss tides, salt, and sediment, in Chinese. Mingyang, thank you for adding new elements to my life. Our interests are almost always aligned, and you are the expert in any domain of your interests. Weichao, thank you for trusting us and sharing your life experience with us.

I would like to thank a special friend of mine, abul Nader Al-Ziadat. Thank you for all the encouragement that partially stimulated me to start a PhD. The frequency you have appeared in my mind is much higher than that of our calls. I am hoping to meet you in person again in the near future.

I would like to thank my family members. Thank you, my wife, Jiaxin Li, for showing me the meaning of life is life itself, not to mention your companionship, support, and love. What I learnt from us is that everything, including myself, changes with the flow of time, as a grain of salt dissolved in water, be part of water, and flows with water. Thank you, mum and dad, for your unconditional love. Thank you, Ziyu, for introducing me to the world of artificial intelligence.

Curriculum vitæ

Jinyang Wang was born on May 27, 1993 in Shanghai, China. For his secondary education, he attended Shanghai Datong Junior High School between 2004 and 2008 and Shanghai Datong High School between 2008 and 2011. In July 2016, he received a Bachelor of Science degree in Applied Mathematics from the Xi'an Jiaotong-Liverpool University, China, with a double degree from the University of Liverpool, the UK. He wrote his bachelor thesis on "Phase-locking in the Arnold's family" under the supervision of Dr. Simon Lloyd. In October 2017, he received a Master of Science degree in Advanced Mathematics from the University of Exeter, the UK. The master thesis was on "Non-linear dynamics and symmetry of three weakly coupled oscillators systems", supervised by Prof. Peter Ashwin. In March 2018, he started to work as a Ph.D. candidate at the Institute for Marine and Atmospheric research Utrecht (IMAU), Utrecht University, The Netherlands, under the supervision of Prof. dr. Huib de Swart. Dr. Yoeri Dijkstra initiated the collaboration with Jinyang Wang in April 2019 at the Ems-Scheldt workshop and became the co-supervisor of Jinyang Wang from May 2020.

Since October 2022, Jinyang Wang works as a Treasury Modeller at Rabobank in Utrecht, The Netherlands.